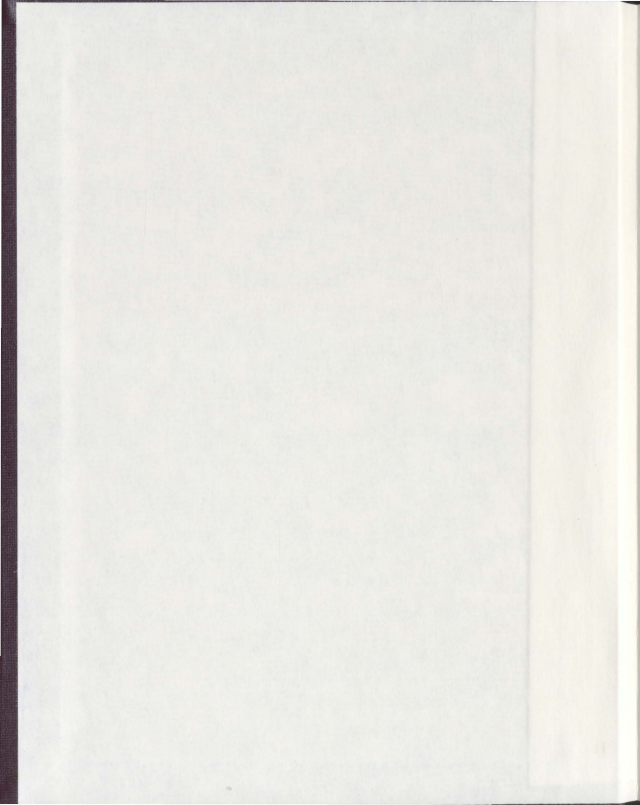


CONTROLS ON VARIABILITY OF MUDSTONE MINERALOGY

MATTHEW JOHNSTON



Controls on Variability of Mudstone Mineralogy

By

© Matthew Johnston, B.Sc. (Hons)

*A Thesis submitted to the School of Graduate Studies
in partial fulfillment of the requirements for the degree of
Master of Science*

*Department of Earth Sciences
Memorial University of Newfoundland*

September 2012

St. John's

Newfoundland

ABSTRACT

The primary aim of this work is to investigate heterogeneity in the mineralogical composition of mudstones resulting from input (detrital, production and diagenetic) variability. With this aim four formations were examined with three unique investigations.

Heterogeneity as a result of diagenesis in the Exshaw Formation (Devonian-Carboniferous) was investigated with a focus on the sulfur cycles influence on mudstone composition. Heterogeneity related to the carbon cycles influence on source and reservoir characteristics of mudstones was analyzed by comparing two carbonate-rich mudstone units (i) the Utica Shale (Ordovician) and (ii) the Winterhouse Formation (Ordovician). The Benbulbin Shale (Devonian-Carboniferous) was utilized as a natural laboratory to investigate the scale of heterogeneity in mudstones.

Accurately evaluating fine-grained rocks requires investigating rock properties on a sub-centimetre scale; therefore in all formations lithofacies variability was measured with both petrographic (transmitted light, SEM) and geochemical methods (XRD, XRF, TOC and $\delta^{13}\text{C}$) in addition to field logging.

ACKNOWLEDGMENTS

First and Foremost I would sincerely like to thank my supervisor Dr. Joe Macquaker. Thank you for being constantly encouraging, supportive and allowing me to pursue the aspects of geology and science that interest me. I've learned a great deal from you over the past few years that will continue to be invaluable as I move on through both my career and life.

I also extend my gratitude to my co-supervisor Dr. Graham Layne. My project significantly benefited from your insight and guidance.

When I began my Masters almost all of the techniques were new to me and I would not have been able to complete the work without the help of a number of people. Thank you to Dario Harazim for helping me with petrography and for having discussions about mudstones that kept me both focused and up to date. Thank you also to those in (or formally in) the CREAT network for their support with analytical procedures, especially Glenn Piercey, Michael Schaffer, Dr. David Grant, Dr. James Conliffe, Dr. Wanda Alyward, Pam King and Helen Gillespie.

I gratefully acknowledge the financial support I received from the Ireland Canada University Fund (ICUF), and the Government of Newfoundland and Labrador's Petroleum Exploration Enhancement Program (PEEP).

Thank you to all the grad students of the Earth Science department at MUN, you made coming into the office/lab/field everyday a great experience. Whether going hiking in Gros Morne, the East Coast Trail or George Street this past couple of years has been a lot of fun.

A special thank you to Scott and my parents, without your support I would never have even been able to start a Masters. Thank you for giving me so many opportunities in life and always being so supportive. Finally, I would like to thank my best friend Natalie. You have been a continuous source of support in every possible way and I could never express how much it is appreciated. Right from the day we drove to St. John's together it's been a constant adventure, I will never forget all that we have experienced together.

TABLE OF CONTENTS

ABSTRACT	II
ACKNOWLEDGMENTS.....	III
TABLE OF CONTENTS	V
LIST OF FIGURES.....	VIII
LIST OF TABLES.....	XIV
LIST OF ABBREVIATIONS AND SYMBOLS.....	XV
1. : INTRODUCTION & OVERVIEW	16
1.1. Introduction.....	16
1.2. Background.....	18
1.2.1. Mudstones and biological evolution	18
1.2.2. Evolution of terrestrial land plants: Impact of chemical weathering in soils on mudstone composition	20
1.2.3. Redox and geochemical conditions during deposition	24
1.3. Objectives	27
1.4. Figures.....	29
CO-AUTHORSHIP STATEMENT.....	30
2. : HIGH-RESOLUTION FACIES ANALYSIS AND MARCASITE FORMATION IN THE TYPE SECTION OF THE FINE-GRAINED EXSHAW FORMATION	32
2.1. Introduction.....	32
2.2. Background on Iron-Disulfides.....	33
2.3. Formation Pathway 1: Oxidation of Primary Pyrite and Reprecipitation of Marcasite.....	35
2.3.1. Sulfate reduction and associated sulfur isotope fractionations	35
2.3.2. Pyrite formation and associated sulfur isotope fractionations	36
2.3.3. Pyrite Oxidation.....	36
2.3.4. Precipitation of Marcasite.....	37
2.3.5. Summary of $\delta^{34}\text{S}$ fractionations in Formation Pathway 1	38
2.4. Formation Pathway 2: Lead-Zinc type deposit.....	38
2.4.1. Lead-Zinc Type deposit with sulfides from the bacterial sulfate reduction of organic matter.....	39
2.4.2. Lead Zinc Type deposit with sulfur derived from bacterial reduction of evaporites or anhydrites.....	39
2.4.3. Lead Zinc Type deposit with sulfur derived from thermochemical reduction of evaporites or anhydrites.....	40
2.5. Materials and Methodology	41
2.6. Geological History	43
2.7. Results.....	44
2.7.1. Clay-bearing sulfide-bearing arkose sandstone	44
2.7.2. Thin bedded dolomite cement-rich mudstone.....	46

2.7.3.	Thin-bedded silt and pyrite-bearing clay-rich mudstone	46
2.7.4.	Thin-bedded normally graded silt-bearing silica-rich mudstone	47
2.7.5.	Calcite cement-dominated mudstone	48
2.8.	Discussion	49
2.8.1.	Lithofacies interpretation	49
2.8.2.	Metal Disulfide Analysis	51
2.9.	Conclusions	55
2.10.	Tables	58
2.11.	Figures	60
3.	: HIGH-RESOLUTION ANALYSIS TO DETERMINE CONTROLS ON CARBON SEQUESTRATION AND MINERALIZATION IN ORDOVICIAN SHALE GAS TARGETS	70
3.1.	Introduction	70
3.2.	Aims and objectives	73
3.3.	Geological setting	74
3.4.	Materials and methodology	76
3.5.	Results	77
3.5.1.	Utica Formation	78
3.5.2.	Winterhouse Formation	84
3.6.	Discussion	87
3.6.1.	Sediment origins, dispersal and bioturbation	87
3.6.2.	Diagenesis	91
3.6.3.	Carbon cycling in Ordovician mudstones (sequestration vs. mineralization)	94
3.7.	Conclusions	98
3.8.	Tables	100
3.9.	Figures	103
4.	: MICROLITHOFACIES ANALYSIS TO INVESTIGATE THE SCALE OF VARIABILITY IN FINE-GRAINED MUDSTONES: USING THE BENBULBEN SHALE OF SLIGO CO. IRELAND	119
4.1.	Introduction	119
4.2.	materials and methodology	121
4.3.	Geological History	123
4.4.	Results	124
4.4.1.	Burrow mottled silt-bearing, clay-rich calcareous mudstone with broken skeletal debris	125
4.4.2.	Homogenized, burrow mottled silt-bearing carbonate-rich calcareous mudstone	126
4.4.3.	Homogenized pseudo-sparry calcite- and silt-rich calcareous mudstone	128
4.4.4.	Homogenized silt-bearing clay-rich calcareous mudstone with broken skeletal debris	129
4.4.5.	Homogenous silt-bearing clay-rich calcareous mudstone	130
4.4.6.	Thin-bedded normally graded fossil-bearing, silt-rich calcareous mudstone	131
4.4.7.	Overall stacking patterns	132

4.5. Discussion	132
4.5.1. Fine-grained sediment production, delivery and accumulation	132
4.5.2. Bioturbation	134
4.5.3. Diagenetic attributes	135
4.5.4. Interpretation of stacking patterns and implications for petrophysical properties.....	136
4.5.5. Scale of compositional variability	137
4.6. conclusions.....	139
4.7. Tables.....	140
4.8. Figures.....	141
5. : CONCLUSIONS.....	151
BIBLIOGRAPHY	156

LIST OF FIGURES

- Figure 1.1: Flow chart demonstrating the significant and interconnected chemical (right) and physical (left) impacts a lack of vegetation on the Earth's surface may have created for the deposition of fine grained rocks.....29
- Figure 2.1: Map demonstrating the extent of the Exshaw and associated Bakken Formations. Inset is a map of the regional geology around the Field location, which is in Jura Creek near the town of Exshaw in the Rocky Mountains of Alberta, Canada. Modified from Asgar-Deen and Adams (2010), Price (1970), and Smith and Bustin (2000).....60
- Figure 2.2: Stratigraphic log of the measured section of the Exshaw Formation at its type section in Jura Creek, Alberta.....61
- Figure 2.3: Petrographic observations of clay-bearing sulfide-rich arkose sandstone. (A) Scan of thin section showing large grain sizes and sulfide minerals. (B and C) Optical images from petrographic microscope. Erosive surface is arrowed in C. (D to F) Backscatter electron optical micrographs. Note wide range of diagenetic minerals in (E) and (D). A large amount of marcasite intergrown with pyrite and sphalerite can be seen in (F) Mineralogy is arrowed and labeled as; Q – quartz, Ca – calcite, Ap – apatite, R-rutile, Pl – plagioclase, Py – Pyrite, M – marcasite and Sp – sphalerite.....62
- Figure 2.4: Petrographic observations of thin-bedded dolomite cement-rich mudstone. (A) Scan of thin section showing the large extent of pyrite within this facies. (B) Optical image from petrographic microscope, note the thin normally grading beds. (D to F) Backscatter electron optical micrographs. Pyrite is very extensive in a euhedral form, often forming the base of thin beds. Mineralogy is arrowed and labeled as; Py – Pyrite, D – Dolomite.....63
- Figure 2.5: Petrographic observations of thin-bedded silt and pyrite-bearing clay-rich mudstone. (A) Scan of thin section showing very clay rich fabric. (B) Optical image from petrographic microscope demonstrating the thin-bedded nature of the facies. (C to D) Backscatter electron optical micrographs. Pyrite occurs throughout this facies in a euhedral form. Mineralogy is arrowed and labeled as; Q – quartz, Ca – calcite, Ap – apatite, D – dolomite, Ru-rutile, and Py – Pyrite.....64
- Figure 2.6: Petrographic observations of thin-bedded normally graded silt-bearing silica-rich mudstone (A) Scan of thin section showing very clay rich fabric. A solid line highlights the normally grading nature of the facies with an arrow pointing at the silt-rich base of a bed. (B-D) Optical images from petrographic microscope. (C and D) show agglutinated benthic foraminifera, which are common in the facies (E and F) Backscatter electron optical micrographs. An agglutinated benthic foraminifera can be seen in (E) with K-feldspar making up the test and a cavity, which is either

empty or filled with organic matter. Mineralogy is arrowed and labeled as; Q – quartz and K-feldspar.....	65
Figure 2.7: Petrographic observations of calcite-cement dominated mudstone (A) Scan of a thin section showing homogenous fabric. (B and C) Optical images demonstrating the clotted fabric and in (C) a large quartz-rich nodule. (C to D) Backscatter electron optical micrographs. Calcite makes up most of the facies with some quartz cement throughout and some very large quartz nodules. In (E) a quartz grain can be seen with a rim of albite surrounding it. Mineralogy is arrowed and labeled as; Q – quartz, Ca – calcite, Al-albite, and Py – Pyrite.	66
Figure 2.8: Results of SIMS analysis with $\delta^{34}\text{S}$ plotted against the height above the base of the measured section of the Exshaw Formation. Note: although pyrite was detected at other intervals of the stratigraphic log, individual grain sizes were too small to accurately measure $\delta^{34}\text{S}$ with the SIMS.	67
Figure 2.9: Petrographic observations of the clay-bearing sulfide-rich arkose sandstone showing ^{34}S measurements of marcasite and pyrite. (A) Optical images from petrographic microscope in reflected light. (B to D) Backscatter electron optical micrographs of the circular mounts, which were analyzed for ^{34}S . In (B) the boundary between a cluster of degraded framboidal pyrite and bladed marcasite is circled with a dash line. The marcasite can be seen growing around the pyrite suggesting a later precipitation of the marcasite. Mineralogy is arrowed and labeled as; Q – quartz, Ca – calcite, Ap – apatite, D - Dolomite Py – Pyrite, M – marcasite, Mil – Millerite and Sp – sphalerite.	68
Figure 2.10: Graph comparing the amount of elemental metals in the basal arkosic unit to all other facies in the Exshaw Formation.	69
Figure 3.1: Map of the field locations of the Utica Shale and surrounding regional geology in the St. Lawrence Lowlands of Quebec. (Modified from (Belt et al., 1979).	103
Figure 3.2: Stratigraphic log of the two measured sections of the Utica Shale	104
Figure 3.3: Petrographic observations of the normally graded, very thin bedded, pelleted, silt-bearing, clay-rich carbonate mudstone (U1). (A) Scan of thin section showing thin bedding planes and fining upward sequences. Solid triangles demonstrate a fining upward sequence. (B) Optical image from petrographic microscope. Circle with dashed lines are compacted pellets. (C and D) Backscatter electron optical micrographs. Mineralogy is arrowed and labeled as; Q – quartz, Ca – calcite, D – dolomite, Pl – plagioclase, Py – Pyrite, and B – Barite.....	105
Figure 3.4: Petrographic observations of thin-bedded partly homogenized, silt- clay- and carbonate cement-bearing mudstone (U2). (A) Scan of thin section showing internally homogenized beds. (B) Optical image from	

- petrographic microscope. Circled with dashed lines are compacted pellets. (C and D) Backscatter electron optical micrographs. Mineralogy is arrowed and labeled as; Q – quartz, Ca – calcite, D – dolomite, Al – albite, Py – Pyrite, and Ap – Apatite. 106
- Figure 3.5: Petrographic observations of normally graded, ripple laminated, very fine sand, coarse silt and fecal-pellet bearing carbonate mudstone (U3). (A) Scan of thin section showing normally grading beds, one of which is highlighted with a solid bar. (B) Optical image from petrographic microscope. Down-lapping surfaces are identified with dashed lines. Circled with dashed lines are crushed pellets in the fabric of this facies. Circled with solid lines are nodules, which have been filled with either quartz or pyrite. (C to F) Backscatter electron optical micrographs. Mineralogy is arrowed and labeled as; Q – quartz, Ca – calcite, and Py – pyrite. 107
- Figure 3.6: Petrographic observations of thin-bedded, normally graded, silt- and very fine sand-bearing calcite-cement-rich mudstone (U4). (A and B) Scans of thin sections showing event beds with sharp and uneven erosional surfaces. (C and D) Optical images from petrographic microscope. Highlighted in (B) and (C) are the two sections of individual beds (i) more coarse silt to sand base (ii) more silt rich top. (E and F) Backscatter electron optical micrographs. Mineralogy is arrowed and labeled as; Ca – calcite, D – Dolomite and Py – pyrite. 108
- Figure 3.7: Petrographic observations of normally graded, burrow mottled silt- and clay-bearing calcite cement-rich mudstone (U5). (A) Scan of thin section showing the very homogeneous fabric of the facies. (B) Optical image from petrographic microscope. (C) Backscatter electron optical micrograph. In (C) can calcite cement is extensive throughout the fabric, and can see a round approximately 30 μm grain of apatite near the centre of the image. 109
- Figure 3.8: Petrographic observations of thin, relict bedded, partially homogenized coarse silt-bearing, clay-rich calcareous mudstone (U6). (A) Scan of thin section showing disrupted bedding planes. (B) Optical image from petrographic microscope. (C to F) Backscatter electron optical micrographs. Circled with dashed lines are dolomite grains with visible porosity around them. Mineralogy is arrowed and labeled as; Q – quartz, Ca – calcite, D – dolomite, Pl – plagioclase, and Py – Pyrite. 110
- Figure 3.9: Petrographic observations of thin-bedded and burrow mottled fine silt-bearing, calcite cement-rich mudstone (U7). (A) Scan of thin section showing disrupted bedding planes. (B) Optical image from petrographic microscope showing bioturbation. (C to F) Backscatter electron optical micrographs demonstrating feldspar dissolution. Mineralogy is arrowed

and labeled as; Q – quartz, Ca – calcite, D – dolomite, Pl – plagioclase, An – anorthite and Py – Pyrite..... 111

Figure 3.10: Map of the field location and regional geology surrounding the Winterhouse Formation, which is part of the Long Point Group, on the Port Au Port Peninsula of Newfoundland. (Modified from (Williams, 2000). 112

Figure 3.11: Stratigraphic log of the measured section of the Winterhouse Formation. . 113

Figure 3.12: Petrographic observations of homogenized, calcite-cemented fine-grained calcareous sandstone (W1). (A) Scan of thin section showing thin bedding planes and fining upward sequences. Solid lines demonstrate the preserved laminations. (B) Optical image from petrographic microscope. (C and D) Backscatter electron optical micrographs. Circled with dashed lines are concavo-convex quartz grain contacts, which indicate that grain dissolution porosity, occurred post-compaction. Mineralogy is arrowed and labeled as; Q – quartz, Ca – calcite, F- K-Feldspar, and Py – Pyrite..... 114

Figure 3.13: Petrographic observations of homogenized sand- and silt-bearing calcite cement-rich mudstone (W2) Scan of thin section demonstrating homogenized and bioturbated nature of individual beds. Planolites isp. burrows are arrowed. (B and C) Optical images from petrographic microscope. (B) has a bored surface indicating that this facies solidified before the next was colonized and subsequently cement. (D – E) Backscatter electron optical micrographs. Mineralogy is arrowed and labeled as; Q – quartz and Ca – calcite, K – k-feldspar, Ap – apatite, R – rutile and Py – pyrite..... 115

Figure 3.14: Petrographic observations of thin relict bedded, partially homogenized clay- and dolomite cement-bearing, silt-rich siliclastic mudstone (W3). (A) Scan of thin section with arrows pointing to the burrows interpreted to be of *Rhizocoarallium*. (B and C) Optical images from petrographic microscope. (D to F) Backscatter electron optical micrographs. Can see there is an abundance of detrital grains, which have been cemented together by calcite and quartz. Mineralogy is arrowed and labeled as; Q – quartz, Ca – calcite, D – dolomite, B – barite, K – K-Feldspar, Ch – chlorite and Py – pyrite. 116

Figure 3.15: Petrographic observations of burrow mottled fine-sand bearing silt-rich mudstone (W4) (A and B) Optical images from petrographic microscope. Water escape structures and that bioturbation have left little of primary depositional structures. (D to F) Backscatter electron optical micrographs. (D) shows the boundary between the inside and outside of a burrow, with the burrow containing much more fine-grained material. The partial dissolution of a K-feldspar grain to quartz can be seen in (E). Calcite cement filling in the boundaries between individual pores can be seen in (F). Mineralogy is arrowed and labeled as; Q – quartz, Ca – calcite, K – K-Feldspar, and Py – pyrite. 117

Figure 3.16: Figure demonstrating the link between sediment delivery rates, extent of cement and organic carbon preserved in carbonate-rich mudstone units. These parameters exert key controls on the source vs. reservoir potential of unconventional hydrocarbon reservoirs. (Information for figure (Bohacs, 2005; Butler and Dam, 1994; Sageman et al., 2003)).	118
Figure 4.1: i) Map of Ireland demonstrating location of field site at Streedagh Point in Sligo Co. Ireland. ii) Geologic map demonstrating regional geology of Northwest Ireland and significant syncline structures in the region, BF – Belhaven Fault, CF – Curlew Fault, CVF – Clogher Valley Fault, GF = Grange Fault, OMPF = Ox Mountains – Pettigoe Fault (Modified from Aretz et al., 2010, after Dixon, 1972).	141
Figure 4.2: Stratigraphic log of measured section of the Benbulbin Shale at Streedagh Point, in Sligo County, Ireland.	142
Figure 4.3: Petrographic observations of the burrow mottled silt-bearing, clay-rich calcareous mudstone with broken skeletal debris. (A) Scan of thin section demonstrating significant preservation of trace fossils. (B-D) Optical images from petrographic microscope demonstrating the variety of trace fossils; <i>N</i> – <i>Nereites</i> sp., <i>Phy</i> – <i>Phycosiphon</i> sp., <i>Plan</i> – <i>Planolites</i> sp.. Circled in B is an Echinoderm fragment (E-F) Backscatter electron optical micrographs. Dashed line in E represents the boundary of a burrow. Mineralogy is arrowed and labeled as; Q – quartz, Ca – calcite, D – dolomite, Al – albite, and Py – Pyrite.	143
Figure 4.4: Petrographic observations of the homogenized, burrow mottled silt-bearing carbonate-rich calcareous mudstone. (A) Scan of thin section. (B-C) Optical images from petrographic microscope; <i>Plan</i> – <i>Planolites</i> sp.. Diagenetic quartz is visible in C. (D-F) Backscatter electron optical micrographs. Multiple (production and diagenetic) forms of calcite are visible in D-F. Pyrite (D) and Albite (E-F) can be seen occurring as a pseudomorphic replacement of dolomite. Mineralogy is arrowed and labeled as; Q – quartz, Ca – calcite, D – dolomite, Al – albite, and Py – Pyrite.	144
Figure 4.5: Petrographic observations of the homogenized, pseudo-sparry calcite- and silt-rich calcareous mudstone. (A) Scan of thin section. (B-C) Optical images from petrographic microscope with visible pseudo-sparry calcite. (D-F) Backscatter electron optical micrographs. Pyrite (D) and Albite (E-F) can be seen possibly occurring as a pseudomorphic replacement of dolomite. Mineralogy is arrowed and labeled as; Q – quartz, Ca – calcite, Al – albite, and Py – Pyrite.	145
Figure 4.6: Petrographic observations of the homogenized, silt-bearing clay-rich calcareous mudstone with broken skeletal debris. (A) Scan of thin section. (B-C) Optical images from petrographic microscope (D-F) Backscatter electron optical micrographs. Visible fossils are abundant in this facies	

including brachiopods (A-B) and echinoderms (B, D-E). Mineralogy is arrowed and labeled as; Q – quartz, Ca – calcite, Al – albite, Cl – chlorite and Py – Pyrite.	146
Figure 4.7: Petrographic observations of the homogenous silt-bearing clay-rich calcareous mudstone. (A) Scan of thin section demonstrating soft sediment deformation, which is cross cut by an escape trace. (B) Optical image from petrographic microscope. (C-D) Backscatter electron optical micrographs. B shows escape trace and D demonstrates the composition of the escape trace, with a greater amount of fine grained and organic rich material. Mineralogy is arrowed and labeled as; Q – quartz, Ca – calcite, Al – albite, Cl – chlorite Fe-D – ferroan dolomite and Py – Pyrite.	147
Figure 4.8: Petrographic observations of the thin-bedded normally-graded fossil-bearing, silt-rich calcareous mudstone. (A) Scan of thin section demonstrating an uneven erosional surface at the base of a bed. (B-D) Optical images from petrographic microscope. C demonstrates the upward fining nature of the beds (E-F) Backscatter electron optical micrographs. The dissolution of a dolomite can be observed in E. Mineralogy is arrowed and labeled as; Ca – calcite, Al – albite, and Py – Pyrite.....	148
Figure 4.9: Results from ITRAX X-ray Fluorescence (XRF) data at 2 mm vertical intervals across a selection of the samples collected.	149
Figure 4.10: Comparison between conventional XRF and high resolution ITRAX XRF scan techniques.....	150

LIST OF TABLES

Table 2.1: Fractionation ranges of $\delta^{34}\text{S}$ during each step in the formation of marcasite through the formation and oxidation of pyrite, followed by precipitation of marcasite. Note adenosine 5 ϕ phosphosulfate = APS.....	58
Table 2.2: Fractionation ranges of $\delta^{34}\text{S}$ during each step in the formation of marcasite through a basinal brine meeting sulfur from a bacterial sulfate reduction of organic matter source.....	58
Table 2.3: Fractionation ranges of $\delta^{34}\text{S}$ during each step in the formation of marcasite through the reduction of sulfate from an evaporitic or gypsum source using either bacterial sulfate reduction (scenario 1) or thermochemical reduction (scenario 2) for the reduction of sulfate.....	58
Table 2.4: Analytical results of Exshaw Formation.....	59
Table 3.1: Analytical results of Utica site UC.....	100
Table 3.2: Analytical results of Utica site UCB.....	101
Table 3.3: Analytical results of Winterhouse Formation.....	102
Table 4.1: Analytical results of Benbulbin Shale.....	140

LIST OF ABBREVIATIONS AND SYMBOLS

APS	- Adenosine 5'-phosphosulfate
aq	- Aqueous
BSE	- Backscatter Electron
EDS	- Energy dispersive X-ray
ITRAX	- ITRAX Core scanner
Eh	- Reduction potential measurement (also Redox potential)
IRMS	- Isotope Ratio Mass Spectrometer
kJ	- Kilojoule
kV	- Kilovolts
LIP	- Large igneous province
M	- Meter
mm	- millimeter
Ma	- Megaannum, unit of time equal to 1million years
MaxFS	- Maximum flooding surface
mol	- Mole, unit of measurement used to express amounts of a chemical substance
mM	- Millimolar
mg	- Milligram
Pb-Zn	- Lead-Zinc
R	- High molecular weight reactive organic compounds (e.g. alkanes or alkenes)
SEM	- Scanning electron microscope
SIMS	- Secondary Ion Mass Spectrometry
SRB	- Sulfate reducing bacteria
ton/in ²	- Tonnes per square inch
TOC	- Total organic carbon
UC	- Utica
WH	- Winterhouse
XRD	- X-ray Diffraction
XRF	- X-ray fluorescence
$\delta^{13}\text{C}$	- Measure of the ratio of stable carbon isotopes ^{13}C : ^{12}C
$\delta^{18}\text{O}$	- Measure of the ratio of stable carbon isotopes ^{18}O : ^{16}O
$\delta^{34}\text{S}$	- Measure of the ratio of stable carbon isotopes ^{34}S : ^{32}S
$\Delta G^{0'}$	- Change in Gibbs free energy
μA	- Microampere
μm	- micrometer
$^{\circ}\text{C}$	- Degree Celsius
%	- Percent
‰	- Per mille (parts per thousand)

I. : INTRODUCTION & OVERVIEW

1.1. INTRODUCTION

Fine-grained rocks such as shales and mudstones are the most common sedimentary rock types on Earth. These rocks are significant because they are hydrocarbon source, seals and reservoirs, host metal deposits and are the bounding lithologies in natural aquifers. Despite their significance, extensive scientific analysis of fine-grained rocks has been lacking in sedimentological studies until recently. In the past approximately 5 years researchers have begun to turn their attention to these previously poorly understood fine-grained rocks. The increased analysis has focused primarily on defining very small-scale sedimentological features (Macquaker and Bohacs, 2007). The very fine-grained fabric of these rocks means that any heterogeneity, which is obvious in coarser grained rocks, is much more difficult to identify and requires multiple techniques of high-resolution analysis including petrographic imaging, geochemical and a mineralogical analysis.

Through these analyses it is possible to identify the three components, which comprise fine-grained rocks. These components are derived from (i) detrital inputs to the basin, (ii) production within the basin and (iii) diagenetic alteration of these materials. These fine-grained elements are composed of mineral mixtures of feldspars, phyllosilicates and clays that are derived from weathering and erosion processes on land; the body parts of the fauna and flora living in the oceans and in the near-surface sediments; and from diagenetic processes occurring both close to the sediment water interface and at deeper burial depths. Within any sedimentary succession the relative proportions of these three components vary and thus lithofacies variability is observed.

The aim of this research is to investigate this variability in four different mudstones successions. Between each of the four successions a wide amount of heterogeneity is likely to occur; and further, within each of the successions a significant amount of heterogeneity is anticipated.

The recent paradigm shift in the study of fine-grained rocks has highlighted the remarkable amount of heterogeneity within mudstones (Macquaker and Bohacs, 2007; Schieber et al., 2007). Thus it is important to examine the sedimentological and geochemical characteristics of mudstones at a higher resolution (compared to hand specimen scale) than was previously believed necessary, in order to determine the spatial and temporal locations of the best reservoirs. In particular, it is necessary to determine the sedimentological controls on mineral distributions at the sub-centimetre scale, so that geological models that are constrained by estimates of different sediment production mechanisms, as well as sediment dispersal and subsequent changes during burial, can be tied to estimates of which intervals are most likely to fracture and contain the most organic matter. Therefore, it is important to have a focus on how natural systems and parameters such as; chemical weathering (e.g. the evolution of terrestrial plants and soils) the silica cycle (which can influence the mudstones potential to hydrofracture), organic content (which influences the mudstones potential as a source rock) and marine plankton groups (which control the productivity component), have evolved over Earth's history.

The main objective of this study is to collect and characterise mudstones from four different areas and two different geologic time periods. Particular emphasis were placed on comparing early and late Paleozoic successions to determine if secular changes can be observed that are consistent with the input of detrital materials with different

starting compositions, and the effects of inputs from different microfossil groups. This stratigraphic interval was chosen because it is the time period associated with the evolution of land plants and the development of soil profiles on land.

From these objectives interpretations will be made to identify the heterogeneity both within and between these different successions due to:

- Input changes associated with the development of soils in terrestrial weathering profiles
- Production changes associated with the biological evolution of key microfossil groups
- Differences in the diagenetic influences within and between different basins.

The starting hypothesis of this project is that the type of weathering and inputs, which have changed through time, will have an intrinsic effect on the resulting mudstone composition.

1.2. BACKGROUND

1.2.1. Mudstones and biological evolution

Approximately 542 Ma (i.e. the Pre-Cambrian – Cambrian boundary) the Cambrian explosion occurred, resulting in the relatively sudden appearance of a wide variety of organisms (Vermeij, 1989). It was during this time period that both calcareous algae and organic walled organisms (such as foraminifera) began to appear in abundance (Scott et al., 2003). Prior to this the ocean floor was covered by stratified microbial mats with a simple structure (Bottjer, 2005). Within the microbial mats each layer contained microbial communities with specific metabolism reflecting the decreasing redox potential

(Bottjer, 2005). However during the Cambrian explosion biomineralised skeletons evolved, allowing organisms to anchor themselves to the sea floor and in some cases dig burrows (Meysman et al., 2006). This resulted in deposit-feeding organisms and the colonization of deeper substrates (Bottjer et al., 2000). As these new colonies arose, the simple one-dimensional microbial mats were replaced with complex burrow networks (Meysman et al., 2006). The prevalence of bioturbation had a significant impact on the physical and chemical structure of the ocean floor, and consequently on the mudstones that were subsequently deposited. The burrow networks created by these organisms function as an irrigation system drawing down oxygen from the sediment water interface deeper into the anoxic layers, creating oxic micro-environments throughout deeper portions of the sediment (Shull et al., 2009). Furthermore the burrowing organisms influence the sediment texture as they disrupt bedding, redistribute minerals, counteract compaction processes, and sometimes glue aggregates together (Meysman et al., 2006). Thus bioturbation, and the burrow networks created, result in a high degree of spatial heterogeneity and can influence the porosity and permeability of mudstones.

The process of silicification (by eukaryotes such as radiolarians, and diatoms) and subsequent transport down through the water column after death exerts a major control on the solid phase silica flux to the seafloor (Calvert, 1968). Prior to the rise of radiolarians in the Cambrian period silicic acid concentrations in the oceans were at equilibrium with respect to amorphous silica (110 mgL^{-1} at less than 25°C). However, since this time silica levels in the ocean have diminished, and diminished even further with the rise of diatoms during the late Triassic to early Jurassic, until reaching the low present day concentrations at values of less than 5 mgL^{-1} (Tréguer et al., 1995). Silica is

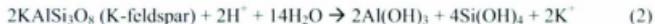
one of the key elemental parameters in the composition of mudstones and therefore the evolution of the silica cycle in the ocean (which has largely been controlled by the evolution of silica bearing organisms) exerts a unique link to the biologically produced component in mudstones.

1.2.2. Evolution of terrestrial land plants: Impact of chemical weathering in soils on mudstone composition

A major turning point in Earth History was the wide spread development of embryophytes (land plants) in the Early Palaeozoic (Devonian period) causing the formation of distinct soil profiles (Algeo et al., 2001; Davies and Gibling, 2010). There are a number of consequences observed to be a result of this event. These include; draw down of atmospheric CO₂ due to enhanced rock weathering and carbon storage, and marine extinctions associated with increased terrestrial nutrient runoff into the oceans (Algeo et al., 2001; Algeo et al., 1998; Davies and Gibling, 2010). Algeo et al. (2001) constructed the “Devonian plant hypothesis” which identifies a link between terrestrial and marine realms as a result of the rise of terrestrial land plants. Testing this hypothesis is inherently difficult due to the spatial heterogeneity of most sedimentological, paleobotanical and geochemical parameters. As a result of this, Algeo et al. (2001) argued that no single dataset is likely to resolve the issue. Rather, exploring the interrelationships between diverse phenomena may yield a better understanding. Algeo et al. (2001) suggested that the rise of terrestrial land plants (and soils) could lead to a shift in clay-mineral composition in marine sediments, from physical-weathering-dominated mineral assemblages of feldspars, illite and chlorite to chemical weathering assemblages dominated by quartz, smectite (or mixed layer illite/smectite) and kaolinite (Weaver, 1967). Smectite and illite are two clay minerals that are highly associated with soil

leaching as a result of the alteration of biotite and plagioclase feldspar precursor minerals (Weaver, 1967).

In the modern Earth, minerals weathered from surface rock exposures are often carried through soils by hydrologic processes. The soils can act as a filtration system as they dissolve the parent rock minerals. Silicates make up the largest portion of rock-forming minerals (approximately 90 % of the Earth's crust). Felsic silicates typically undergo incongruent dissolution, during which easily exchangeable cations such as Ca^{2+} , Mg^{2+} , K^+ and Na^+ , as well as variable amounts of aluminium and silica, are leached, leaving behind a residual clay phase. Two possible reaction pathways are provided in reactions 1 and 2 (Van Cappellen, 2003).



The type of secondary mineral which is formed from this dissolution process is controlled by three factors (Van Cappellen, 2003).

- The composition of the mineral phase (i.e. felsic or mafic).
- The concentration of dissolved ions at the interface between the leached layer and the mineral surface, as well as the bulk amount that are removed from the weathering zone.
- The kinetics of the dissolution reaction as affected by throughflow and temperature.

In some environments the production of acids such as sulfuric and nitric acids can cause severe but localized pH changes (Brady, 1989; Subramanian et al., 2006). These environments arise from the oxidation of reduced sulfur and nitrogen compounds. When

concentrations of these acids are sufficient, they may cause congruent dissolution of the primary mineral phases (as shown in reaction 3). The dissolution of K-feldspar converts a strong acid (sulfuric acid) into a weak acid (silicic) which can be transported through a soil or sediment in an undisassociated form (Welch and Ullman, 1996).



A much more effective pathway for the dissolution of feldspar is in the presence of organic acids. Experimental studies have demonstrated that organic acids can increase rates of dissolution by orders of magnitude relative to inorganic acids with the same acidity (Welch and Ullman, 1996). The citric and oxalic strains of fungi have been described in nature as being very effective at degrading feldspar minerals into secondary minerals (Stillings et al., 1996). During feldspar weathering in the presence of organic acids the secondary minerals formed are often depleted in Al relative to those produced through inorganic acid weathering, due to the fact that organic acids preferentially break Al-O bonds (Blake and Walter, 1999; Stillings et al., 1996).

Mafic minerals make up a smaller portion of the continental crust than felsic minerals. Their weathering involves both dissolution and oxidation-reduction reactions (Van Cappellen, 2003). The minerals olivine, pyroxene, amphibole and biotite are enriched in magnesium and ferrous iron, and as a result they weather rapidly in oxic environments as the Fe^{2+} is initially released through congruent dissolution (eg. reaction 4) and then oxidized and hydrolyzed to ferric hydroxide (reactions 5) (Wogelius and Walther, 1991).



Quartz is the most stable silica solid phase, and quartz dissolution is unaffected by acidity except in extremely acidic conditions (e.g. $\text{pH} < 2$), where high proton concentrations can disrupt silica bonding, or at pH above 8 where the deprotonation of surface Si-O-H bonds can occur (Brady and Walther, 1990). Therefore quartz weathers extremely slowly under normal conditions, allowing the Si atom to be preserved in tetrahedral coordination in solution (Brady and Walther, 1990). However, similar to feldspar weathering, organic acids can play a role in increasing the dissolution of quartz. Blake and Walker (1999) found that quartz dissolution rates were increased by up to a factor of 2.5 when organic acid concentrations of 2-20 mM were present. Organic acids play a significant role in mineral weathering and thus likely influence the pathways which dissolved silica will follow (Drever and Stillings, 1997).

Prior to the evolution of terrestrial land plants in the Devonian period, soils that existed on Earth's surface were vastly different from those present in modern times (Algeo et al., 2001). Modern soils act as filtration systems for continental weathering processes and have a profound influence on fine-grained sediments delivered to the oceans. In soils, the geochemical conditions are quite different compared to the atmosphere and hydrosphere due to the microenvironments created, which can influence the redox and pH within porewaters. This means that minerals that had previously been either metastable or stable at the surface of the Earth dissolve and new minerals, particularly clays, precipitate (de Kamp, 2008). In addition the physical effects of having plants shading and binding the sediment exert an important control on rates and style of runoff (see Figure 1.1).

By exerting a significant control over the detrital influx of not only sediment but also nutrients into the ocean, soils have the potential to influence all three sources of sediments for mudstones (detrital, biogenic and diagenetic). Prior to soils, the detrital portion of the mudstones would have likely contained a much more varied mineralogical composition. This is because minerals previously would not have been subjected to the chemical weathering system that soils can provide (i.e. altering the parent minerals such as olivine and biotite to clay minerals). The decreased concentrations of clay would have the potential to decrease the quantity of organic matter being preserved, as researchers have identified a link between large amounts of highly reactive clay sized particles and the efficient preservation of organic matter (Kennedy et al., 2002). Due to the lack of dissolution of minerals from parent rocks, combined with the lack of leaf litter and nutrients from vegetation and soils systems, a land without soils would provide significantly less nutrient flux to ocean waters. This (combined with less planktonic diversity) should have impacted the primary productivity in the oceans, thus causing a control over the biogenic input of sediments, and further exerting an influence over the redox conditions in the environment of deposition. As a result of the fact that alteration of silicate minerals is not occurring in the same abundance as in a world with soils, dissolved silica is not being created or supplied to the oceans to the same extent as it would after soil development. Therefore a lack of dissolved silica should result in silica cements being far less common in mudstones from the pre-Devonian Earth.

1.2.3. Redox and geochemical conditions during deposition

One of the aims of conducting a geochemical analysis of mudstones is to establish redox conditions during the time of deposition. Aerobic respiration (reaction 6) is the

most energetically favourable metabolic pathway utilized for the oxidation of organic matter. The aerobes which carry out this reaction are equipped with a suite of enzymes capable of degrading complex organic molecules into simpler substrates and CO₂ making this the most efficient way to breakdown organic matter (Froelich et al., 1979; Morse et al., 1987). (The Gibbs free energy “ΔG⁰” has been included with each redox reaction to indicate the amount of energy which is yielded and to demonstrate the decreasing energetic favourability of each subsequent reaction):



The mineral deposition associated with aerobic respiration is non-ferroan calcite (CaCO₃). This process can result in a significant depletion in oxygen concentrations in the sediments and occasionally the bottom waters of the Earth’s oceans (Claypool et al., 1980). When oxygen becomes depleted microbes will begin to utilize nitrate (the next most efficient electron acceptor), for microbial oxidation of organic matter through a process known as denitrification (reaction 7) (Froelich et al., 1979; Morse et al., 1987).



Denitrification is not often associated with mineral deposition because nitrogen is not a common mineral-forming element. In environments where concentrations of nitrate are not high enough to support denitrification (e.g. below the zone of denitrification) the reduction of MnO₂ to dissolved Mn(II) (reaction 8) becomes the most energy efficient process for oxidizing organic matter (Christensen et al., 1987; Froelich et al., 1979; Morse et al., 1987; Piper and Calvert, 2009).

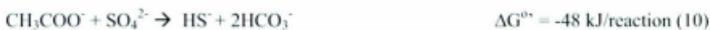


Rhodochrosite (MnCO_3) and Manganous Calcite ($(\text{CaMn})\text{CO}_3$) are minerals which are often associated with reduction of MnO_2 (Lovley and Phillips, 1988). After Mn(IV) reduction the most energetically favourable reaction for the oxidation of organic matter is Fe(III) reduction (reaction 9). The most reactive and readily available form of Fe(III) is ferric hydroxide, the solid phase iron mineral (Lovley and Phillips, 1986).



The deposition of magnetite (Fe_3O_4) and siderite (FeCO_3) have both been associated with Fe(III) reduction (Roh et al., 2003). In general Fe(III) reduction is significantly less important as a terminal electron accepting pathway in comparison to sulfate reduction. In the zone of peak Fe(III) reduction, Fe^{2+} diffuses in every direction throughout the sediment. A portion of this diffuses upwards where it can be oxidized, and form Fe(OH)_3 through an abiological reaction with MnO_2 or NO_3^- (Myers and Nealson, 1988). Fe^{2+} in the pore water may also be removed through a reaction with HS^- which is produced in the underlying sulfate reduction zone. If this occurs a metastable iron monosulfide mineral will form, (e.g. mackinawite (FeS)). This step is a precursor to the formation of pyrite (Rickard and Luther, 2007).

Following Fe(III) reduction the next most energetically favourable metabolic pathway is sulfate reduction (reaction 10).



HS^- can react with Fe^{2+} in the sediment (or water column) to form an insoluble monosulfide (FeS) and eventually pyrite (FeS_2) (Newton and Bottrell, 2007; Rickard and Luther, 2007). Bacterial sulfate reduction is a complex process which proceeds via a variety of individual steps, these involve the breakdown of biopolymeric organic matter

to simple organic molecules by fermentative micro-organisms, sulfate-reducing bacteria (SRB) themselves, and the further oxidation of organic reaction products (Newton and Bottrell, 2007). This process accounts for approximately 50% of the oxidation of organic matter in coastal marine sediments (Jorgensen, 1982).

After sulfate reduction, methanogenesis (reaction 11) is the next (and least) most energetically favourable process for the oxidation of organic matter. Methanogenesis is carried out through the energy metabolism of methanogens, which are microorganisms of the archaea domain (Whiticar, 1999).



Sediment concentrations of magnesium and calcium are key in determining whether ferroan dolomite and ferroan calcite (CaCO_3) are associated with methanogenesis. The step wise process of terminal electron acceptors being positioned in a stratified way is oversimplified in the context of the actual ocean floor (Aller, 1994). Since the evolution (during the Cambrian period) of burrowing organisms redox conditions in sediments occur in complex heterogeneous geometries due to bioturbation drawing down oxygen and altering the redox conditions of the sediment (Aller, 1994; Meysman et al., 2006).

1.3. OBJECTIVES

This thesis is composed of three focused papers, each of which discusses different forms of variability in the composition of mudstones.

The objective of Chapter 2 is to characterise the lithofacies in the Exshaw Formation (Devonian-Carboniferous) using a multi-technique approach and use the Formation as a natural laboratory for examining the sulfur cycle within mudstones. As

indicted above, sulfur is an important biogeochemical element and the state of its preservation in a variety of minerals (e.g. pyrite and marcasite) can yield important information about the geochemical conditions in the water column at the time of deposition and the processes that occurred during diagenesis (Rickard and Luther, 2007; Schieber, 2011).

The carbon cycle is examined in Chapter 3, which compares the Utica Shale and the Winterhouse Formation both of which formed in the Ordovician Period. The objective of this paper is to investigate the connection between cycling of carbon between reduced and oxidized forms, and the heterogeneity that is observed in fine-grained sediments. This balance has important implications for hydrocarbon exploration as the preservation of reduced carbon is necessary to deposit source rocks, and the precipitation of inorganic carbon is key to creating cements making mudstones susceptible to hydrofracturing.

The Benbulbin Shale of North-western Ireland is utilized as a natural laboratory in Chapter 4 with the objective of investigating the scale of heterogeneity in mudstones. The unit is described on a variety of scales linking small-scale textural diversity with geochemical attributes. This allows for an identification of the scale of variability in mineralogical parameters, which are key for identifying important rock forming features such as cements that are necessary for hydrofracturing.

The methods and techniques (e.g. high resolution lithofacies analysis) were consistent in analysis of all four formations to allow for comparison and consistency on the data set.

1.4. FIGURES

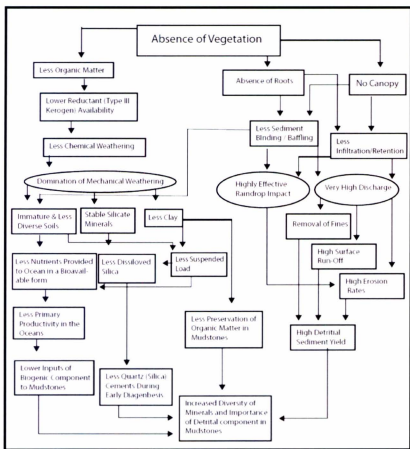


Figure 1.1: Flow chart demonstrating the significant and interconnected chemical (right) and physical (left) impacts a lack of vegetation on the Earth's surface may have created for the deposition of fine grained rocks.

CO-AUTHORSHIP STATEMENT

In the first semester of this Masters the Thesis author conducted a literature review and research proposal. During the progression of the Thesis, modifications to the original proposal were made based on collaborative discussions between Dr. Joe Macquaker, Dr. Graham Layne and the Thesis author.

This thesis is a compilation of three papers, each of which will be submitted to peer-reviewed research journals.

The Thesis author conducted all of the research surrounding the objective of this investigation, literature review, selection of samples, sample collection, sample analysis and manuscript writing. Exceptions to this are noted in the text of the manuscript and include: (i) TOC analysis, which was sent to the Manchester Metropolitan University (MMU), (ii) stable isotope analysis of carbon and oxygen which were conducted at the Environmental Isotope Laboratory in the Earth and Environmental Science Department at Waterloo University, (iii) SIMS analysis for Chapter 2 that was conducted by Glenn Piercey of the CREAT Network at Memorial University on sulfide grains selected by the Thesis author, using rounded grain mounts prepared and imaged by the Thesis author, and (iv) the ITRAX core scan was conducted with significant technical support from Dr. Jonathon Turner at the University College Dublin on samples prepared by the Thesis author.

Dr. Joe Macquaker provided valuable guidance on the direction of the research, discussion of the results at various stages of research and editorial comments during the writing of the manuscript and Thesis. Dr. Graham Layne provided considerable insight

that further modified the direction of this Thesis, as well as providing significant editorial comments during the Thesis writing and editing process.

2. : HIGH-RESOLUTION FACIES ANALYSIS AND MARCASITE FORMATION IN THE TYPE SECTION OF THE FINE-GRAINED EXSHAW FORMATION

2.1. INTRODUCTION

Black shale units are common throughout the Devonian in North America and have been intensely studied by a number of researchers (Angulo and Buatois, 2012; Milliken et al., 2007; Ross and Bustin, 2009; Sageman et al., 2003; Schieber, 2011; Schmoker, 1981). The existence of these fine-grained organic carbon-rich units has been recently linked to the presence of a large igneous province (LIP) that was present close to the Frasnian-Famennian boundary, which caused increased global nutrient runoff into the oceans basins (Trabucho-Alexandre et al., 2010). This runoff fuelled primary production within the ocean and is thought to have caused widespread bottom water anoxia and organic carbon preservation. While the presence of an enhanced nutrient supply may have resulted in increased primary production within the oceans (Trabucho-Alexandre et al., 2010) (and thus greater organic matter concentrations), it does not necessarily follow that all basins where organic carbon was being preserved had ambient depositional conditions that were low and anoxic bottom waters were developed.

In this study the Late Devonian organic carbon-rich Exshaw Formation of Western Alberta is used as a natural laboratory to investigate the geochemical conditions in the water column and sediment pore water at the time of deposition. Deposition of the Exshaw Formation was associated with a period when nutrient inputs may have been effected by the presence of a high LIP frequency, creating bottom waters which have commonly been interpreted to have been low energy and sulfidic. In order to investigate

the conditions that were associated with the emplacement of these strata, this study investigates lithofacies variability, coupled with variations in the sulfide geochemistry. Lithofacies variability was analyzed to gain insights into the environment of deposition and subsequent diagenesis. Sulfur isotope variation in iron-disulfides was also investigated, to determine the depositional and early diagenetic processes that controlled sulfur dynamics and rock character. Varying iron-disulfide mineralogy (proportion of marcasite to pyrite) is particularly significant because it provides insight into the geochemical conditions (oxygen concentrations, pH and redox) at the time of deposition (Berner, 1984; Rickard and Luther, 2007; Schieber, 2007; Wilkin et al., 1996) in particular if oxygenation events disrupted the prevailing anoxic conditions (Schieber, 2007; Schieber, 2011).

2.2. BACKGROUND ON IRON-DISULFIDES

In the reducing environments common in pore waters of sediment in marine environments, near the sediment water-interface, sulfate is transformed through either biotic (bacterial sulfate reduction) or abiotic (thermochemical sulfate reduction) processes to hydrogen sulfide or elemental sulfur (Froelich et al., 1979; Harrison, 1958; Machel et al., 1995). In this reduced form sulfur commonly reacts with iron to form a number of iron sulfide minerals, including pyrite and marcasite (Rickard and Luther, 2007). Pyrite is one of the most common minerals in the marine sedimentary record and is frequently encountered in mudstones (Berner, 1984; Canfield, 2001; Rickard and Luther, 2007). Marcasite, a dimorph of pyrite, has been much less commonly identified in marine deposits, however recent exhaustive surveys coupled with advances in petrographic techniques suggest its prevalence may be greatly underestimated,

particularly in fine-grained units (Rickard and Luther, 2007; Schieber, 2011). Precipitation of marcasite relative to pyrite is distinctive because - while both require reducing pore water conditions with either free H_2S or HS^- available - marcasite specifically requires $pH < 6$ to precipitate (Murowchick and Barnes, 1986; Rickard and Luther, 2007; Schoonen and Barnes, 1991). The pore waters in normal marine sediments are typically buffered to approximately $pH 7 - 8$ by the alkalinity of seawater and therefore a source of acidity must be created in order for marcasite to precipitate rather than pyrite (Rickard and Luther, 2007; Schieber, 2011).

One possible source for this acidity is through the oxidation and dissolution of previously formed pyrite - with the reprecipitation of marcasite occurring in the ensuing acidic, and reducing, conditions (Schieber, 2011). Such a mechanism would operate close to the seafloor. Marcasite, however, is also a common component in sedimentary ore-deposits (Kuhlemann et al., 2001; Leach et al., 2010; Myers and Nealson, 1988; Stoffell et al., 2008). Sediment hosted lead-zinc (Pb-Zn) deposits often contain assemblages of metal-sulfide minerals including pyrite (FeS_2), marcasite (FeS_2), sphalerite ($(Zn,Fe)S$), galena (PbS) chalcopyrite ($CuFeS_2$) and millerite (NiS). In these Pb-Zn deposits, marcasite is directly associated with the post-indurational migration of metal-rich brines and - while it is often observed replacing pyrite - is epigenetic and not associated with pyrite oxidation in soft sediments close to the seafloor (Leach et al., 2010). In these circumstances dissolved sulfur is not wholly derived from oxidized pyrite, but may instead be derived from (either bacterial or thermochemical) alteration of sulfur rich organic carbon, and/or sulfate minerals (e.g. gypsum or anhydrite) (Kuhlemann et al., 2001; Vandeginste et al., 2007).

Stable isotopes of sulfur may represent a useful tool in determining the formation mechanism of sedimentary iron-sulfides (i.e. marcasite and pyrite) (Canfield, 2001; Peevler et al., 2003). To utilize $\delta^{34}\text{S}$ signatures of pyrite and marcasite for interpreting formation pathways it is necessary to trace the potential fractionations that can occur prior to and during sulfide formation. The following discussion summarizes potential formation pathways and associated sulfur isotope dynamics, which include:

- The oxidation of pyrite and reprecipitation of pyrite; with steps of potential $\delta^{34}\text{S}$ fractionation including: sulfate reduction, pyrite formation, pyrite oxidation and the precipitation of marcasite.
- Lead-Zinc type deposits, with potentially isotopically distinct sources of sulfur including:
 - Sulfides from the bacterial sulfate reduction of organic matter
 - Sulfur derived from bacterial reduction of evaporites or anhydrites
 - Sulfur derived from thermochemical reduction of evaporites or anhydrites

2.3. FORMATION PATHWAY 1: OXIDATION OF PRIMARY PYRITE AND REPRECIPITATION OF MARCASITE

2.3.1. Sulfate reduction and associated sulfur isotope fractionations

In this pathway for marcasite precipitation, the initial pyrite is exposed to elevated oxygen (or another oxidant) concentrations sometime after initial formation. This is most likely to occur during early diagenesis in close proximity to the sediment water interface where oxidants are readily available. In this context the sulfate is likely derived from seawater and reduced to sulfide by bacterial sulfate reduction.

The biochemistry of microbial sulfate-reduction involves four steps with each having potential $\delta^{34}\text{S}$ fractionations (Canfield, 2001; Harrison and Thode, 1957; Kemp

and Thode, 1968; Rickard and Luther, 2007). However, the actual degree of fractionation, however, occurring through bacterial sulfate reduction can vary significantly due to a number of kinetic isotope effects. In the reducing environment the general range of fractionation attributed to bacterial sulfate reduction (sulfate to hydrogen sulfide) is approximately -2.0 to -42.0 ‰ (Detmers et al., 2001). Once hydrogen sulfide forms it is commonly oxidized and has the potential to produce a number of intermediate species of sulfur such as sulfite (⁻⁴), elemental sulfur (⁰), or thiosulfate (^{-1, -5}) (Canfield, 2001). Recycling between these intermediate stages can result in significant kinetic isotope fractionations.

2.3.2. Pyrite formation and associated sulfur isotope fractionations

The basic reaction for iron sulfide formation involves the initial precipitation of a thermodynamically unstable iron sulfide mineral that reacts with available sulfur (e.g. reaction 1) (Berner, 1967; Morse et al., 1987; Rickard and Luther, 2007).



There is little to no fractionation of $\delta^{34}\text{S}$ associated with the subsequent formation of pyrite with laboratory experiments recording only +0.9 ‰ fractionation (Price and Shieh, 1979)

2.3.3. Pyrite Oxidation

Once pyrite is formed it may undergo an oxidative dissolution reaction, which results in the sulfur from pyrite being transformed back into sulfate (Rimstidt and Vaughan, 2003). The oxidant required for this process has traditionally been suggested to be oxygen, however in modern systems $\text{Fe(III)}_{\text{aq}}$ has been identified as the primary oxidant (Balci et al., 2007; Schieber, 2011).

If O₂ is the oxidant the general overall reaction for the oxidation is expressed by reaction 2 (Balci et al., 2007) .



If Fe(III)_{aq} is the primary oxidant the general reaction for the process would be similar to reaction 3 (Balci et al., 2007).



Typically, during bacterial and abiotic oxidation of iron-sulfides the mineral surface dissolves layer by layer without any significant sulfur isotopic fractionation. Experimental studies have shown only a +0.7 ‰ fractionation (Balci et al., 2007).

The requirement of low pH conditions for marcasite precipitation is satisfied by the oxidation of pyrite, which not only releases ferrous iron and sulfate but also produces acidity (H₂SO₄) (Schieber, 2007). This creates a microenvironment around the pyrite, lowering the pH of the pore waters. Acid formation can be compounded further via the oxidation of ferrous iron to ferric iron through reaction 4.



This reaction releases added acidity further lowering the pore-water pH conditions.

2.3.4. Precipitation of Marcasite

Through this pathway, reducing and low pH pore water conditions are created that meet the two primary requirements for marcasite formation. The subsequent precipitation of marcasite itself is not related to any substantial net fractionation of isotopes (Canfield, 2001).

2.3.5. Summary of $\delta^{34}\text{S}$ fractionations in Formation Pathway 1

In pathway 1, the most significant fractionation occurs in the initial sulfate reduction stage. The fact that pyrite formation/oxidation and marcasite formation have little to no associated net fractionation means that any marcasite formed through this process should have a very similar $\delta^{34}\text{S}$ signature to the initial pyrite which was initially oxidized (i.e. the source of sulfur). The whole process and associated fractionation ranges are presented in Table 2.1. Temperature can exert small kinetic isotope effects on the magnitude of fractionation that occurs. The described ranges generally take into consideration this variability, however it is worth noting that these ranges are for normal marine conditions with normal temperatures for the upper sediment in close proximity to the sediment water interface ($\sim 10^\circ\text{C}$) (Canfield, 2001).

Combining the total fractionation of all steps suggests that the net fractionation that occurs through this process should yield a range $\delta^{34}\text{S}_{\text{marcasite}}$ of -15.0 to -65.6 ‰ (Canfield, 2001; Detmers et al., 2001).

2.4. FORMATION PATHWAY 2: LEAD-ZINC TYPE DEPOSIT

It is well established that some Pb-Zn type deposits are derived from hot, saline metal-bearing basinal brines driven laterally through aquifers (Kendrick et al., 2002; Sverjensky, 1986). Variations are possible in the mechanism of brine flow and the substrate(s) through which the brine passes. However, the factor that most influences the $\delta^{34}\text{S}$ signature of any precipitating iron-sulfides is the pathway by which H_2S is generated and mixed with the brine (Anderson and Garven, 1987; Helgeson et al., 1984; Sverjensky, 1986) Three potential sources of sulfur are discussed below.

2.4.1. Lead-Zinc Type deposit with sulfides from the bacterial sulfate reduction of organic matter

One potential source of sulfur is from biogenic sulfate reduction resulting from the decomposition of organic matter in the sediment near the location of sulfide precipitation. Bacterial sulfate reduction along with associated fractionations is discussed in detail above, however the overall fractionation would leave a slightly different signature due to the fact that pyrite is not being formed and oxidized prior to marcasite formation Table 2.2. Without the step of precipitating and oxidizing pyrite the degree of fractionation occurring to ^{34}S would yield a range of -15.0 to -64.0 ‰ for $\delta^{34}\text{S}_{\text{marcasite}}$ (Canfield, 2001; Detmers et al., 2001).

2.4.2. Lead Zinc Type deposit with sulfur derived from bacterial reduction of evaporites or anhydrites

In this environment either dissolved gypsum or anhydrite is reduced to create hydrogen sulfide, with consequent dolomite precipitation (e.g. reaction 5):



If a brine flow carries aqueous metal ions through the area where H_2S is generated, or if H_2S is transported through diffusion and subsequently encounters metal ions, metal sulfides will precipitate (e.g. reaction 6) (where M represents a variety of metals including lead, zinc, nickel and iron) (Leach et al., 2010).

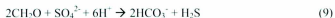


One of the products in reaction 6 is acidity (H^+), which results in an increase in pore water acidity, thus creating the low pH conditions (pH <6), required for marcasite formation.

The most significant influence on the $\delta^{34}\text{S}$ signature of sulfide minerals produced through this potential pathway is the reduction of the initial sulfate. The dissolution of gypsum or anhydrite (reaction 5) may have occurred at some depth, or it may have happened closer to the sediment water interface. With this uncertainty neither bacterial sulfate reduction nor thermochemical reduction can be ruled out. For bacterial sulfate reduction the process (associated fractionations of $\delta^{34}\text{S}$) would be the same as that discussed in detail above and outlined in Table 2.2.

2.4.3. Lead Zinc Type deposit with sulfur derived from thermochemical reduction of evaporites or anhydrites

Machel et al (1995) determined a reaction scheme for thermochemical sulfate reduction (reactions 7 to 9, where R represents high molecular weight reactive organic compounds; alkanes or alkenes).



Significant isotopic fractionation occurs during the initial abiological breaking of the S-O bond. This process is thought to be highly temperature dependant with about a -20.0 ‰ fractionation for a temperature of 100°C, -15.0 ‰ at 150°C and -10.0 ‰ at 200°C (Harrison and Thode, 1957; Machel et al., 1995). In natural environments similar fractionation values have been observed, however a near-zero fractionation (e.g. -1.0 ‰ to -7.0 ‰) for $\delta^{34}\text{S}$ is more commonly identified (Machel, 2001; Machel et al., 1995). Near-zero fractionation is believed to be a result of nearly quantitative conversion of all sulfates which were present in an essentially closed system (i.e. Rayleigh fractionation)

(Machel et al., 1995). The total fractionations associated with such a pathway are outlined in Table 2.3.

The amount of fractionation occurring in ^{34}S through this process would yield a range of 1.5 to -18.5 ‰ in $\delta^{34}\text{S}_{\text{marcasite}}$. (Canfield, 2001; Detmers et al., 2001).

2.5. MATERIALS AND METHODOLOGY

Samples were collected from the Exshaw Formations type section in Jura Creek, near the town of Exshaw in Alberta, Canada. In the field a detailed log description was recorded and a total of 24 samples were collected across a 5.4 m vertical section exposed in a river bank (Field Location in Figure 2.1).

To generate the descriptions of grain size, fabric, composition and facies designations present on a range of scales, polished, unusually thin (20-25 μm) sections were prepared from the collected samples. These sections were initially described using an optical petrographic microscope (Nikon Optiphot Pol). Following this the sections were coated with carbon and analyzed both texturally and compositionally using an FEI Quanta 400 environmental scanning electron microscope (SEM) equipped with an electron Backscattered (BSE) and an energy dispersive X-ray (EDS) analytical system. The SEM was operated at 25 kV and 2.0 μA ; with a working distance of 12 mm. This process follows similar techniques of earlier studies (Macquaker and Gawthorpe, 1993).

For bulk quantitative analyses, 18 mudstone samples were comminuted using tungsten carbide grinding bowls. Between each sample grinding, a bowl of ultra-pure silica was crushed to prevent contamination and all tools and surfaces were thoroughly cleaned with ethanol. A number of analyses were conducted on powdered samples. Mineralogical composition was analyzed using a Rigaku Ultima IV X-ray Diffractometer

(XRD) with a copper cathode X-ray source and a scintillation counter detector. X-ray fluorescence (XRF) spectrometry was utilized to determine the concentration of major and trace elements. For this analysis 5 mg of mudstone powder was weighed and mixed with a 0.7 gm of phenolic resin binder. After mixing, this powder was placed in a Herzog Pellet Press and pressed for 10 seconds at 20 ton/in² pressure. The pellet was then baked at 200°C for 15 minutes. The operating conditions of the XRF followed those of Longerich (1995). Total organic carbon analysis was conducted at the Manchester Metropolitan University (MMU) in a Leco Induction Furnace. In this technique total carbon contents of each sample were initially determined. The samples were then decalcified using warm 2% HCl, and the decalcified carbon contents were determined using the same Leco furnace. The TOC contents of each sample were then determined by difference. A sub-set of samples were selected to be analyzed for $\delta^{13}\text{C}$ isotopic analysis that was conducted by the Environmental Isotope Laboratory in the Earth and Environmental Science Department at Waterloo University.

A sub-set of samples were selected for isotopic analysis of $\delta^{34}\text{S}$ in iron disulfide minerals through Secondary Ion Mass Spectrometry (SIMS) with a Cameca IMS 4f ion microprobe equipped with a modernized ion detection system to augment performance for stable isotope analysis. Prior to this analysis separate circular mounts (25.4 mm in diameter) were created from individual samples and polished to a flat sample surface. Each of the circular mounts was characterized and mapped with an optical petrographic microscope under reflected light and in some cases also using the SEM described above for BSE imagery.

2.6. GEOLOGICAL HISTORY

The Exshaw Formation was deposited close to the Devonian-Carboniferous boundary in the Western Canada Sedimentary Basin. Due to the absence of *sulcata* and *praesulcata* conodont zones in the unit the Devonian-Carboniferous (D-C) boundary has not been accurately constrained at Jura Creek (Macqueen, 1970). The thickness of the formation varies throughout the Prophet Trough on the cratonic platform in western Alberta with the thickest section occurring in southwestern Alberta (Raasch, 1956; Smith and Bustin, 2000). Based on conodont biostratigraphy the Exshaw Formation is stratigraphically equivalent to the Bakken Formation, which extends in the subsurface throughout the Williston basin (Figure 2.1) (Johnston, 2010; Savoy et al., 1999).

At Jura Creek the Exshaw Formation overlies the bioturbated Palliser Formation, which contains *Thalassinoides* *isp.*, replaced with chert (Johnston, 2010). The eastern section of the formation stratigraphically overlies carbonates of the Big Valley Formation (Smith and Bustin, 2000). The boundary between the Exshaw Formation and the underlying carbonate units is recognized as the Acadian Unconformity, during which a drop in relative sea level occurred resulting in erosion and reworking of the underlying sediments (Smith and Bustin, 2000).

The lower member (9.3 m at the Jura Creek type section) of the Exshaw Formation (Figure 2.2) has been described as being composed of brownish-black, fossiliferous shale at the base of which is a phosphate-rich lag deposit with sand-sized detrital quartz, and a significant early diagenetic component (Macqueen, 1970). The upper member of the Exshaw Formation (37.4 m thick at Jura Creek) has been described as a sparsely fossiliferous, bioturbated, calcareous siltstone (Smith and Bustin, 2000). The top of the Exshaw Formation is separated from the fine-grained mudstones of the Lower

Banff Formation by a sharp contact (Smith and Bustin, 2000). Previous researchers have measured total organic carbon (TOC) concentrations in the Exshaw formation of 21 %, and average Hydrogen Index (HI) values of 515 mg Hg/g (Caplan and Bustin, 1999).

The Exshaw Formation has commonly been interpreted as having been deposited in a quiescent basin with anoxic bottom waters. Research has pointed to the fine-grained fabric and high organic matter concentrations to support this description. The lag deposit identified at the base of the type section has previously been interpreted to represent a transgressive surface (Smith and Bustin, 2000). The Exshaw is a particularly useful natural laboratory for this study because it represents very typical black shale deposit which has previously thought to be formed in a stagnant environment with anoxic bottom waters (Caplan and Bustin, 1996; Caplan and Bustin, 1999; Macqueen, 1970; Smith and Bustin, 2000).

2.7. RESULTS

Five different lithofacies were identified, on the basis of varying grain size, mineralogy and textural attributes in this succession. These include both fissile sandstones and thin-bedded mudstones. The individual units exhibit a variety of lamina geometries and diagenetic features. Detailed descriptions of each lithofacies are given below and their stratigraphic distributions are shown on Figure 2.2.

2.7.1. Clay-bearing sulfide-bearing arkose sandstone

At the base of the Exshaw Formation's type section in Jura Creek Alberta is a 30-mm thick, clay-bearing, diagenetic sulfide-bearing, arkose sandstone (Figure 2.3). This unit is a lag deposit with coarse (100 to 250 μm) grains of quartz and feldspar grains (sanidine) with some phosphate (Figure 2.3 A). There is no visible bedding within this

relatively thin unit (Figure 2.3 A-B). Mineralogically, this facies is composed of 30.4 % feldspar (predominantly sanidine with minor amounts of orthoclase), 25.1 % quartz, 17.3 % pyrite, 15.2 % apatite, 10.6 % calcite (Table 2.4). Minor amounts of dolomite, rutile and a range of sulfide minerals (marcasite, sphalerite and millerite) were detected during EDS analyses. This facies was determined to have a TOC content of 1.56 % and a $\delta^{13}\text{C}_{\text{OM}}$ of -28.1 ‰ (Table 2.4). Using bulk samples calcite was measured to have a $\delta^{13}\text{C}_{\text{calcite}}$ of -0.4 ‰ and $\delta^{18}\text{O}_{\text{calcite}}$ of -6.7 ‰. (Table 2.4).

The feldspar grains have irregular and well-defined grain boundaries and likely have a detrital origin (Figure 2.3 E). Some of the feldspar grains, however, have undergone partial dissolution and been replaced by quartz (Figure 2.3 E). Quartz cement also encloses detrital quartz grains (Figure 2.3 D-E). A distinct erosion surface is present at the top of this unit (Figure 2.3 C). Above this surface the framework grains are composed of finer-grained apatite, quartz and pyrite, compared to the coarse-grained framework material below this surface (Figure 2.3 C).

Diagenetic pyrite is present in both framboidal and euhedral forms (Figure 2.3 D-F). In addition to pyrite, marcasite, sphalerite, and millerite, cements are also present (Figure 2.3 D, F, Figure 2.9). SIMS analysis of individual grains of pyrite and marcasite identified significant variability in $\delta^{34}\text{S}$, with an overall range of +14.5 ‰ to -38.6 ‰ throughout the succession (Figure 2.8; Figure 2.9). Marcasite was the most enriched in ^{34}S of all samples with a range of +6.3 ‰ to +14.5 ‰ (Figure 2.8; Figure 2.9). Measured pyrite clustered in two regions; -8.1 ‰ to -14.9 ‰ and -30.7 ‰ to -38.6 ‰ (Figure 2.8; Figure 2.9).

2.7.2. Thin bedded dolomite cement-rich mudstone

Directly above the arkose sandstone is a thin unit (~ 50 mm) of parallel-bedded and normally graded silica and dolomite-cement-rich mudstones (Figure 2.4). Beds in this part of the succession have wavy bases (Figure 2.4 A-C). The framework fraction is composed of detrital quartz and feldspar minerals and ranges in size from 5 to 25 μm . Zoned dolomite suggesting a diagenetic origin contributes up 40 % of the volume of the unit (Figure 2.4 E-F). Both the detrital quartz grains (coarse silt-size) and dolomite cement rhombohedra are coarser at the base of the individual beds than they are towards the bed tops, where the grains are dominated by clay-size material (Figure 2.4 C-F). This facies contains 36 % quartz, 12.7 % pyrite, 11.2 % clay (illite) as well as minor amounts of apatite (Table 2.4). TOC content of this facies was measured to be 4.1 % with a $\delta^{13}\text{C}_{\text{OM}}$ of -28.0 ‰ (Table 2.4). Bulk samples of dolomite had a $\delta^{13}\text{C}_{\text{dolomite}}$ of -3.4 ‰ and $\delta^{18}\text{O}_{\text{dolomite}}$ of -3.6 ‰ (Table 2.4). $\delta^{34}\text{S}$ of individual pyrite grains from this unit had an overall range of -4.4 ‰ to -7.3 ‰.

Individual beds of these facies are commonly organized into stacked successions of bed-sets that form units up to 1.5 m thick.

2.7.3. Thin-bedded silt and pyrite-bearing clay-rich mudstone

Directly above the unit with an extensive dolomite cement is a thin-bedded silt and pyrite-bearing clay rich mudstone (Figure 2.5). The framework minerals, which have a grain size ranging from 10 to 25 μm , are composed of a mix of silt-sized feldspars and quartz (Figure 2.5 C-D). The matrix is composed of clay-sized quartz, feldspars and clay (Figure 2.5 C-D).

This facies is very similar to other thin-bedded facies with the exception that it contains pyrite (Figure 2.5 C-D). The other key distinction of this facies is that it does not contain sulfur in the form of gypsum, which is common in the other facies. Overall the facies is composed predominantly of quartz (62.2 %) clay (illite) (17.7 %), feldspar (orthoclase) (17.6 %), and pyrite (2.5 %) (Table 2.4). The TOC content of this facies was measured to be 4.7 % with a $\delta^{13}\text{C}_{\text{OM}}$ of -28.1 ‰ (Table 2.4). $\delta^{34}\text{S}$ of individual pyrite grains from this unit had an overall range of -2.7 ‰ to -7.7 ‰.

2.7.4. Thin-bedded normally graded silt-bearing silica-rich mudstone

The most common facies throughout the Lower Exshaw Formation is a thin-bedded normally graded silt-bearing silica-rich mudstone (Figure 2.6). The framework grains in this facies range in size from 10 to 50 μm and are oriented parallel to bedding. These units contain a significant amount of quartz (59 %) (Table 2.4). This quartz occurs in a variety of forms including: silt sized detrital grains, radiolaria tests and as discrete infill of *Tasmanites* tests (Figure 2.6 F). Some of the quartz is also present as early diagenetic cement infilling uncompact pore spaces (Figure 2.6 E-F). The matrix is predominantly quartz with some smaller grains of clays (illite) (22.2%), and feldspar (18.1 %) (Table 2.4). Both veins and discrete grains of gypsum were found throughout this facies. Gypsum was also noted during the visit to the outcrop to be forming a crust on the surface of the succession (Figure 2.6 F). The average TOC content of this facies were 4.3 % with an average $\delta^{13}\text{C}_{\text{OM}}$ of -28.5 ‰ (Table 2.4).

Lenticular shaped bodies ranging from 200 to 500 μm in length and 20 to 30 μm thick were found to be quite common (Figure 2.6 C-E) in these units. SEM analysis of these bodies reveals them to be composed of clay to silt sized feldspar grains (Figure 2.6

E). Some of these bodies enclose an elongate pore space, while in others compaction seems to have destroyed this porosity. Based on these features these bodies are interpreted to be the remains of agglutinated benthic foraminifera with tests composed of clay to silt sized detrital feldspar (based on well defined and irregularly shaped grain boundaries). In some cases these features may be silicified algal cysts (Figure 2.6 E-F)

Individual beds of these facies are commonly organized stacked successions of bed-sets that form units up to 2 m thick.

2.7.5. Calcite cement-dominated mudstone

Calcite cement-dominated mudstone form discrete units throughout the Exshaw Formation. This facies is primarily composed of calcite cement (64.5 %), which precipitated early (Table 2.4). In addition these units contain subordinate amounts of quartz (28.9 %), pyrite (4.1 %), feldspars (1.3 %) and illite (0.75 %) (Table 2.4). The framework grains in this facies range in size from 3 to 60 μm . Quartz is present mainly as diagenetic cement, although minor amounts of clay sized detrital grains also occur (Figure 2.7 D-E). Quartz cement often forms a rim around the edges of detrital grains (e.g. quartz cement around an albite grain in Figure 2.7 E). This relationship suggests the diagenetic quartz precipitated from the silica rich pore space fluids created from the dissolution of these elastic detrital grains (Figure 2.7 D-E). In this facies, large > 1 mm nodules of quartz were found in some areas (Figure 2.7 C-D). No visible bedding planes were identified in this facies (Figure 2.7 A-B). Organic matter in this unit has a $\delta^{13}\text{C}_{\text{OM}}$ of -28.1 ‰ (Table 2.4). Using bulk samples, calcite has a $\delta^{13}\text{C}_{\text{calcite}}$ of -4.7 ‰ and $\delta^{18}\text{O}_{\text{calcite}}$ of -8.3 ‰ (Table 2.4).

The paragenetic succession of cementation in these units is complicated, as illustrated by the fact that early calcite cementation grain dissolution was followed by the precipitation of euhedral pyrite (Figure 2.7 B-F) and ultimately quartz. SIMS analysis showed that the $\delta^{34}\text{S}$ of individual pyrite grains from this unit had a range of +1.8 ‰ to -1.2 ‰.

2.8. DISCUSSION

2.8.1. Lithofacies interpretation

At Jura Creek the basal unit of the Exshaw Formation is a clay-bearing iron sulfide-rich arkosic arenite that unconformably overlies the carbonates of the Palliser Formation. Directly above this interval, separated by a sharp contact (Figure 2.3 C), is a thin-bedded dolomite cement-bearing mudstone. The stratigraphic context of these basal units relative to the underlying carbonates suggests that additional accommodation became available over this interval and that it is a transgressive surface. The presence of abundant early diagenetic iron-sulfides and non-ferroan dolomite in these basal beds suggests that the pore water were anoxic and sulfidic (Berner, 1984). Based on enclosing relationships of grain boundaries there were multiple events of iron-sulfide precipitation in the basal arkosic unit. The transition between the two units reflects a shift in grain size from sand sized detrital grains (100 to 250 μm) in the lag deposit to silt-sized (3 to 25 μm) grains of the dolomite-bearing mudstone. Therefore the amount of energy being supplied to the seafloor decreased as flooding continued and the likely effects of wave reworking were reduced (Mckay et al., 1995). The presence of wave ripples on the top of bedding surfaces in the dolomite facies indicate that while the amount of energy decreased (i.e. no longer able to transport sand sized grains) the basin did not become

completely stagnant. Based on $\delta^{13}\text{C}$ of dolomite and petrographic analysis dolomite cement precipitation at this level is likely linked to microbial sulfate reduction occurring in the sediment pore-waters (Figure 2.4 E-F; Table 2.4) (Warren, 2000; Whitaker and Smart, 1990). In this context sulfate reduction is important because it removes otherwise inhibiting sulfate from the pore waters which had been limiting dolomite precipitation when the pore-waters, were oxic (Warren, 2000; Whitaker and Smart, 1990).

Abruptly overlying the basal dolomite is a stacked succession of thin relict bedded silt and pyrite-bearing clay-rich mudstone that forms a unit approximately 0.5 m thick. This unit is a transitional zone that was probably deposited as the basin was deepening. Carbonate concretions are present towards the top of this unit. The presence of diagenetic pyrite and the undisrupted nature of the laminae suggests that in this part of the succession the pore-waters and potentially the bottom waters were reducing and sulfidic. The concretionary horizon likely represent a maximum flooding surface (MaxFS) where a break in sediment delivery occurred and there was sufficient time for enough solutes to be transported to sites of precipitation and infill the large, pre-compaction volumes of intergranular pore space (Raiswell, 1988; Raiswell and Fisher, 2000). Analyses of the enclosing relationships between the cement phases (see Figure 2.7) suggests that following the initial period of cement precipitation there appears to have been grain dissolution (primarily of feldspars). Resulting porosity was subsequently filled by later-stage silica and pyrite (euhedral) cement (Van Cappellen, 2003; Vorhies and Gaines, 2009). A similar surface occurs near the top of the measured succession and may represent either a parasequence boundary or, potentially, a sequence boundary.

The succession above the maximum flooding surface is composed mainly of clay and silt-bearing silica cement-rich mudstones. In this part of the succession the strata vary from thin relict bedded to laminated. Many of the individual beds are normally graded and some contain agglutinated foraminifer. The normal grading suggest that deposition was likely from waning flows where these flows were driven by storm events (Aplin and Macquaker, 2011). The relict bed fabrics suggest that organisms (e.g. agglutinated foraminifer) were able to colonize the sediment in some intervals and disrupt the depositional fabrics. The presence of lamination reflects higher recurrence frequencies of sedimentation episodes (e.g. storm events). Agglutinated benthic foraminifera occur commonly and are often detected in close proximity to *Tasmanites* (Figure 2.6) (Schieber, 1996). The presence of abundant agglutinated foraminifera, provide evidence for at least some oxygen being present in the water column at the time of deposition (Milliken et al., 2007; Schieber, 2009).

2.8.2. Metal Disulfide Analysis

As previously outlined, petrographic analyses (backscattered electron imaging and optical petrography) of the basal arkosic unit identified sulfide cements of varying forms that precipitated both early and late. In addition to pyrite and marcasite, millerite and sphalerite were also found to be present in assemblages intergrown with marcasite (e.g. Figure 2.3; Figure 2.9). The presence of millerite and sphalerite that post-dates precipitation of at least some pyrite suggests that nickel and zinc, in addition to iron, must have been available in the pore waters during the interval when later metal disulfides were precipitating. A total of three populations of $\delta^{34}\text{S}$ were identified in the measured pyrite and marcasite of the basal arkosic unit (Figure 2.8).

The first population contained only pyrite and was the most depleted in $\delta^{34}\text{S}$, with a range of -30.7 ‰ to -38.6 ‰. This pyrite was preserved as either framboids, degraded relict framboids or as larger euhedral grains. The $\delta^{34}\text{S}$ of pyrite in this range is within the common range for pyrite precipitated as a result of biogenic sulfate reduction in an open system with free exchange to the overlying water column (i.e. not Rayleigh or closed system fractionation) (Canfield, 2001). In Figure 2.9 B marcasite appears to be growing around a cluster of degraded framboidal pyrite, further suggesting that this pyrite precipitated prior to marcasite formation. Based on this and other textural relationships with surrounding minerals, the pyrite in this population appears to be the earliest sulfide preserved in the rock (Figure 2.9).

The second $\delta^{34}\text{S}$ population, found only in pyrite, had a range of -8.1 ‰ to -14.9 ‰. The pyrite in this group was euhedral (e.g. Figure 2.9 C). This population is isotopically heavier by +15.8 ‰ to +30.5 ‰ than the first group described. The distinct difference of the two $\delta^{34}\text{S}$ populations suggests different sources of sulfur for pyrite precipitation. When combined with analysis of mineral boundaries from petrographic data it appears that this pyrite formed at a later stage of precipitation, after the compaction of the sediment (epigenetic). In this case both thermochemical and biogenic sulfate reduction were potential sources of sulfur for pyrite.

The $\delta^{34}\text{S}$ of pyrite beyond the arkosic unit, in the rest of the measured Exshaw Formation succession, was found to be similar to the second population, with a range of -2.7 ‰ to -7.7 ‰ (Figure 2.8). Assuming a similar formation mechanism between population two in the arkosic unit and the pyrite throughout the overlying succession, the small isotopic difference between the two groups may be related to a reservoir effect.

Available sulfur may have become enriched from the older to younger sediments, in the essentially closed system that existed during continued precipitation at depth.

The third, and isotopically heaviest, population of measured $\delta^{34}\text{S}$ - with a range of +6.3 ‰ to +14.5 ‰ - was only detected in marcasite. The presence of corroded framboidal pyrite nodules in the same unit suggests that marcasite may have formed from the pyrite precipitation/oxidation process, with the initial pyrite not completely being oxidized (Schieber, 2011). Based on $\delta^{34}\text{S}$ measurements from previous studies, the $\delta^{34}\text{S}$ of sulfate in seawater during the Upper Devonian (Famennian) was between +18.0 and +30.0 ‰ (Claypool et al., 1980; Kaplan, 1975). With this initial range, marcasite precipitated from these pore waters would have $\delta^{34}\text{S}$ values ranging from +15.0 to -47.6 ‰. This is within the range of measured marcasite values, although at the heavy end of the spectrum – implying contemporaneous seawater with a $\delta^{34}\text{S}$ range of +29.5 to +21.3 ‰.

However, marcasite $\delta^{34}\text{S}$ was significantly different from either of the two populations of pyrite - with a minimum difference of +14.4 ‰ and a maximum of +53.1 ‰. The oxidation of pyrite and reprecipitation of marcasite combined for a total fractionation ranging from +0.0 to +0.7 ‰. If this process occurred multiple times, (i.e. repeated cycles of pyrite formation, oxidation and marcasite precipitation) a larger fractionation is possible, however this would actually cause the $\delta^{34}\text{S}$ of marcasite to become more negative. It is therefore difficult to explain through this process how the $\delta^{34}\text{S}$ of marcasite is much more enriched than the pyrite from which it potentially originated. This scenario also fails to explain the elevated concentrations of zinc and nickel in the pore waters of this unit implied by intimate association of millerite and

sphalerite with the marcasite (e.g. Figure 2.3; Figure 2.9). Trace metal concentrations in the arkosic unit relative to the rest of the formation further suggest the source of material entering the depositional area had a different and more metal-rich origin (Figure 2.10). High sediment concentrations of trace metals (i.e. zinc, lead, copper, and nickel) are not typical in normal marine environments and therefore require some unique source delivering a relatively significant influx of these metals. This influx appears to have only occurred at one specific interval in the measured succession.

Lead-Zinc type mineralization mechanisms represent an alternative for the formation of marcasite, which may better explain the conditions in the arkosic unit (Leach et al., 2006). A formation mechanism similar to a Pb-Zn deposit would have a sulfur source either transported to the area (could be from younger or older strata due to biogenic or thermochemical sulfate reduction) or derived in the deposit itself (e.g. dissolution of sulfate-bearing minerals such as barite). Once basinal metal-rich brine was driven through the formation and encountered this pool of reduced sulfur, metal-sulfides would be rapidly precipitated (e.g. reaction 10).



The low-pH conditions created by the precipitation of metal-sulfides lead to marcasite precipitation rather than pyrite. These acidic conditions also resulted in the dissolution of existing carbonate minerals (esp. calcite) in the unit.

The exact source of sulfur in this latter scenario is interesting to consider. It is not likely that sulfides were derived from bacterial sulfate reduction during the oxidation of organic matter, because this process itself does not yield or require the low pH conditions needed to favour marcasite formation over pyrite. A more likely source could be that

sulfur was derived from the reduction of local evaporites. Whether this process is occurring from the bacterial reduction of evaporite sulfates or from thermochemical reduction cannot be definitively determined. Minor amounts of barite in the arkosic unit; suggest that the source of dissolved sulfate minerals may have been the unit itself (Figure 2.9). The fact that the arkosic unit is sandstone further supports this theory as i) regional fluid flow occurs much more easily and potentially for much longer; and ii) the unit was potentially acrially exposed, allowing for evaporite (gypsum or anhydrite) minerals to form.

Large scale Pb-Zn deposits formed by regional flow of basinal brines occur across the Western Canada Sedimentary Basin e.g. the Pine Point, Robb Lake, Kicking Horse and Monarch ore deposits (Leach et al., 2001; Vandeginste et al., 2007).

2.9. CONCLUSIONS

The results of the lithofacies investigation suggest that during the deposition of this formation the basin was not as persistently stagnant as previous research has suggested. While it is clear that oxygen concentrations in the sediment were quite low, agglutinated benthic foraminifera suggest that oxygen was present in the bottom waters of the basin. The presence of ripples and graded bedding throughout the formation also suggests that there was at least some advective transport, indicating the bottom waters were not persistently low energy, and were at least episodically impacted by storm waves.

Marcasite has been identified in a number of Devonian mudstones (black shales) (Schieber, 2011) and recent research has suggested that the most likely reason for its formation is the oxidation of pyrite and reprecipitation of marcasite process (Schieber,

2007; Schieber, 2011). However, this is the first known stable isotope analysis of sulfur in these lag deposits and thus offers new insight as to the formation of these sulfides.

Assuming marcasite formed as a result of pyrite oxidation and re-precipitation, very little difference between the $\delta^{34}\text{S}$ of pyrite and marcasite would be expected due to the fact that there is little to no fractionation associated with the coupled oxidation of pyrite and consequent formation of marcasite in a relatively closed system. Furthermore, the pyrite oxidation and re-precipitation theory fails to explain the co-occurrence of other metal sulfides (e.g. sphalerite and millerite). This sulfur isotope analysis suggests that there were multiple sources of sulfur in the system during the deposition of the basal arkosic arenite. In this deposit the most plausible formation pathway for marcasite appears to be a process similar to the one that precipitates Pb-Zn deposits. That is, a relatively open system (esp. for metals) with the potentially long-range transport of a migrating metal-rich brine to the depositional area. This likely happened at some depth of burial, as it is possible that due to the large grain sizes and subsequently greater porosity, the migratory brine was able to preferentially enter the arkosic bed after initial deposition. Based on the isotopic signature, it would seem that thermochemical sulfate reduction of an evaporite or other sulfate mineral may be the most likely source of sulfur for marcasite precipitation.

Similar to recent research this study demonstrates that these fine-grained sedimentary units are also very heterogeneous. It is unrealistic to suggest that the same process were responsible for all the variability observed. An array of hydrodynamic processes were likely dispersing the sediment and responsible for varying rates of sediment accumulation and resulting diagenetic processes. In much the same way, there

are also a greater variety of diagenetic processes, which can be occurring in these units as indicated by the multiple pathways by which iron disulfide minerals formed. In many fine-grained sedimentary rocks the idea that marcasite is forming from the oxidation of pyrite and reprecipitation of marcasite is certainly accurate. However, this study demonstrates that marcasite precipitation via the oxidation of pyrite is not the only mechanism for marcasite precipitation in mudstones. Therefore the presence of marcasite alone cannot suggest that oxygen (or any other oxidant) was available in the pore-waters during the deposition of a mudstone.

2.10. TABLES

Table 2.1: Fractionation ranges of $\delta^{34}\text{S}$ during each step in the formation of marcasite through the formation and oxidation of pyrite, followed by precipitation of marcasite. Note adenosine 5'-phosphosulfate = APS.

Process		ϵ (‰)
Bacterial Sulfate Reduction (-2 to -42)	Step 1 $\text{SO}_4^{2-}(\text{org}) \rightarrow \text{SO}_4^{2-}(\text{int})$	0 to -3
	Step 2 $\text{SO}_4^{2-}(\text{int}) \rightarrow \text{APS}$	0
	Step 3 $\text{APS} \rightarrow \text{SO}_3^{2-}$	-9 to -24
	Step 4 $\text{SO}_3^{2-} \rightarrow \text{H}_2\text{S}$	-6 to -37
Pyrite Formation		0 to -0.9
Pyrite Oxidation		0 to -0.7
Marcasite Formation		0

Table 2.2: Fractionation ranges of $\delta^{34}\text{S}$ during each step in the formation of marcasite through a basinal brine meeting sulfur from a bacterial sulfate reduction of organic matter source.

Process		ϵ (‰)
Bacterial Sulfate Reduction	Step 1 $\text{SO}_4^{2-}(\text{org}) \rightarrow \text{SO}_4^{2-}(\text{int})$	0 to 3
	Step 2 $\text{SO}_4^{2-}(\text{int}) \rightarrow \text{APS}$	0
	Step 3 $\text{APS} \rightarrow \text{SO}_3^{2-}$	-9 to -24
	Step 4 $\text{SO}_3^{2-} \rightarrow \text{H}_2\text{S}$	-6 to -37
Marcasite Formation		0

Table 2.3: Fractionation ranges of $\delta^{34}\text{S}$ during each step in the formation of marcasite through the reduction of sulfate from an evaporitic or gypsum source using either bacterial sulfate reduction (scenario 1) or thermochemical reduction (scenario 2) for the reduction of sulfate.

Process		ϵ (‰)
Evaporate Formation		+1.5
Thermochemical Sulfate Reduction (Theoretical)		0 to -20
Marcasite Formation		0

Table 2.4: Analytical Results of Exshaw Formation

LOC	156	417	448	497	334	417	312	046	310	349	413	432	310	340	414	188	337
Major elements																	
SiO ₂	58.1	58.0	58.1	58.0	58.3	58.4	58.7	57.5	58.7	58.6	58.6	58.5	58.7	58.3	58.4	58.0	58.5
TiO ₂	0.8	0.8	0.8	0.8	0.8	0.8	0.8	0.8	0.8	0.8	0.8	0.8	0.8	0.8	0.8	0.8	0.8
Al ₂ O ₃	4.7	4.7	4.7	4.7	4.7	4.7	4.7	4.7	4.7	4.7	4.7	4.7	4.7	4.7	4.7	4.7	4.7
FeO	25.1	26	27.2	26.9	25.6	25.1	25.3	25.3	25.9	25.3	25.3	25.4	25.6	25	25.3	25	25.5
MnO	13.2	13.7	13.3	13.8	13.4	13.5	13.3	13.3	13.3	13.0	13.0	13.0	13.3	13.3	13.3	13.3	13.3
MgO	17.8	17.7	17.3	17.3	17.3	17.3	17.3	17.3	17.3	17.3	17.3	17.3	17.3	17.3	17.3	17.3	17.3
CaO	1.2	1.2	1.2	1.2	1.2	1.2	1.2	1.2	1.2	1.2	1.2	1.2	1.2	1.2	1.2	1.2	1.2
Na ₂ O	18.6	18.6	18.6	18.6	18.6	18.6	18.6	18.6	18.6	18.6	18.6	18.6	18.6	18.6	18.6	18.6	18.6
K ₂ O	27.2	27.2	27.2	27.2	27.2	27.2	27.2	27.2	27.2	27.2	27.2	27.2	27.2	27.2	27.2	27.2	27.2
Sum	136	136	136	136	136	136	136	136	136	136	136	136	136	136	136	136	136
Trace elements																	
As	3.2	3.2	3.2	3.2	3.2	3.2	3.2	3.2	3.2	3.2	3.2	3.2	3.2	3.2	3.2	3.2	3.2
Br	15.2	15.2	15.2	15.2	15.2	15.2	15.2	15.2	15.2	15.2	15.2	15.2	15.2	15.2	15.2	15.2	15.2
Cr	38.4	38.4	38.4	38.4	38.4	38.4	38.4	38.4	38.4	38.4	38.4	38.4	38.4	38.4	38.4	38.4	38.4
Major elements																	
SiO ₂	51.0%	51.0%	51.0%	51.0%	51.0%	51.0%	51.0%	51.0%	51.0%	51.0%	51.0%	51.0%	51.0%	51.0%	51.0%	51.0%	51.0%
TiO ₂	0.6%	0.6%	0.6%	0.6%	0.6%	0.6%	0.6%	0.6%	0.6%	0.6%	0.6%	0.6%	0.6%	0.6%	0.6%	0.6%	0.6%
Al ₂ O ₃	6.0%	6.0%	6.0%	6.0%	6.0%	6.0%	6.0%	6.0%	6.0%	6.0%	6.0%	6.0%	6.0%	6.0%	6.0%	6.0%	6.0%
FeO	27.8%	27.8%	27.8%	27.8%	27.8%	27.8%	27.8%	27.8%	27.8%	27.8%	27.8%	27.8%	27.8%	27.8%	27.8%	27.8%	27.8%
MnO	10.0%	10.0%	10.0%	10.0%	10.0%	10.0%	10.0%	10.0%	10.0%	10.0%	10.0%	10.0%	10.0%	10.0%	10.0%	10.0%	10.0%
MgO	13.0%	13.0%	13.0%	13.0%	13.0%	13.0%	13.0%	13.0%	13.0%	13.0%	13.0%	13.0%	13.0%	13.0%	13.0%	13.0%	13.0%
CaO	1.0%	1.0%	1.0%	1.0%	1.0%	1.0%	1.0%	1.0%	1.0%	1.0%	1.0%	1.0%	1.0%	1.0%	1.0%	1.0%	1.0%
Na ₂ O	11.0%	11.0%	11.0%	11.0%	11.0%	11.0%	11.0%	11.0%	11.0%	11.0%	11.0%	11.0%	11.0%	11.0%	11.0%	11.0%	11.0%
K ₂ O	19.0%	19.0%	19.0%	19.0%	19.0%	19.0%	19.0%	19.0%	19.0%	19.0%	19.0%	19.0%	19.0%	19.0%	19.0%	19.0%	19.0%
Sum	100%	100%	100%	100%	100%	100%	100%	100%	100%	100%	100%	100%	100%	100%	100%	100%	100%

2.11. FIGURES

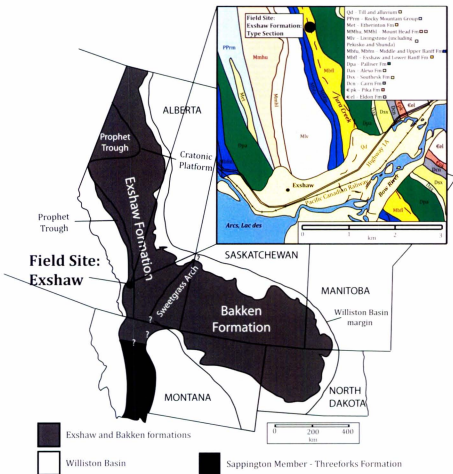


Figure 2.1: Map demonstrating the extent of the Exshaw and associated Bakken Formations. Inset is a map of the regional geology around the Field location, which is in Jura Creek near the town of Exshaw in the Rocky Mountains of Alberta, Canada. Modified from Asgar-Deen and Adams (2010), Price (1970), and Smith and Bustin (2000).

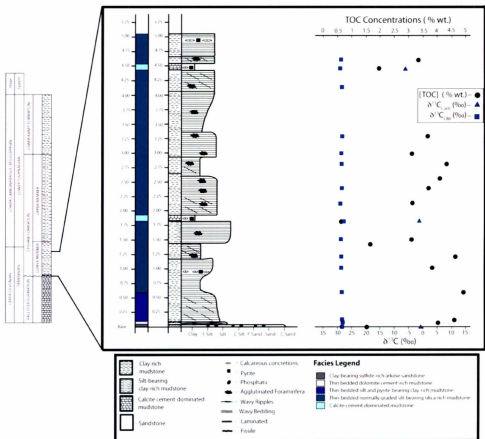


Figure 2.2: Stratigraphic log of the measured section of the Exshaw Formation at its type section in Jura Creek, Alberta.

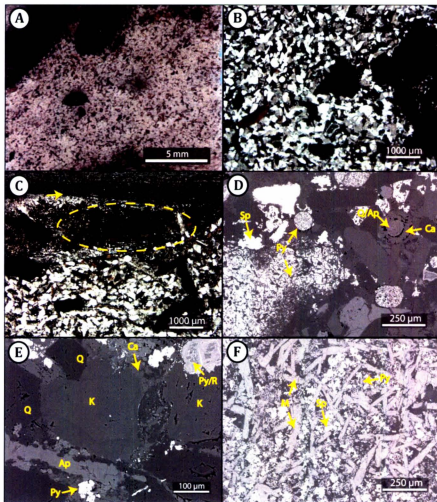


Figure 2.3: Petrographic observations of clay-bearing sulfide-rich arkose sandstone. (A) Scan of thin section showing large grain sizes and sulfide minerals. (B and C) Optical images from petrographic microscope. Erosive surface is arrowed in C. (D to F) Backscatter electron optical micrographs. Note wide range of diagenetic minerals in (E) and (D). A large amount of marcasite intergrown with pyrite and sphalerite can be seen in (F) Mineralogy is arrowed and labeled as: Q – quartz, Ca – calcite, Ap – apatite, R-rutile, Pl – plagioclase, Py – Pyrite, M – marcasite and Sp – sphalerite.

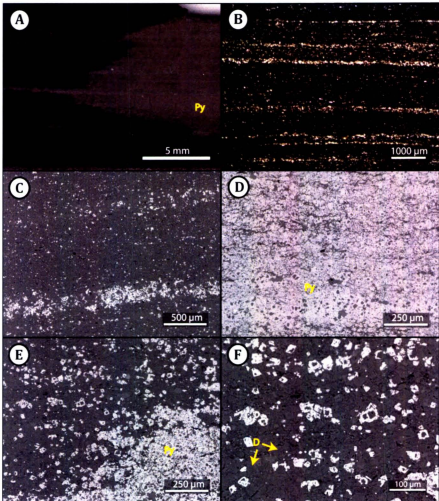


Figure 2.4: Petrographic observations of thin-bedded dolomite cement-rich mudstone. (A) Scan of thin section showing the large extent of pyrite within this facies. (B) Optical image from petrographic microscope, note the thin normally grading beds. (D to F) Backscatter electron optical micrographs. Pyrite is very extensive in a euhedral form, often forming the base of thin beds. Mineralogy is arrowed and labeled as: Py – Pyrite, D – Dolomite.

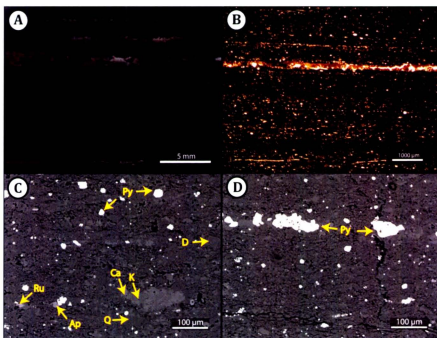


Figure 2.5: Petrographic observations of thin-bedded silt and pyrite-bearing clay-rich mudstone. (A) Scan of thin section showing very clay rich fabric. (B) Optical image from petrographic microscope demonstrating the thin-bedded nature of the facies. (C to D) Backscatter electron optical micrographs. Pyrite occurs throughout this facies in a cubedral form. Mineralogy is arrowed and labeled as; Q – quartz, Ca – calcite, Ap – apatite, D – dolomite, Ru-rutile, and Py – Pyrite.

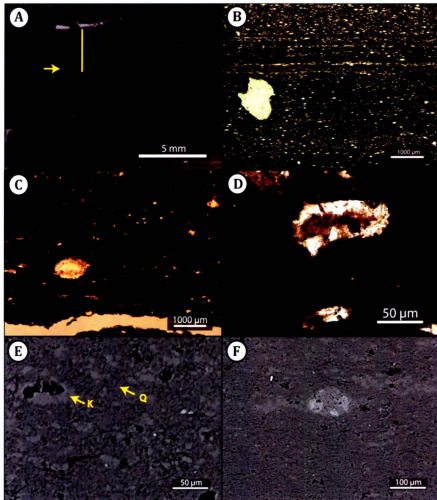


Figure 2.6: Petrographic observations of thin-bedded normally graded silt-bearing silica-rich mudstone (A) Scan of thin section showing very clay rich fabric. A solid line highlights the normally grading nature of the facies with an arrow pointing at the silt-rich base of a bed. (B-D) Optical images from petrographic microscope. (C and D) show agglutinated benthic foraminifera, which are common in the facies (E and F) Backscatter electron optical micrographs. An agglutinated benthic foraminifera can be seen in (E) with K-feldspar making up the test and a cavity, which is either empty or filled with organic matter. Mineralogy is arrowed and labeled as: Q – quartz and K – feldspar.

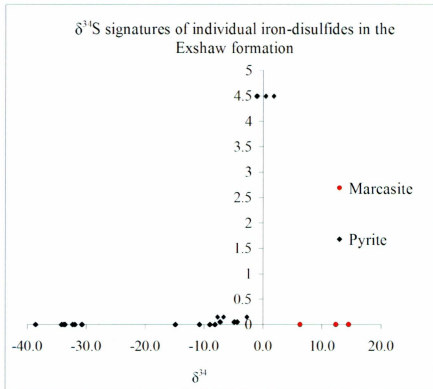


Figure 2.8: Results of SIMS analysis with $\delta^{34}\text{S}$ plotted against the height above the base of the measured section of the Exshaw Formation. Note: although pyrite was detected at other intervals of the stratigraphic log, individual grain sizes were too small to accurately measure $\delta^{34}\text{S}$ with the SIMS.

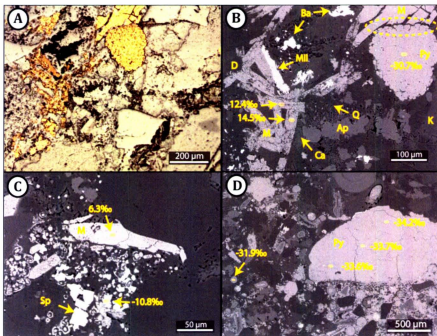


Figure 2.9: Petrographic observations of the clay-bearing sulfide-rich arkose sandstone showing ^{34}S measurements of marcasite and pyrite. (A) Optical images from petrographic microscope in reflected light. (B to D) Backscatter electron optical micrographs of the circular mounts, which were analyzed for ^{34}S . In (B) the boundary between a cluster of degraded framboidal pyrite and bladed marcasite is circled with a dash line. The marcasite can be seen growing around the pyrite suggesting a later precipitation of the marcasite. Mineralogy is arrowed and labeled as; Q – quartz, Ca – calcite, Ap – apatite, D – Dolomite Py – Pyrite, M – marcasite, Mil – Millerite and Sp – sphalerite.

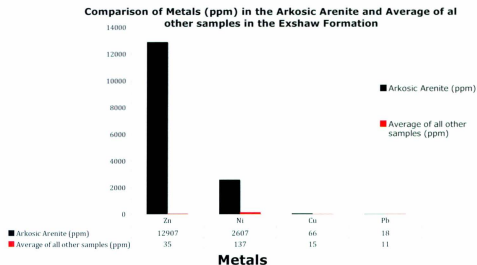


Figure 2.10: Graph comparing the amount of elemental metals in the basal arkosic unit to all other facies in the Exshaw Formation.

3. : HIGH-RESOLUTION ANALYSIS TO DETERMINE CONTROLS ON CARBON SEQUESTRATION AND MINERALIZATION IN ORDOVICIAN SHALE GAS TARGETS

3.1. INTRODUCTION

Conventional scientific understanding of organic-rich fine-grained rocks is that they are deposited from suspension settling in anoxic basins. Recent research, however, has highlighted that in spite of similar superficial appearances at hand specimen scales, fine-grained rocks (including shales) are highly variable in: (a) grain sizes as reflected in differing silt to clay ratios, (b) compositions, (c) proportions of materials derived from detrital inputs to basins, primary production within basins and subsequent diagenesis and (d) microtextural attributes, particularly lamination style, and bioturbation (Baas et al., 2009; Bohacs et al., 2005; Macquaker et al., 2010a; Macquaker and Bohacs, 2007; Piper and Calvert, 2009; Schieber et al., 2007; Van Cappellen, 2003). This variability indicates that they were not simply deposited from buoyant plumes via suspension settling in quiescent anoxic environments, but are products of deposition in much more dynamic settings, which then suffered complex dysoxic and anoxic diagenetic overprinting (Piper and Calvert, 2009). Stratified redox profiles in the lower water column and sediment pore waters, combined with varied hydrodynamic/sediment transport mechanisms, cause these rocks to exhibit significant unrecognized variability in a range of parameters from porosity to elemental (e.g. carbon) concentrations. The carbon cycle is of particular importance to this heterogeneity because it controls the balance of carbon preserved in reduced and oxidized states, resulting in organic carbon sequestration and mineralization. Heterogeneity within the carbon cycle of the Earth's oceans is driven by sediment

delivery mechanisms and the availability of oxidants, which then drive the stratification of microbially mediated early diagenetic reactions.

In the Earth's oceans, carbon is primarily present in an oxidized form, as dissolved inorganic carbon (Falkowski et al., 2000). Other pools of carbon in the oceans include reduced particulate organic carbon and carbon in the skeletal (carbonate) and soft parts (organic carbon) of organisms (Falkowski et al., 2000). Much of the carbon contained in the biosphere is cycled to an inorganic form at the sediment water interface, as organic compounds are decomposed via oxidation reactions (e.g. reaction 1) (Claypool et al., 1980) to oxidized carbon species. The most energetically favourable oxidant for this reaction is oxygen.



In dysoxic to anoxic conditions a series of other oxidants will be utilized by this process (e.g. Mn(IV), NO_3^- , Fe(III), SO_4^{2-} , CH_4) (Froelich et al., 1979; Morse et al., 1987). These oxidants, however, are not as energetically favourable as oxygen and the ensuing oxidation reactions using these terminal electron acceptors are neither as efficient or as rapid (Froelich et al., 1979). High primary production rates can lead to a significant amount of reduced carbon being transported to the sediment-water interface, thus causing depletion of available oxidants that are mostly delivered from the overlying water column by diffusion. Thus, periods of high production, combined with high sediment accumulation rates (high recurrence frequency of bed emplacement) and low dilution (from detrital sources) can result in preferential organic carbon preservation within the sediment following consolidation and subsequently lithification (Bohacs et al., 2005; Piper and Calvert, 2009; Sageman et al., 2003). Alternatively, if oxygen is readily

available in the water column and in the pore waters, and sediment accumulation rates are slower, most of the organic carbon will be oxidized (e.g. reaction 1).

This commonly liberates carbon dioxide that will subsequently dissociate into bicarbonate and hydrogen ions (e.g. reaction 2).



In this form, the bicarbonate can react with Ca^{2+} to precipitate calcium carbonate (via reaction 3) (Morse et al., 2007).



Calcium for the formation of calcium carbonate is derived from the weathering and transport of Ca-rich minerals (e.g. feldspars and clays) to the oceans (Aplin and Macquaker, 2011). While Ca^{2+} is ultimately derived from run-off, it is often cycled through the biosphere as organisms use calcium to construct their tests (e.g. bivalves, brachiopods, echinoderms, coccolithophores, foramanifera etc.). This Ca may then be re-dissolved during early burial, particularly if it is in the relatively unstable aragonite or high Mg-calcite forms. Combined with sub-marine weathering of Ca-rich feldspars and clays, the dissolution of such skeletal Ca-bearing organisms living in the water column and in the sediment can supply abundant Ca^{2+} to the pore-waters (Aplin and Macquaker, 2011; Machent et al., 2007; Morse et al., 2007). If the pore waters have reducing (anoxic) conditions a variety of other minerals may form rather than calcium carbonate, including rhodochrosite (MnCO_3), which is associated with reduction of MnO_2 (Lovley and Phillips, 1988); magnetite (Fe_3O_4) and siderite (FeCO_3), which have both been associated with Fe(III) reduction (Roh et al., 2003); pyrite (FeS_2), which forms during sulfate

reduction (Newton and Bottrell, 2007; Rickard and Luther, 2007); and/or ferroan dolomite or ferroan calcite (CaCO_3), which are associated with methanogenesis.

In this way, carbonate cement can precipitate in the pore waters of pre-compaction mudstones, forming either individual concretions or continuous cemented layers where they coalesce (Morse et al., 2007). Acidic pore waters can lead to grain dissolution, which often enhances porosity given minimal clay mineralization after dissolution (Siegel and Pfannkuch, 1984).

From a source rock/reservoir perspective the relative balance between the two spheres of carbon (oxidized and reduced) is important because it influences both; i) the abundance of inorganic carbonate (oxidized) and ii) the overall organic content (reduced) (Aplin and Macquaker, 2011; Morse et al., 2007; Ross and Bustin, 2009) of the sediment. The inorganic carbon fraction is particularly significant, as it exists either as preserved skeletal fragments derived from production in the basin, or in diagenetic cements. The form of cement is likely to play a significant role in the source rock/reservoir quality of a shale succession.

3.2. AIMS AND OBJECTIVES

This study aims to investigate the relationship between i) cycling among the carbon spheres of reduced and oxidized forms and ii) the heterogeneity observed in fine-grained sediments and, in particular, the spatial and temporal distributions of organic carbon and different carbonate minerals. To this end, the controls on carbon cycling in two Ordovician-aged carbon rich mudstone successions, the Utica Shale, and the Winterhouse Formation will be examined. These two successions are ideal natural laboratories for this investigation because they are of the same age (mid to late

Ordovician), were deposited in the same tectonostratigraphic domain (the Lower-Middle Paleozoic autochthonous St. Lawrence Platform), and formed in related depositional settings (previously near-shore carbonate platforms moving into continental shelf) (Dietrich et al., 2011). Even with these similarities, the expectation is that, due to the wide range of heterogeneity recently documented in mudstones, significant differences will exist between the two successions-causing them to exhibit different source rock and unconventional reservoir attributes.

3.3. GEOLOGICAL SETTING

The break-up of Rodinia during the late Neoproterozoic to early Paleozoic created the basin in which the St. Lawrence Platform was deposited. This platform itself formed in the early Paleozoic (Cambrian to Devonian) depositing sediment in shallow marine and near shore environments of the Laurentian continental shelf (Dietrich et al., 2011). On-land deposits from this platform are found from the St. Lawrence Lowlands of southern Quebec eastward to the Mingan Islands, Anticosti Island and western Newfoundland. This unit is also found offshore in the St. Lawrence estuary and the Northern Gulf of St. Lawrence.

Sediment was deposited along the eastern margin of Laurentia during the Taconic orogeny. This sedimentation deposited shallow to deep carbonate and clastic units in disconnected tectonically active foreland basins along the eastern margin of Laurentia (Dietrich et al., 2011; Knight, 1992). In western Newfoundland this created a number of carbonate and clastic deposits including the Table Head Group, Goose Tickle Group and the Long Point Group (Dietrich et al., 2011). The Winterhouse Formation, one of two units investigated for this study, was deposited during the Middle to Upper Ordovician

Period as part of the Long Point Group, exposed on the Long Point Peninsula of the Port au Port Peninsula in south-western Newfoundland, Canada (Figure 1) (Bergstrom et al., 1974; Quinn et al., 1999). Previous studies have identified the Winterhouse as being composed of thinly bedded, calcareous silty shales, to quartzose sandstones and occasional limestone (Bergstrom et al., 1974; Gillespie, 1998). The Long Point Formation is composed of the Winterhouse Formation and the underlying middle Ordovician Lourdes Limestone that has a gradational boundary with the Winterhouse (Bergstrom et al., 1974). Overlying the Winterhouse Formation is the Silurian-Devonian Clam Bank Formation (Williams S.H., 1989; Williams S.H., 1987).

In Southern Quebec the Taconic Foreland basin, which formed in the Middle-Upper Ordovician, contained both carbonates (Black River and Trenton groups) and what have been described as deep marine clastic deposits (Utica Shale). The Utica Shale was deposited in the Upper Ordovician in the Taconic Foreland basin (Hannigan and Basu, 1998; Mitchell et al., 1994). The Utica conformably overlies the carbonates of the Trenton group (Brett and Baird, 2002). The reason for the shift to more clastic dominated material has been suggested to be an increase of sea level due to tectonic activity associated with collisions of an island arc (Taconic Terrane) along the margins of Laurentia.

The fact that the Utica and the Winterhouse are of similar age and were deposited in foreland basins of the St. Lawrence Platform creates a useful comparison of the two fine-grained units as (i) similar weathering processes theoretically influenced sediment entering both basins and (ii) production derived components should be relatively similar.

3.4. MATERIALS AND METHODOLOGY

Samples were collected from 1) the Utica Shale in the St. Lawrence Lowlands of southern Quebec (Figure 3.1) and 2) the Winterhouse Formation on the Port Au Port Peninsula of Western Newfoundland (Figure 3.10). Detailed log description was recorded at each location. Two locations were visited at the Utica field location, with a total of 33 samples collected, 23 from a 4 m measured section at the base of the Utica and 10 from a 3 m section near the middle of the formation (field locations shown in Figure 3.1). In the Winterhouse Formation a total of 20 samples were collected across a 5.4 m vertical section beginning at the base of the formation (field location in Figure 3.10).

To generate the descriptions of grain size, fabric, composition and facies designations present on a range of scales, polished unusually thin (20-25 μm) sections were prepared from the collected samples. These sections were initially described through the use of an optical petrographic microscope (Nikon Optiphot Pol). Following this the sections were coated with carbon and analyzed both texturally and compositionally using an FEI Quanta 400 environmental scanning electron microscope (SEM) equipped with a Backscattered electron imaging (BSE) and an energy dispersive X-ray (EDS) analytical system. The SEM was operated at 25 kV and 2.0 μA ; with a working distance of 12 mm. This process followed similar techniques of earlier studies (Macquaker and Gawthorpe, 1993).

For bulk quantitative analyses, 18 mudstone samples were crushed using a tungsten carbide grinding mill. To minimize cross-sample contamination in the mill, ultra-pure silica was crushed between samples and all tools and surfaces were thoroughly cleaned with ethanol. The mineralogical composition of each sample was determined

using a Rigaku Ultima IV X-ray Diffractometer (XRD) with a copper $K\alpha$ X-ray source equipped with a scintillation counter detector.

X-ray fluorescence (XRF) spectrometry was utilized to determine concentration of major and trace elements. For XRF analyses 5 mg of sample was weighed and mixed with a 0.7 gm of phenolic resin binder. After mixing, this powder was placed in a Herzog Pellet Press and pressed for 10 seconds at 20 ton/in² pressure. The pellet was then baked at 200°C for 15 minutes. The operating conditions of the XRF are described in Longrich (1995). Total organic carbon analysis was conducted at the Manchester Metropolitan University (MMU) in a Leco Induction Furnace. The samples were then decalcified using warm 2% HCl, and the decalcified carbon contents were determined using the same Leco furnace. The TOC contents of each sample were then determined by difference. A sub-set of samples was selected for $\delta^{13}\text{C}$ isotopic analysis at the Environmental Isotope Laboratory in the Earth and Environmental Science Department at Waterloo University.

3.5. RESULTS

Lithofacies present are classified using the nomenclature scheme proposed by Macquaker and Adams (Macquaker and Adams, 2003) for mudstones (sedimentary rock composed of > 50% grains < 0.063 mm). In this scheme the lithofacies names are based on the percentage abundance of materials of either different grain size or different origin within a mudstone. For instance, mudstone beds containing >90% of a particular grain size are described as being “dominated” by that component; units that contain between 50 to 90% of a particular grain size are described as being “rich” in that component; whereas materials that comprise 10 to 50% of a particular grain size are described as “bearing” the component. With modifiers (e.g. thin bedded, laminated, burrowed,

homogenized, fossiliferous) being added to the beginning of the name to describe its textural attributes, and its compositional attributes (e.g. siliceous, calcareous, dolomitic, silicilastic) being added to the end of the name. Using this terminology the mudstones in the Utica and Winterhouse Formations can be described in detail and compared.

3.5.1. Utica Formation

Two short sections within the Utica Shale were measured and logged for this study. The first was a 4 m thick succession along the banks of the Jacques Cartier River at the base of Utica Shale where it gradationally overlies the Trenton Formation (UC field location in Figure 3.1). The second, which represents the middle of the Utica Shale, was a 3 m succession, located in a road cut in near the town of Cap-Sante, QC, (UCB field location in Figure 3.1).

On the basis of varying grain size, mineralogy, grain origin and textural attributes eight lithofacies (described below) were identified in the Utica Shale. The lithofacies present include both homogenized and very thin-bedded (bed thicknesses ranging from 1 mm to 20 mm) mudstones with varying proportions of calcite cements (from 46 to 80 %). Internally, the individual units exhibit a variety of lamina geometries and are variably bioturbated. Detailed descriptions of each lithofacies are given below and their stratigraphic distributions are shown in Figure 3.2.

3.5.1.1. (U1) Normally graded, very thin bedded, pelleted, silt-bearing, clay-rich carbonate mudstone

This facies is organized into sharp based, very thin (1 to 5 mm thick), normally graded beds that are silt-enriched at their bases (grain size approximately 25 μm) and clay-rich towards their tops (grain size $<4 \mu\text{m}$) (see Figure 3.3 A-C). Prominent, compacted pellets are visible throughout (Figure 3.3 C). The silt sized framework grains

(~20 μm) are composed of detrital quartz, feldspars and broken pieces of reworked calcite skeletal debris (Figure 3.3 D). The matrix is composed of clay sized quartz, feldspar, and illite (Figure 3.3 C-D). While most of the quartz is found primarily in the form of detrital grains, euhedral overgrowths are also present (Figure 3.3 C). Similarly calcite is primarily present as silt-sized reworked skeletal grains, but is also present in minor amounts of early diagenetic pore filling cement. Other forms of early diagenetic cement included zoned dolomite and minor amounts of framboidal pyrite and barite (Figure 3.3 C – D). Overall the mineralogical abundances were determined to be calcite (46 %), quartz (15.6 %), illite (17.7 %), dolomite (12.5 %), albite (6.1 %), and pyrite (2.1 %) (Table 3.1, Table 3.2). Total organic carbon abundance was measured to be 1.5 % and have a $\delta^{13}\text{C}_{\text{organic}}$ signature of -30.2 ‰ (Table 3.1, Table 3.2).

Individual beds of these facies are commonly organized into stacked successions of bed-sets that form units up to 0.5 m thick.

3.5.1.2. (U2) Thin-bedded partly homogenized, silt- clay- and carbonate cement-bearing mudstone

Thin-bedded partly homogenized, silt- clay- and carbonate cement-bearing mudstones contain discontinuous, relic bedding planes > 5 mm thick (Figure 3.4). Internally the majority of the primary textures have been homogenized (Figure 3.4 A). The overall grain size in this facies ranges from <3 to 40 μm . This facies is very calcareous (51%). The calcite is present primarily as finely comminuted bioclastic debris (preserved as elongated angular grains) in the silt-sized fraction, and as cement (Figure 3.4 B-D). Compressed fecal pellets composed of very fine-grained calcite are present (Figure 3.4 A-C). Some burrow mottles are visible and these are attributed tentatively to either *Thalassinoides isp.* and/or *Planolites isp.* Quartz occurs primarily as sub-rounded

detrital, silt-sized grains although there is also clay sized quartz in the matrix and minor amounts of quartz cement (Figure 3.4 C and D). The most common cement in this facies is dolomite (Figure 3.4 D). Pyrite, which is also occurs throughout the facies, forms either discrete grains or circular/crushed elongated 100 μm nodules composed of framboids (or relict framboidal). The overall mineralogical composition of this facies is calcite (51 %), dolomite (9.5 %), illite (13 %), quartz (13 %), anorthite (4.5 %), chlorite (3.6), orthoclase (2.9 %), and pyrite (0.7 %) (Table 3.1, Table 3.2). Dispersed organic matter was identified in thin section analysis and the total organic carbon content was measured to be 1.2 % and have a $\delta^{13}\text{C}_{\text{org}}$ signature of -29.8 ‰ (Table 3.1, Table 3.2).

3.5.1.3. (U3) Normally graded, ripple laminated, very fine sand, coarse silt and fecal-pellet bearing carbonate mudstone

Thin beds of normally graded very fine sand, coarse silt and fecal-pellet-bearing carbonate mudstones are common in the Utica Formation. These units have grain sizes ranging from clay to very fine sand (3 to 100 μm) (Figure 3.5). Internally the individual beds are organized into non-parallel lamina sets that exhibit down-lapping geometries on to the underlying bedding planes (Figure 3.5 B). The bases of the individual beds are defined by thin lags composed of coarse silt (Figure 3.5 A-C). While fecal pellets are present throughout the facies, they are particularly abundant at the tops of individual beds (Figure 3.5 B-C). These fecal pellets are composed of a mixture of very fine-grained clay, quartz, feldspars and dolomite (Figure 3.5 D). Dolomite appears to primarily occur within these fecal pellets, in contrast outside of the pellets the dominant carbonate cement calcite (although carbonate cement is not very abundant in this facies) (Figure 3.5 D-F). Most of the calcite is present in the form of broken silt-sized skeletal debris, with varying morphologies (round to elongated) (Figure 3.5 E). Round nodules ranging from 0.1 to 0.5

mm in length and approximately 0.1 mm in width are common; in some areas they have been filled with either the precipitation of silica (quartz) cement or what is presently slightly degraded framboidal pyrite (Figure 3.5 C and F). In some areas these nodules have been crushed during compaction resulting in an elongated pattern oriented along bedding planes (Figure 3.5 C). Uncompacted nodules indicate cement that precipitated prior to compaction. The overall mineralogical composition of the slide is calcite (51.4 %), illite (16.7 %), dolomite (15.5 %), quartz (14.4 %), pyrite (0.6 %), and apatite (1.4 %) (Table 3.1, Table 3.2). The total organic carbon content of this facies was measured to be 1.6 % (Table 3.1, Table 3.2).

Individual beds of these facies are commonly organized into stacked successions of bed-sets that form units up to 3 mm thick.

3.5.1.4. (U4) **Thin-bedded, normally graded, silt- and very fine sand-bearing calcite-cement-rich mudstone**

Thin-bedded, normally-graded, silt and very fine sand bearing calcite-cement-rich mudstones, with sharp and uneven erosional surfaces at the base of each event bed, contain framework grains of very fine sand sized quartz, feldspar and broken fossil debris (in the form of calcite) (Figure 3.6). Individual beds are normally graded and have a distinct coarse rich section at the base grading upward into a more fine-grained unit on top (Figure 3.6 B-C). There are multiple forms of diagenetic cements including calcite, dolomite (as evidenced by zonation), barite and degraded framboidal pyrite (Figure 3.6 E-F). The overall mineralogical composition of the facies is calcite (67.1 %), dolomite (9.3 %), illite (8.6 %), anorthite (7.5 %), quartz (3.6 %), chlorite (3.5 %), and pyrite (0.4 %) (Table 3.1, Table 3.2). The total organic content of this facies is 0.35 % (Table

3.1, Table 3.2). In the bulk carbonate samples the $\delta^{13}\text{C}_{\text{calcite}}$ of was measured to be +1.2 ‰ and the $\delta^{18}\text{O}_{\text{calcite}}$ -5.0 ‰ (Table 3.1, Table 3.2).

Individual beds of these facies are commonly organized into stacked successions of bed-sets that form units ranging from 1 to 50 mm thick.

3.5.1.5. (U5) Normally graded, burrow mottled silt- and clay-bearing calcite cement-rich mudstone

This normally graded, burrow mottled silt- and clay-bearing calcite-cement-rich mudstone is primarily composed of calcite cement however some silt and very fine sand size (3 to 100 μm) framework grains are present (Figure 3.7). The framework grains are composed of quartz, broken skeletal debris (in the form of calcite), apatite and feldspars (Figure 3.7 A-C). The matrix is composed of clay minerals and pyrite. The bed bases are sharp based and commonly overlain by lags composed of skeletal debris (Figure 3.7 B). Burrowing has completely homogenized some beds and partially disrupted the tops of others (Figure 3.7 A-B). The overall mineralogical composition is calcite (77.2 %), dolomite (8.55 %), illite (8 %), quartz (4.3 %), anorthite (0.2 %), rutile (1 %), apatite (0.9 %), chlorite (0.2 %) and orthoclase (0.1 %) (Table 3.1, Table 3.2). The total organic carbon content of this facies is 0.29 % with a $\delta^{13}\text{C}_{\text{OM}}$ signature of -28.6 ‰ (Table 3.1, Table 3.2). In bulk carbonate samples the $\delta^{13}\text{C}_{\text{calcite}}$ of was measured to be +2.8 ‰ and the $\delta^{18}\text{O}_{\text{calcite}}$ -4.1 ‰ (Table 3.1, Table 3.2).

3.5.1.6. (U6) Thin, relict bedded, partially homogenized coarse silt-bearing, clay-rich calcareous mudstone

This thin relict bedded partially homogenized coarse silt-bearing clay-rich calcareous mudstone contains grain sizes with a range of <3 to 50 μm (Figure 3.8). Bioturbation has resulted in the destruction of a large proportion of the original bedding

features (Figure 3.8 A-B). In areas where bedding planes have been preserved it is evident that normally grading is present and there are alternating lamina dominated by shell and clay minerals (Figure 3.8 A-B). In some of these beds ripples have been preserved, and wavy bosses occur overlying erosional surfaces (Figure 3.8 A). The matrix material is composed of a mix of clay-sized quartz, clays, feldspar and broken carbonate debris (Figure 3.8 C). Calcite occurs as both cement and in the form of clay and silt sized broken skeletal debris (Figure 3.8 B-C). Silt to very fine sand sized grains of dolomite are present in a diagenetic form as evidence by the occurrence of zonation within the grains (Figure 3.8 D). Surrounding the dolomite grains is porosity around the grain boundaries (Figure 3.8 D). Minor amounts of diagenetic euhedral pyrite occur as discrete grains throughout (Figure 3.8 C-D). The overall composition of this facies is calcite (61.2 %), illite (16.2 %) quartz (7 %), orthoclase (6.8 %), dolomite (5.4 %), and pyrite (1.5 %) (Table 3.1, Table 3.2).

3.5.1.7. (U7) Thin-bedded and burrow mottled fine silt-bearing, calcite cement-rich mudstone

This silt-bearing calcite cement-rich mudstone contains discontinuous beds with erosive bases, which fine upwards and have grain sizes ranging from clay to fine silt (<3 to 25 μm). This facies contains trace fossils of unlined passive filled *Thalassinoides* and/or *Planolites* burrows (Figure 3.9 A-B). The detrital fraction is composed of reworked skeletal debris (calcite) and small amounts of quartz and feldspars. Quartz is also present as a result of the dissolution of K-feldspar, and formed as cement post-dissolution of other primary minerals (Figure 3.9 E-F). This facies also contains authigenic feldspars (in the form of albite) (Figure 3.9 E-F). Authigenic feldspar was identified based on irregular grain boundaries and the fact that in some areas the albite

forms a rim around other detrital grains (of anorthite) (Figure 3.9 E-F). Pyrite occurs as a diagenetic mineral in both euhedral and framboidal forms (Figure 3.9 C-F). Some fractures in this unit have been filled in with framboidal pyrite (Figure 3.9 C-D). Minor amounts of the zinc-sulfide sphalerite also occur in this facies (Figure 3.9 E). Overall the mineralogical composition is calcite (74.3 %), illite (12.2 %), dolomite (7.2 %), quartz (5.5 %), anorthite (2.75 %), Chlorite (1.9 %), Apatite (0.9), and pyrite (0.4 %) (Table 3.1, Table 3.2). The total organic carbon content of this facies is approximately 0.35 % (Table 3.1, Table 3.2). In bulk carbonate samples the $\delta^{13}\text{C}_{\text{calcite}}$ was measured to be +1.9 ‰ and the $\delta^{18}\text{O}_{\text{calcite}}$ -4.6 ‰ (Table 3.1, Table 3.2).

3.5.2. Winterhouse Formation

A 6 m section of the Winterhouse Formation on the Port-au-Port Peninsula (Field Location in Figure 3.10) was measured and logged. Four different lithofacies were identified in this succession. The lithofacies present include both calcareous sandstones and calcareous mudstones. The individual units exhibit a variety of lamina geometries and are variably bioturbated. Detailed descriptions of each lithofacies are given below and their stratigraphic distributions are shown on Figure 3.11.

3.5.2.1. (W1) Homogenized, calcite-cemented fine-grained calcareous sandstone

The coarsest facies encountered in the Winterhouse Formation is a homogenized calcite-cemented fine-grained calcareous sandstone (framework grains range in size from 125 to 200 μm) (Figure 3.12). This facies forms a prominent unit at the base of the measured succession of the Winterhouse Formation. The framework grains in this unit are mainly composed of quartz with minor feldspar. Concavo-convex quartz grain

contacts between the cement and the framework grains suggest the calcite cement postdates compaction (Figure 3.12 C). Extensive burrowing has homogenized most of the depositional fabrics, however, in some regions there is evidence of preserved lamination (Figure 3.12 A-B). This unit contains significant grain dissolution porosity, produced by the dissolution of unstable feldspars (note relic feldspar grains in Figure 3.12 B-C). The grain dissolution porosity has been subsequently filled by calcite and later stage quartz cement (Figure 3.12 B-C). Overall the facies is composed predominantly of calcite (69.4 %) quartz (14.1 %), Dolomite (6.2 %), Albite (2.9 %), Rutile (2.8 %) apatite (0.9 %), orthoclase (0.4 %), pyrite (0.2 %), and chlorite (0.1 %) (Table 3.3).

3.5.2.2. (W2) Homogenized sand- and silt-bearing calcite cement-rich mudstone

The framework grains in this Homogenized sand- and silt-bearing calcite cement-rich mudstones are composed of silt to sand-sized framework grains (Figure 3.13). These Preserved framework grains are mostly composed of quartz, calcareous skeletal debris and feldspar in the silt-size fraction (Figure 3.13 B-D). Most of the bioclastic material has an uncertain origin, however, echinoderm debris was identified (Figure 3.13 B). Individual burrows are defined by clay-rich cavities with no lining suggesting they are *Planolites isp.* and/or *Thalassinodes isp.* At one boundary with an overlying homogenized sand and silt-bearing calcite cement-rich mudstone facies a hard ground is present. This hard ground contains multiple borings (Figure 3.13 A). Chlorite and apatite were identified through SEM analysis. Small euhedral pyrite grains are scattered throughout this unit.

There were multiple generations of cements prior to compaction in this facies with calcite being the earliest and most extensive and pyrite and calcite enclosing the

early fabrics (Figure 3.13 E-F). Post-compaction (based on the concavo-convex elongate boundaries between the detrital grains) calcite cement infills the intergranular porosity (Figure 3.13 C-D). Calcite cement is also present infilling grain dissolution porosity in voids created by the dissolution of feldspars and other unstable mineral grains (Figure 3.13 D). XRD analysis indicates the overall mineralogical composition is calcite (57.1 %), quartz (16.4 %), orthoclase (2.3%), illite (8.6 %), dolomite (7.6 %), albite (4.1 %), pyrite (0.4 %) and chlorite (2.3 %) (Table 3.3). Total organic carbon was measured at 0.27 % with a $\delta^{13}\text{C}_{\text{OM}}$ signature of -29.1 ‰. In bulk carbonate samples the $\delta^{13}\text{C}_{\text{calcite}}$ of was measured to be -0.4 ‰ and the $\delta^{18}\text{O}_{\text{calcite}}$ -4.0 ‰ (Table 3.3).

3.5.2.3. (W3) Thin relict bedded, partially homogenized clay- and dolomite cement-bearing, silt-rich siliclastic mudstone

This thin relict bedded, partially homogenized clay, silt-rich siliclastic mudstone facies contains burrow mottling and framework grains ranging in size from medium to coarse silt (10 to 50 μm). Bioturbation has resulted in the destruction of most bedding planes; although some relict beds have been preserved (Figure 3.14). There are preserved trace fossils of passively filled and horizontally protrusive *Rhizocoarallium isp.* burrows and *Paleophythus isp.* that contain thin to thick wall linings with a passive fill similar to the host sediment (Figure 3.14 A-C). A large amount of detrital material has been preserved with little evidence of grain dissolution porosity (Figure 3.14 D-F). The detrital framework is composed quartz, feldspars, and clay minerals (chlorite) (Figure 3.14 D-F). There is some cement infilling pore spaces, primarily in the form of dolomite with lesser amounts of calcite (Figure 3.14 D-F). Minor amounts of barite are present as cement (Figure 3.14 E). The overall mineralogical composition is composed of quartz (30.3 %), illite (21.2 %), dolomite (12.7 %), orthoclase (10.5 %) chlorite (7.8 %), calcite (7.8 %),

albite (6.8 %), pyrite (2.9 %) (Table 3.3). Measured total organic carbon was found to be 0.27 % and have a $\delta^{13}\text{C}_{\text{OM}}$ signature of -28.9 ‰ (Table 3.3).

3.5.2.4. (W4) Burrow mottled fine-sand bearing silt-rich mudstone

This homogenized fine sand-bearing silt-rich mudstone contains 10 to 50 μm framework grains 10 to 50 μm grains of quartz, feldspars, and clays (chlorite). Grain dissolution has resulted in the destruction of much of the detrital grains, as many grains have been dissolved and a cement of quartz or calcite has subsequently filled the porosity (Figure 3.15 C-F). This facies contains a burrow-mottled fabric; due to the extensive bioturbation no visible bedding planes have been preserved (Figure 3.15 A-B, D). Portions of some burrows have been preserved as fine-grained rich zones (Figure 3.15 A-B, D). Escape traces have also been preserved with an abundance of clay to fine sand sized minerals (Figure 3.15 A). It is primarily within burrows that diagenetic calcite and dolomite are found (Figure 3.15 D and F). Minor amounts of framboidal pyrite are common throughout the facies (Figure 3.15 C-F). XRD analysis indicates the overall mineralogical composition of this facies is quartz (36.3 %), chlorite (25.4 %), albite (16.8 %), orthoclase (9.8 %), calcite (7.3 %), dolomite (3.8 %), and illite (0.7 %) (Table 3.3). The total organic carbon concentration of this facies was detected to be the highest of any facies in the Winterhouse (although still relatively low compared to other mudstone successions) at 0.31 % with an average $\delta^{13}\text{C}_{\text{OM}}$ signature of -28.9 ‰ (Table 3.3).

3.6. DISCUSSION

3.6.1. Sediment origins, dispersal and bioturbation

As in all fine-grained successions, sediment of the Utica and Winterhouse Formations are derived from both detrital and primary production sources (Aplin and

Macquaker, 2011). Within the individual Formations the relative proportions of detrital and primary production components; proportions of organic carbon and inorganic carbon (carbonate), grain size and transport mechanisms all vary significantly. The following sections address this variability and their link to sediment origins, mechanisms of dispersal and subsequent colonization.

The Utica Shale is organized into stacked successions of: i) thin-bedded, normally graded calcareous mudstones intercalated with ii) more argillaceous calcareous mudstones, on a meter scale. The basal units, immediately overlying the Trenton limestone, are transitional and contain particularly high carbonate concentrations compared with the overlying younger strata (see Figure 3.11), which contain greater proportions of clastic derived minerals. This change was caused by a profound shift in sediment supply, with *in-situ* materials derived from carbonate production being gradually replaced by silt-size reworked carbonate debris in addition to weathering-derived clastic detritus. This change was likely caused by flooding of the St. Lawrence Platform and subsequent infilling of the available accommodation (Note, the silt-size carbonate fraction in the Utica has an uncertain origin, but is likely comminuted bioclastic debris). The fact that production derived components represent most of the sediment present in the lower parts of the succession suggests reduced inputs of clastic detritus, and minimal clastic dilution, were occurring at this time (Aplin and Macquaker, 2011).

The Winterhouse Formation contains a stacked combination of carbonate-rich mudstone and sandstones. The units with the largest grain sizes were found at the base of the formation, suggesting a gradational shift to more clastic derived material from

episodic high-energy inputs of weathered material to the basin. The gradational shift from the underlying Lourdes Limestone to the Winterhouse Formation likely resulted from an increase in clastic sediment supply to the basin during the overall flooding of the St. Lawrence Platform (Bergstrom et al., 1974). All facies of the Winterhouse Formation contain similar detrital mineralogies dominated by quartz, feldspars and chlorite. This would suggest that detrital inputs varied little throughout deposition of this succession, indicating no significant shifts in provenance or climate.

In the Utica certain finely laminated, fine-grained units contain a pelted fabric and lack bioturbation. Preserved fecal pellets in these units suggest three important features of the water column at the time of deposition.

- The abundance and relatively large size ($> 750 \mu\text{m}$) of some of the fecal pellets suggest that the zooplankton had relatively high production rates and high concentrations of food (Butler and Dam, 1994; Dagg and Walser, 1986)
- The pellets likely contributed to a large part of the vertical flux of organic carbon to the sediment during this time period, as larger fecal pellets sink at greater velocity and can account for greater rates of fecal pellet preservation (Turner, 2002; Urban-Rich, 2001; Yoon et al., 1996).
- The fact that such an abundance of fecal pellets were preserved indicates that were not disrupted by bioturbation, which implies either fast burial rates or anoxic bottom waters (Macquaker et al., 2010b).

These features, coupled with the lack of traction structures suggest the sediment in the pelleted units was likely deposited from suspension settling (e.g. Figure 3.3, Figure

3.6). The pelleted fabric also has important implications for organic carbon preservation and this will be discussed further in subsequent sections on carbon cycling.

Not all the sediment in the Utica and the Winterhouse was deposited in such a low energy environment, as both formations clearly contain evidence of higher energy conditions. The presence of sharp-based normally graded silt to fine-sand beds in both facies suggests higher energy depositional events. Such event beds are characteristic of mud tempestites which contain an erosive surface below a mm-thin laminated silt to fine-sand sized section of reworked shell debris (Aigner and Reineck, 1982). The presence of these fabrics are indicative of storm events occurring in the basin (Aigner and Reineck, 1982). In the Winterhouse there is an overall upward coarsening succession that appears approximately 4 m above the base of the Formation. This pattern likely records a series of depositional events, which included both a high energy component (i.e. result of storms) in the coarse grained fraction followed by periods of waning sediment supply with lower energy, during which the more fine-grained clay-rich sections were deposited. Upward coarsening successions have been identified as representing shallowing deposits (De Raaf et al., 1977). Therefore, it appears the measured section records an interval of deepening from the base to approximately the middle (~ 4 m) followed by shallowing from 4 m to the top.

In the younger measured section of the Utica, undetectable at hand-specimen scale, small (< 2 mm) on-lap surfaces were identified infilling scour features (e.g. Figure 3.6). In these units horizontal lamina progressively terminate against the underlying topography. These structures indicate that at the time of deposition there was significant erosion and sediment was being transported through an advective process. Moreover, the

fact that they are stacked on top of each other, with little evidence of colonization, suggests that the recurrence frequency of sediment delivery events was high.

Organisms living at the sediment water interface colonized the top layers of the sediment in both formations. Many of the individual beds in both the Utica and Winterhouse have been homogenized by bioturbation, leaving only cryptobioturbation in the rock record (Pemberton et al., 2008). The Winterhouse contains a variety of bioturbation intensities and styles including *Planolites isp.*, *Thalassinodes isp.*, *Macaronichmus isp.*, *Rhizocorallium isp.* and *Paleophycus isp.* among others. In the Utica much less variety of ichnogenera was identified, with only *Thalassinoides isp.* and *Planolites isp.* being recorded in the measured intervals. The assemblages of bioturbation ichnogenera identified commonly occur on shelves in foreland basins with oxic to dysoxic water column conditions (Gingras et al., 2002; Levin et al., 2003; Macquaker et al., 2007; McIlroy, 2004; Pemberton et al., 2002). The degree of bioturbation preserved in mudstones is controlled by sediment accumulation rates, the frequency of delivery events (e.g. storms), substrate composition, and by geochemical (redox) conditions at the time of deposition (Aplin and Macquaker, 2011; Bentley et al., 2006; Jaeger and Nittrouer, 2006).

3.6.2. Diagenesis

Both successions contain abundant carbonate (with many units containing > 50% calcite) (Table 3.1, Table 3.2, Table 3.3). Petrographic analysis reveals that this carbonate was present in a number of components including fossil debris (e.g. echinoderms) as well as both pre- and post-compaction cements. The early precipitation of carbonate cement is linked to decreased recurrence frequency of sediment delivery events and breaks in

sediment accumulation (Raiswell and Fisher, 2000). The increased time available at these levels allowed for both the transport of solutes to sites of precipitation and the time necessary for precipitation to occur. (Aplin and Macquaker, 2011; Morse et al., 2007).

The extent and texture of carbonate precipitation depended largely on the length of these low sediment delivery intervals (Demico and Hardie, 2002). During relatively short intervals the restriction of sediment supply resulted in the precipitation of small (5 to 10 mm diameter) carbonate nodules (e.g. Figure 3.6, Figure 3.8). In units with a much more pervasive carbonate cement, production from the water column exerts a significant control over mudstone composition. In these intervals, only a small amount of detrital material was brought to the basin and held together in a card house fabric with a large amount of porosity prior to compaction (Aplin and Macquaker, 2011). Organisms with carbonate shells (e.g. echinoderms, bivalves, bryozoans, etc.) were deposited on the surface of the sediment. After accumulation, the Ca-rich shells dissolved leaving the relatively large pore spaces filled with Ca^{2+} and dissolved inorganic carbon (e.g. HCO_3^-) rich waters, which began to precipitate in the form of calcium carbonate (e.g. Figure 3.7, Figure 3.13, Figure 3.14) (Morse et al., 2007).

The form of carbonate cement precipitating during these intervals reflects redox conditions of the pore waters at the time of deposition. Non-ferroan calcite, which is the most common cement in both formations, likely, reflects oxygen-rich intervals (Aplin and Macquaker, 2011; Mächent et al., 2007; Morse et al., 2007). Dolomite-rich units reflect sulfate reduction zones, particularly when also associated with pyrite (e.g. Figure 3.4 C-D, Figure 3.6 F). The presence of reduced sulfide species limits the poisoning effect of sulfate that otherwise inhibits dolomite precipitation (Baker and Kastner, 1981;

Curtis et al., 1986; Warren, 2000). The precipitation of pyrite is related to sulfide produced from sulfate reduction during the breakdown of organic matter, reacting with available iron under reducing conditions in the sediment (Berner, 1984; Canfield, 2001; Rickard and Luther, 2007). A variety of sizes and textures of pyrite were observed in both formations (e.g. Figure 3.5 F, Figure 3.6 F, Figure 3.13 D, Figure 3.15 E). Pore water concentrations of iron, and the amount of time allowed for precipitation, controlled the size and texture (euhedral or framboidal) of pyrite being precipitated (Macquaker et al., 1997).

Dissolution of potassium feldspar grains was observed in both the Utica and Winterhouse Formations, but more extensively in the Winterhouse. In the areas of K-feldspar dissolution, diagenetic quartz (e.g. Figure 3.12 D) and/or a combination of illite and chlorite (e.g. Figure 3.13 E-F) were detected. The assemblage of illite, quartz and chlorite may be from an illitization process during which mixed layer illite/smectite was converted to illite (Eberl and Hower, 1976; Elliott and Matisoff, 1996; Essene and Peacor, 1995; Freed and Peacor, 1989; Nadeau et al., 1984; Velde and Vasseur, 1992). A generalized reaction for this process is given below in reaction 4 (Aplin and Macquaker, 2011).



This reaction typically occurs during late stage diagenesis once the sediment reaches temperatures above approximately 70°C (Hower et al., 1976). It is commonly noted that dissolving K-feldspars are the source of potassium for illite formation (Hower et al., 1976). Therefore, this reaction would explain both the partial or complete potassium feldspar grain dissolution observed, and the presence of diagenetic quartz (e.g.

Figure 3.12 D-F), illite and chlorite (Figure 3.13 E-F) (Berger et al., 1999; Hower et al., 1976). This suggests that late stage diagenesis has potentially significantly overprinted the present day mineralogy in the Winterhouse and to a much lesser extent the Utica as well. Not all quartz, chlorite and illite appear to be a result of this reaction, as in some samples the grain boundaries and surrounding carbonate cement suggests these minerals have a detrital origin (e.g. Figure 3.14 F).

3.6.3. Carbon cycling in Ordovician mudstones (sequestration vs. mineralization)

The Utica and the Winterhouse Formations are fine-grained units of approximately similar age (i.e. Mid- to Late-Ordovician). However, total organic carbon concentrations are quite different between the two formations. The Utica contained TOC of up to 1.75 % while in the extensively calcite-cemented Winterhouse Formation; the highest TOC concentration was 0.31 %. Porosity within the basins was also quite different. Throughout the Winterhouse Formation, grain dissolution porosity is observed, however the porosity that was created has been in-filled with calcite cement. In comparison, grain dissolution in the Utica Formation was much less extensive. Where it has occurred it to has been in filled primarily with carbonate cement. However in this case some of the carbonate precipitated as dolomite, which preserved small but potentially significant volumes of porosity between the host material and the cement itself.

The multi-technique analysis used (XRD, TOC, optical and SEM petrography) revealed that both formations appear to contain similar concentrations of carbon during their initial deposition. The difference between the two formations arises from the quantity of mineralized carbon vs. the quantity sequestered as organic carbon. In the

Winterhouse Formation, pH and redox conditions at the time of deposition favoured carbon being present in an oxidized form (CO_2 , HCO_3^- , H_2CO_3^*). In this form, carbonate in the pore waters reacted with available cations (Ca^{2+} , Mg^{2+}) to precipitate as authigenic carbonate predominantly in the form of calcite (e.g. reaction 5) and rarely dolomite (e.g. reaction 6) (Warren, 2000).



The net effect of this process in the Winterhouse formation was a decrease in organic matter concentrations, and increased carbonate cement production - subsequently decreasing the overall porosity.

Carbonate in the Utica formation is predominantly in the form of fine-grained (clay-sized) reworked skeletal debris. While the exact hydrodynamic mechanism for transport of this fine-grained material cannot be constrained in this study, the fact that it was transported is significant. Due to the high surface areas of the fine-grained material the capacity for retaining highly reactive organic carbon is increased because of the greater number of binding sites (Kennedy et al., 2002). There is also more evidence of increased productivity in the Utica due to the abundance of relatively large fecal pellets, which can help to transport and preserve organic matter (Turner, 2002). These factors lead to an increase in the preservation of organic carbon during deposition and subsequent burial.

Bohacs et al. (2005) argued that moderate sedimentation and production rates are ideal for the preservation of organic matter rich units because they i) provide optimal conditions for organic matter content relative to dilution by biosilica, ii) provide optimal

conditions for burial preservation relative to dilution by terrigenous detritus, and iii) facilitate redox conditions that are consistently favourable for preservation. In environments where calcium-bearing organisms are more extensive than silicon-bearing organisms the optimal conditions for organic-rich rock preservation are very similar.

In carbonate-rich mudstones dilution is a key factor when attempting to identify organic-rich units, just as it is in silica-rich marine mudstones (Bohacs et al., 2005). In carbonates however, it is also of primary importance to understand the composition of the diluting fraction, i.e. whether it is composed of detrital minerals or reworked skeletal debris.

During periods of low sedimentation rates and low production, calcium in the bottom waters can remain undersaturated leading to the concentration of detrital clay and potentially organic matter (Bohacs et al., 2005; Isaacs, 1985). If the sediment transport follows a pathway with re-worked skeletal debris (e.g. a recently deposited carbonate platform or reef up-dip) a source of re-worked clay to silt sized carbonate can be transported along with the detrital fraction - leading to increased carbonate concentrations. If the early geochemical conditions of the bottom waters are conducive to carbonate dissolution this can lead to the eventual precipitation of carbonate cement in the pore waters of the sediment. This can also occur if the silt to clay sized carbonates experience dissolution and reprecipitation as carbonate cement during later stage diagenesis. The net effect of this process would be the destruction of porosity and degradation in quality of the unit as a reservoir. However the carbonate cement may increase the overall fracturability of the rock (Rijken and Cooke, 2001). The Winterhouse Formation largely reflects this scenario.

Areas with elevated sedimentation rates and biogenic production can lead to excess calcium saturation in the bottom waters, with consequent preservation of calcium-rich tests (Bohacs et al., 2005). If clay to silt-sized carbonate material were transported to the basin it would also be preserved, rather than experiencing dissolution. Due to the high Ca^{2+} in the pore waters calcium cement would form in the pore spaces in this scenario, once again reducing the porosity and the rock's quality as a reservoir.

Moderate sedimentation and production rates would likely provide the best preservation potential for an organic-rich rock. Dissolved concentrations of calcium would stay near but below saturation. Therefore, as clay to silt-sized carbonate material was transported to the basin it would primarily be preserved in the sediment. This would be aided if organic matter was transported to the sediment in a more resistant form (i.e. marine snow or pellets) (Macquaker et al., 2010b). The net effect of these conditions would be a greater preservation of carbon as organic carbon and greater relative porosity, thus creating an ideal reservoir or source rock. The Utica Formation largely reflects this scenario.

Mudstone successions with elevated calcium concentrations may have been more common in rocks prior to the evolution of diatoms in the Triassic period (Sims et al., 2006). While radiolaria can contribute significant amounts of silica to ocean bottom waters, the evolution of diatoms, combined with their ability to thrive in a wide variety of environments, resulted in the depletion of silica concentrations in ocean waters to the low modern day concentrations (less than 5 mgL^{-1}) (Tréguer et al., 1995).

Elevated carbonate concentrations are not uncommon in mudstone successions, several of which have been identified as useful shale gas reservoirs. This investigation

highlights the need for petrographic techniques in combination with an array of other analyses to accurately assess the form in which carbonate occurs. Without detailed petrographic analysis carbonate contents in the two units would have been perceived (e.g. through XRD alone) to be very similar.

3.7. CONCLUSIONS

In the Winterhouse, pH and redox conditions at the time of deposition favoured microbially mediated carbonate precipitation. Mineralization decreased organic carbon contents and porosity, reducing the amount of potential gas generation. In contrast, the Utica, which contains similar bulk quantities of carbonate, retained a greater amount of both porosity and organic carbon due to the fact that carbonate is dominantly in the form of fine-grained reworked skeletal debris. The lack of an extensive carbonate cement resulted in a greater proportion of the organic carbon fraction being preserved in the Utica Shale.

In the middle section of the Utica Formation, the proportions of clastic derived material are higher. Here the individual units are mostly composed of normally graded pellet-bearing carbonate mudstones. Similar to the lower section, variations in facies are a result of either i) restrictions of clastic sediment supply or ii) increases in hydrodynamic energy. These two factors allowed for increased colonization of the sediment.

The variation in the sediment delivery rates appears to be the primary control on facies shifts in both formations; from the more clay rich to the more calcite-cement dominated units. In some intervals in the Winterhouse Formation sediment was cemented at the sea floor as evidenced by the presence of boring into a hard ground surface (Figure 3.13 B). In the Winterhouse the substrate composition remained very consistent through

the measured succession, with the amount of carbonate cement being the only major shift in the mineralogy.

This investigation highlights the need for petrographic techniques in combination with an array of other analyses to accurately assess the form in which carbonate occurs. Identifying not only the bulk concentration of carbonate (e.g. with X-Ray Diffraction) but the form present (e.g. through petrographic investigation) is key to understanding factors that affect the reservoir characteristics.

The carbon cycle is of unique and vital importance to defining the large degree of heterogeneity recently recognized in fine-grained successions (Macquaker and Bohacs, 2007; Schieber et al., 2007). The balance between the inorganic and organic spheres of carbon is particularly significant for shales as only the presence of carbonate as cement aids fracturability of a reservoir rock. In contrast, rocks that contain fine-grained re-worked carbonate skeletal material may potentially retain a greater amount of porosity/permeability and organic matter, thus increasing overall reservoir quality.

Table 3.2: Analytical results of Utica site UCB

LOC	Sample Size #											
	UCB	0	UCB 07	UCB 075	UCB 1.40	UCB 2.00	UCB 3.25	UCB 5.00	UCB 7.50	UCB 10.00	UCB 15.00	
Major Elements		1.31	1.15	1.36	1.43	1.25	1.05	1.42	1.38	1.62	1.38	1.64
Trace Elements												
Major Elements												
SiO ₂	wt%	0.4	0.4	0.4	0.4	0.3	0.4	0.4	0.4	0.4	0.4	0.4
Al ₂ O ₃	wt%	0.0	0.1	0.1	0.1	0.0	0.0	0.0	0.0	0.0	0.0	0.1
Fe ₂ O ₃	wt%	0.0	0.0	0.0	0.0	0.0	0.0	0.0	0.0	0.0	0.0	0.0
MgO	wt%	0.0	0.0	0.0	0.0	0.0	0.0	0.0	0.0	0.0	0.0	0.0
CaO	wt%	0.4	0.4	0.4	0.4	0.4	0.4	0.4	0.4	0.4	0.4	0.4
Na ₂ O	wt%	0.0	0.0	0.0	0.0	0.0	0.0	0.0	0.0	0.0	0.0	0.0
K ₂ O	wt%	0.0	0.0	0.0	0.0	0.0	0.0	0.0	0.0	0.0	0.0	0.0
P ₂ O ₅	wt%	0.0	0.0	0.0	0.0	0.0	0.0	0.0	0.0	0.0	0.0	0.0
Trace Elements												
Cl	ppm	625.4	6969.3	6179.4	5904.8	6366.5	6304.8	6304.8	6304.8	6304.8	6304.8	6304.8
Sc	ppm	66.7	69.7	57.8	100.1	114.5	100.1	114.5	100.1	114.5	100.1	114.5
Y	ppm	16.4	33.0	30.1	32.7	16.4	32.7	16.4	32.7	16.4	32.7	16.4
Zr	ppm	36.5	37.3	41.3	29.7	46.0	37.3	46.0	37.3	46.0	37.3	46.0
Nb	ppm	21.0	22.2	23.2	15.9	23.1	15.9	23.1	15.9	23.1	15.9	23.1
Sn	ppm	8.5	10.4	10.4	5.2	10.4	10.4	10.4	10.4	10.4	10.4	10.4
Ce	ppm	-1.0	-1.0	4.4	-1.0	6.5	6.5	6.5	6.5	6.5	6.5	6.5
Pr	ppm	19.4	-1.0	-1.0	-1.0	-1.0	-1.0	-1.0	-1.0	-1.0	-1.0	-1.0
Sm	ppm	165.0	165.0	165.0	165.0	165.0	165.0	165.0	165.0	165.0	165.0	165.0
Y	ppm	13.3	14.6	14.6	12.6	14.7	12.6	14.7	12.6	14.7	12.6	14.7
Zr	ppm	61.7	61.7	61.7	61.7	61.7	61.7	61.7	61.7	61.7	61.7	61.7
Nb	ppm	6.1	7.0	6.9	5.0	7.0	6.9	7.0	6.9	7.0	6.9	7.0
Mo	ppm	787.9	784.5	834.4	621.5	862.8	621.5	862.8	621.5	862.8	621.5	862.8
Co	ppm	-1.0	-1.0	-1.0	-1.0	-1.0	-1.0	-1.0	-1.0	-1.0	-1.0	-1.0
Ni	ppm	5.6	-1.0	-1.0	-1.0	-1.0	-1.0	-1.0	-1.0	-1.0	-1.0	-1.0
Th	ppm	-1.0	-1.0	-1.0	-1.0	-1.0	-1.0	-1.0	-1.0	-1.0	-1.0	-1.0
U	ppm	-1.0	-1.0	-1.0	-1.0	-1.0	-1.0	-1.0	-1.0	-1.0	-1.0	-1.0

3.9. FIGURES

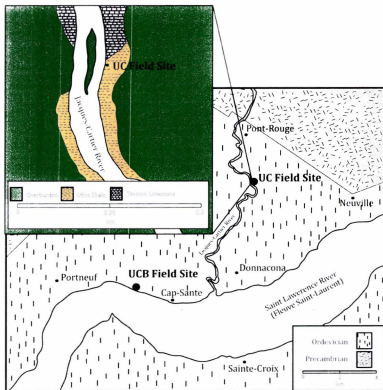


Figure 3.1: Map of the field locations of the Utica Shale and surrounding regional geology in the St. Lawrence Lowlands of Quebec. (Modified from (Belt et al., 1979).

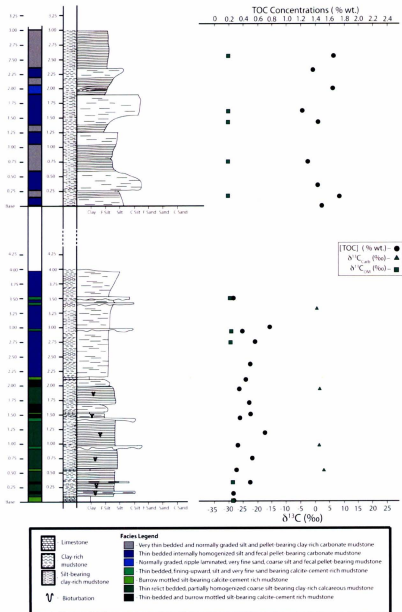


Figure 3.2: Stratigraphic log of the two measured sections of the Utica Shale

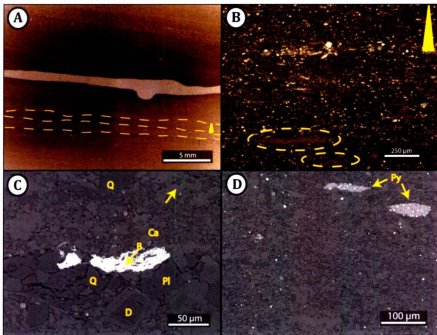


Figure 3.3: Petrographic observations of the normally graded, very thin bedded, pelleted, silt-bearing, clay-rich carbonate mudstone (U1). (A) Scan of thin section showing thin bedding planes and fining upward sequences. Solid triangles demonstrate a fining upward sequence. (B) Optical image from petrographic microscope. Circle with dashed lines are compacted pellets. (C and D) Backscatter electron optical micrographs. Mineralogy is arrowed and labeled as; Q – quartz, Ca – calcite, D – dolomite, Pl – plagioclase, Py – Pyrite, and B – Barite.

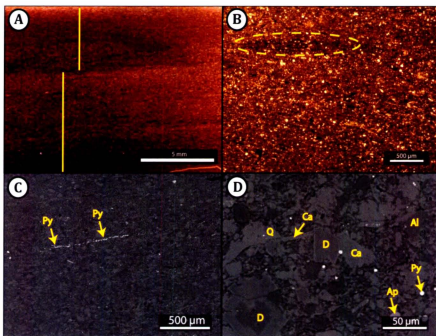


Figure 3.4: Petrographic observations of thin-bedded partly homogenized, silt- clay- and carbonate cement-bearing mudstone (U2). (A) Scan of thin section showing internally homogenized beds. (B) Optical image from petrographic microscope. Circled with dashed lines are compacted pellets. (C and D) Backscatter electron optical micrographs. Mineralogy is arrowed and labeled as; Q – quartz, Ca – calcite, D – dolomite, Al – albite, Py – Pyrite, and Ap – Apatite.

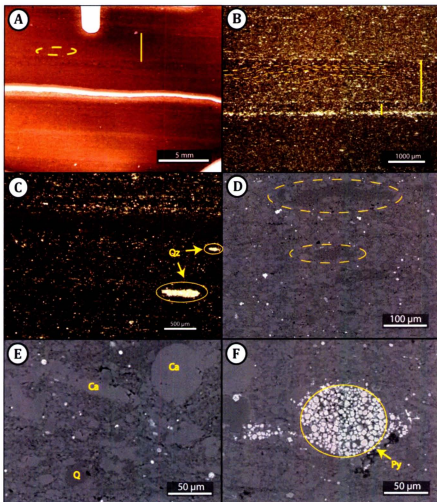


Figure 3.5: Petrographic observations of normally graded, ripple laminated, very fine sand, coarse silt and fecal-pellet bearing carbonate mudstone (U3) (A) Scan of thin section showing normally grading beds, one of which is highlighted with a solid bar. (B) Optical image from petrographic microscope. Down-lapping surfaces are identified with dashed lines. Circled with dashed lines are crushed pellets in the fabric of this facies. Circled with solid lines are nodules, which have been filled with either quartz or pyrite. (C to F) Backscatter electron optical micrographs. Mineralogy is arrowed and labeled as; Q – quartz, Ca – calcite, and Py – pyrite.



Figure 2.6: Petrographic observations of thin-bedded, normally graded, silty and very fine sand-bearing calcite-cemented mudstones (U4). (A and B) Sower of thin sections showing event beds with sharp and unreset erosional surfaces. (C and D) Optical images from petrographic microscopes. Highlighted in (C) and (D) are the two surfaces of individual beds (G) more coarse silt to sand sizes (H) more silt, clay size. (E and F) Backscattered electron optical micrographs. Mineralogy is unreset and related to Ca - calcite, D - Dolomite and Py - pyrite.

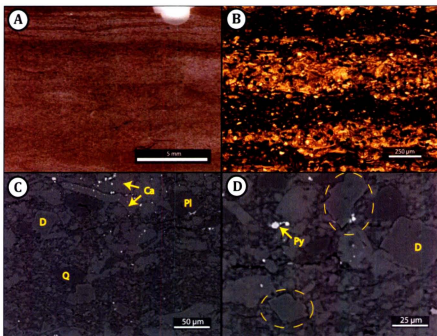


Figure 3.8: Petrographic observations of thin, relict bedded, partially homogenized coarse silt-bearing, clay-rich calcareous mudstone (U6). (A) Scan of thin section showing disrupted bedding planes. (B) Optical image from petrographic microscope. (C to F) Backscatter electron optical micrographs. Circled with dashed lines are dolomite grains with visible porosity around them. Mineralogy is arrowed and labeled as; Q – quartz, Ca – calcite, D – dolomite, Pl – plagioclase, and Py – Pyrite.

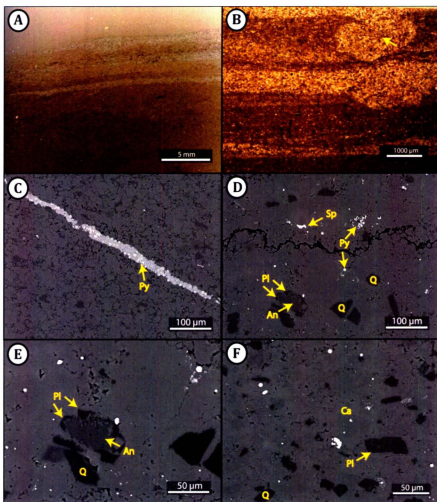


Figure 3.9: Petrographic observations of thin-bedded and burrow mottled fine silt-bearing, calcite cement-rich mudstone (U7). (A) Scan of thin section showing disrupted bedding planes. (B) Optical image from petrographic microscope showing bioturbation. (C to F) Backscatter electron optical micrographs demonstrating feldspar dissolution. Mineralogy is arrowed and labeled as; Q – quartz, Ca – calcite, D – dolomite, Pl – plagioclase, An – anorthite and Py – Pyrite

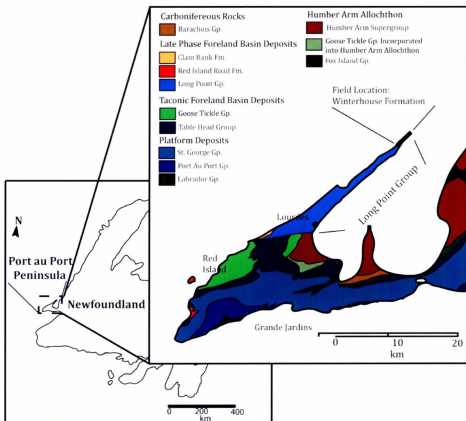


Figure 3.10: Map of the field location and regional geology surrounding the Winterhouse Formation, which is part of the Long Point Group, on the Port Au Port Peninsula of Newfoundland. (Modified from (Williams, 2000).

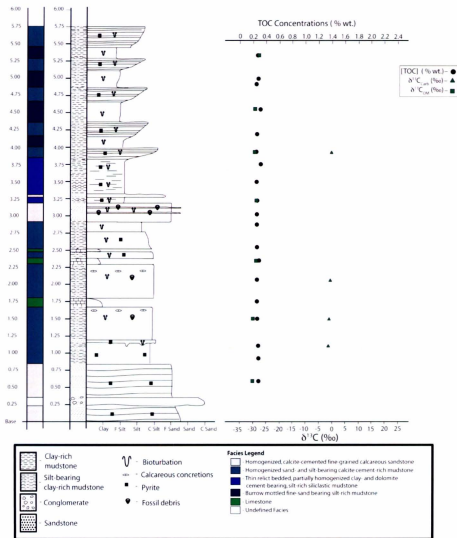


Figure 3.11: Stratigraphic log of the measured section of the Winterhouse Formation.

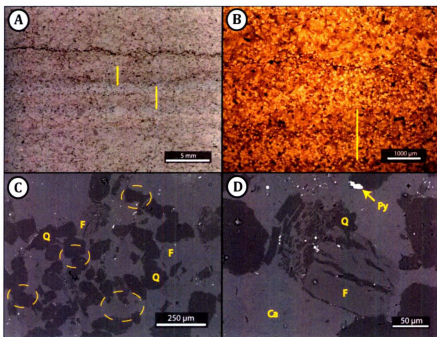


Figure 3.12: Petrographic observations of homogenized, calcite-cemented fine-grained calcareous sandstone (W1). (A) Scan of thin section showing thin bedding planes and fining upward sequences. Solid lines demonstrate the preserved laminations. (B) Optical image from petrographic microscope. (C and D) Backscatter electron optical micrographs. Circled with dashed lines are concavo-convex quartz grain contacts, which indicate that grain dissolution porosity, occurred post-compaction. Mineralogy is arrowed and labeled as; Q – quartz, Ca – calcite, F- K-Feldspar, and Py – Pyrite.

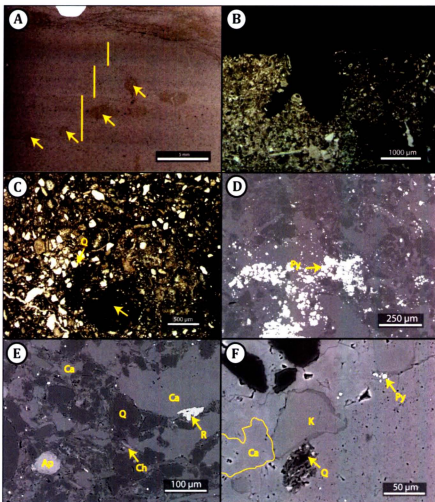


Figure 3.13: Petrographic observations of homogenized sand- and silt-bearing calcite cement-rich mudstone (W2) Scan of thin section demonstrating homogenized and bioturbated nature of individual beds. Planolites *isp.* burrows are arrowed. (B and C) Optical images from petrographic microscope. (B) has a bored surface indicating that this facies solidified before the next was colonized and subsequently cement. (D – E) Backscatter electron optical micrographs. Mineralogy is arrowed and labeled as; Q – quartz and Ca – calcite, K – k-feldspar, Ap – apatite, R – rutile and Py – pyrite.

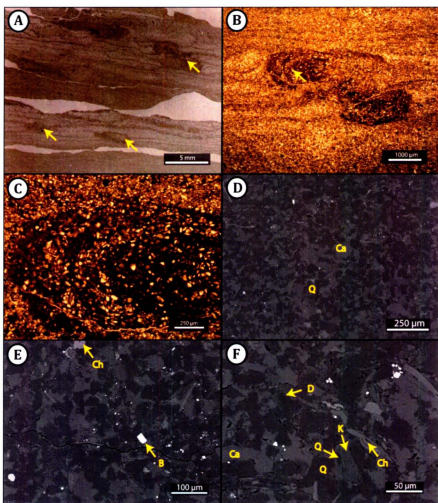


Figure 3.14: Petrographic observations of thin relict bedded, partially homogenized clay- and dolomite cement-bearing, silt-rich siliclastic mudstone (W3). (A) Scan of thin section with arrows pointing to the burrows interpreted to be of *Rhizoacarrallium*. (B and C) Optical images from petrographic microscope. (D to F) Backscatter electron optical micrographs. Can see there is an abundance of detrital grains, which have been cemented together by calcite and quartz. Mineralogy is arrowed and labeled as; Q – quartz, Ca – calcite, D – dolomite, B – barite, K – K-Feldspar, Ch – chlorite and Py – pyrite.

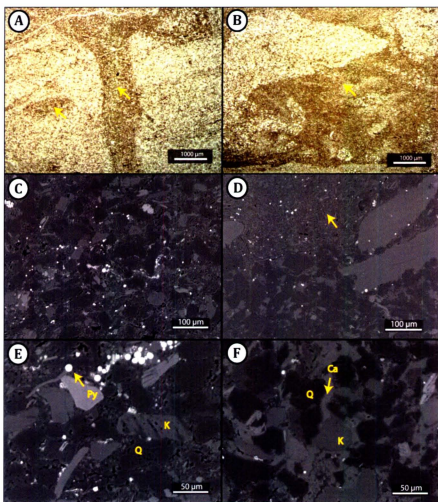


Figure 3.15: Petrographic observations of burrow mottled fine-sand bearing silt-rich mudstone (W4) (A and B) Optical images from petrographic microscope. Water escape structures and that bioturbation have left little of primary depositional structures. (D to F) Backscatter electron optical micrographs. (D) shows the boundary between the inside and outside of a burrow, with the burrow containing much more fine-grained material. The partial dissolution of a K-feldspar grain to quartz can be seen in (E). Calcite cement filling in the boundaries between individual pores can be seen in (F). Mineralogy is arrowed and labeled as; Q – quartz, Ca – calcite, K – K-Feldspar, and Py – pyrite.

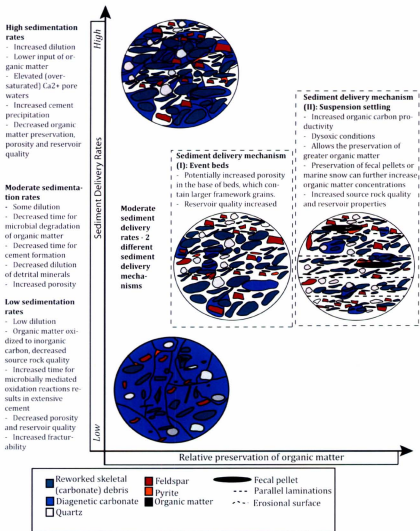


Figure 3.16: Figure demonstrating the link between sediment delivery rates, extent of cement and organic carbon preserved in carbonate-rich mudstone units. These parameters exert key controls on the source vs. reservoir potential of unconventional hydrocarbon reservoirs. (Information for figure (Bohacs et al., 2005; Butler and Dam, 1994; Sageman et al., 2003).

4. : MICROLITHOFACIES ANALYSIS TO INVESTIGATE THE SCALE OF VARIABILITY IN FINE-GRAINED MUDSTONES: USING THE BENBULBEN SHALE OF SLIGO CO. IRELAND

4.1. INTRODUCTION

The presence of liquid and gaseous hydrocarbons preserved in fine grained sediments has become of great interest as an energy resource over the last few years, due to the fact that vast reserves are likely present in fine-grained organic carbon-rich rocks i.e. shale gas reservoirs (Mango and Jarvic, 2009). The controls on shale gas reservoir quality are subtle and rely on these materials being carbon rich, to generate and store the gas, and cemented with either silica or carbonate cement so that they are more likely to artificial hydrofracture and develop connected porosity/permeability (Rijken and Cooke, 2001). In hand specimens It is widely assumed that mudstones are largely homogenous, however, recent research has demonstrated this assumption is incorrect (Ross and Bustin, 2009; Schieber et al., 2007). Research has demonstrated that mudstones actually contain significant heterogeneity in grain size, mineralogy, rock fabric, and the proportion of materials derived from production, detrital and diagenetic inputs (Aplin and Macquaker, 2011; Baas et al., 2009; Macquaker et al., 2010a; Macquaker and Bohacs, 2007; Macquaker and Gawthorpe, 1993; Schieber, 2009; Schieber et al., 2010; Van Cappellen, 2003). This heterogeneity is significant because it results in localized “economic sweet spots” being present within larger shale gas targets. Due to the fine-grained nature of these rocks this variability is often only visible at sub-hand specimen scales thus techniques capable of resolving high-resolution variability need to be utilized. Geological models from sedimentological and geochemical data can predict sediment origins,

sediment dispersal mechanisms and post-depositional processes can be used to predict the spatial temporal locations of the best reservoirs.

Identifying the scale of heterogeneity in mudstones can be very difficult due to their very fine-grained nature. Data in regards to mineralogical or elemental composition can be misleading when not coupled with petrographic analysis that indicate the origin of the minerals and elements. Elevated carbonate concentrations for example can be a good indicator of a unit in a formation that will be likely to hydrofracture (Rijken and Cooke, 2001). However, this is only if the carbonate is present as a diagenetic cement, whereas if it occurs as a result of a significant production component with little cement it may act as a baffle to the units ability to hydrofracture. Therefore it is necessary to utilize a wide variety of techniques to identify the spatial and temporal location of the best reservoir and source rocks in a formation.

The aim of this study is to investigate the scale of the spatial heterogeneity in fine-grained mudstones, specifically to identify and characterize the inputs to mudstones (i.e. detrital, production and diagenetic) and how these components vary on a range of scales. With these data and number of key parameters can be observed including: the controls on the distribution of carbonate minerals; and the type of carbon preservation (oxidized or reduced). Understanding these parameters make it possible to identify how carbon cycling might influence the rocks source and reservoir potential.

To investigate these features this study will use the remarkably well-exposed Carboniferous (Brigantian) mudstone succession at Streedagh Point in Sligo County, Ireland. Heterogeneity within the mineralogical, sedimentological and geochemical characteristics of this unit will be analyzed on a range of scales from macroscopic (field)

to microscopic to determine how lithofacies variability present might influence overall rock forming processes. These features will be tested with variety of optical, electron optical and geochemical techniques to identify the heterogeneity across spatial and temporal scales. In addition variations in elemental composition will be measured using both conventional XRF techniques and an ITRAX Core scanner. This will allow for a comparison between bulk analysis which has a resolution of >50 mm to a technique with a resolution of 2 mm (Core scanner). These data are important as they provide information about the rocks petrophysical properties, particularly its susceptibility to hydrofracturing. Moreover, the data gathered here at different scales should enable insights to be gained into the subtle shifts in the mineralogy that are likely to be responsible for varying rock rheological properties at different scales.

4.2. MATERIALS AND METHODOLOGY

Samples were collected from outcrop of the Benbulbin Shale on Streedagh Point in Sligo Co. of Northwest Ireland (Figure 4.1). A detailed log was recorded of the field scale facies variability. A total of 21 samples were collected across a 6 m vertical section beginning at the base of the formation (field location in Figure 4.1).

Unusually thin (20-25 μm), thin sections were prepared from each sample. These sections were initially described through the use on an optical petrographic microscope (Nikon Eclipse-Pol). Following this the sections were coated with carbon and analyzed both texturally and compositionally using an FEI Quanta 400 environmental scanning electron microscope (SEM) equipped with an electron backscattered (BSE) and energy dispersive X-ray (EDS) detectors. The SEM was operated at 25 kV and 2.0 μA ; with a

working distance of 12 mm. This procedure follows a similar workflow as used in earlier studies (e.g. Macquaker and Gawthorpe, 1993).

For bulk quantitative analyses, 18 mudstone samples were crushed in a tungsten carbide grinding mill. To minimize cross-sample contamination in the mill, ultra-pure silica was crushed between each sample and all tools and surfaces were thoroughly cleaned with ethanol. The mineralogical composition of each sample was determined using a Rigaku Ultima IV X-ray Diffractometer (XRD) with a copper K α X-ray source equipped with a scintillation counter detector. Total organic carbon analysis was conducted at the Manchester Metropolitan University (MMU) in a Leco Induction Furnace. In this technique total carbon contents of each sample were initially determined. The samples were then decalcified using warm 2% HCl, and the decalcified carbon contents were determined using the same Leco furnace. The TOC contents of each sample were then determined by difference. A sub-set of X samples was selected to be analyzed for $\delta^{13}\text{C}$ and $\delta^{18}\text{O}$ isotopic analysis and was conducted by the Environmental Isotope Laboratory in the Earth and Environmental Science Department at Waterloo University.

Conventional X-ray fluorescence (XRF) spectrometry was utilized to determine concentration of major and trace elements. For these analyses 5 mg of sample was weighed and mixed with a 0.7 gm of phenolic resin binder. After mixing, this powder was placed in a Herzog Pellet Press and pressed for 10 seconds at 20 ton/in² pressure. The pellet was then baked at 200°C for 15 minutes. The operating conditions of the XRF are described in Longerich (1995). In addition, to conventional XRF analysis the samples were scanned using an ITRAX Core scanner. Prior to scanning the samples on the

ITRAX scanner, each sample was prepared by manufacturing blocks with a width of 70 mm, depth of 20 mm, variable lengths and preparing a polished surface. This scanner creates a high-resolution image and a X-Radiograph image of each of the polished samples, and provides X-ray Fluorescence data at 2 mm intervals across each of the samples.

Lithofacies present will be classified using the nomenclature scheme proposed by Macquaker and Adams (Macquaker and Adams, 2003; Ross and Bustin, 2009) for mudstones (sedimentary rock composed of > 50% grains < 0.063 mm). Thus lithofacies names will be based on the percentage abundance of materials of either different grain size or origin within a mudstone and microfabrics visible. For example mudstone beds containing >90% of a particular grain size are described as being “dominated” by that component; units that contain between 50 to 90% of a particular grain size are described as being “rich” in that component; whereas materials that comprise 10 to 50% of a particular grain size are described as “bearing” the component. With modifiers (e.g. thin bedded, laminated, burrowed, homogenized, fossiliferous) being prefixed to the beginning of the name to describe its textural attributes and its compositional attributes (e.g. siliceous, calcareous, dolomitic, siliclastic) being suffixed to the end of the name.

4.3. GEOLOGICAL HISTORY

The Benbulbin Shale Formation was deposited close to the Devonian-Carboniferous boundary. During this time North-Western Ireland was paleogeographically located just south of the late Mississippian paleoequator (Aretz, 2010). During the Mississippian the region which is currently North-Western Ireland was part of the larger Northwest European carbonate platform and experienced repeated

cycles of carbonate dominated and siliciclastic-dominated sediment delivery to the area (Aretz, 2010). The cycles were a result of regional tectonic activity and sea-level oscillations, particularly during the late Viséan (George, 1958; Graham, 1996; Mitchell, 2004)

The Benbulbin shale itself was deposited in an embayment of the much larger Northwest-European carbonate platform during the Tournaisian–Viséan age (George, 1958; Graham, 1996; Mitchell, 2004; Sevastopulo, 2009). The mudstones in the Benbulbin Shale are thought to be the result of intrabasinal rise due to regional tectonic activity (Somerville et al., 2009). This tectonic activity created a dam restricting influx of terrestrial sediment from the Laurasian continent. Specifically the rise of the Ox Mountains or from active faults such as the Grange Fault (e.g. Figure 4.1) likely created this dam (Somerville et al., 2009).

In the Sligo region underlying the Benbulbin shale is the more coarse-grained siliciclastic material of the Mullaghmore Sandstone Formation. Overlying the Benbulbin Shale is the Glencar Limestone Formation (Somerville et al., 2009).

4.4. RESULTS

A 6 m section of the Benbulbin Shale, which is exposed at Streedagh Point in County Sligo of Northwestern Ireland, was measured for this study (Figure 4.1). A total of 6 lithofacies were identified on the basis of differing grain size, mineralogy and textural attributes. The lithofacies present include both calcareous sandstones and calcareous mudstones. The individual units exhibit a variety of laminae geometries and are variably bioturbated. Detailed descriptions of each lithofacies are given below and

their stratigraphic distributions are shown in Figure 4.2. ITRAX scan results for each mudstone lithofacies are also presented in Figure 4.9.

4.4.1. Burrow mottled silt-bearing, clay-rich calcareous mudstone with broken skeletal debris

The most common facies in the measured section are burrow mottled silt-bearing clay-rich calcareous mudstones (Figure 4.3). These units contain abundant disarticulated skeletal debris (in the range of 10 to 400 μm), and rare relatively large fossil fragments (>1000 μm). The framework of these units is composed of a combination of the fossil debris (which is composed of calcite) and detrital quartz and feldspars grains, which range in size from <3 to 35 μm . Identifiable fossils preserved in the framework fraction include fenestrate bryozoans, echinoderm fragments (Figure 4.3 B), and crinoids spines (Figure 4.3 D).

The fabric of this facies has been intensely bioturbated. Burrowing has destroyed almost all-visible bedding. Trace fossils preserved in the fabric are commonly of the ichnogenus *Nereites isp.* with a clay-filled core and a halo composed of silt surrounding the core (Figure 4.3 A-B). There are also some trace fossils of *Phycosiphon isp.* and *Planolites isp.* in this facies (Figure 4.3 A-C).

Calcite also occurs as cement surrounding framework grains and filling in pore space (Figure 4.3 E-F). Albite occurs throughout, both in the clay size fraction within burrows and as silt-sized framework grains in the host sediment. The silt-sized albite grains exhibit both irregular and very sharp grain outlines (Figure 4.3 F). Pyrite occurs in minor amounts as a diagenetic mineral both in euhedral and framboidal forms (Figure 4.3 E-F). XRD analysis indicates the mineralogical composition of this facies is calcite

(65.5%), quartz (18.5 %), dolomite (8.7 %) illite (5.4 %), albite (4.5 %), and muscovite (0.78 %), pyrite (0.6 %) (Table 4.1). Total organic carbon of this facies was measured to be 0.57% and have a $\delta^{13}\text{C}_{\text{OM}}$ signature of -27.6 ‰ (Table 4.1). In bulk carbonate samples the $\delta^{13}\text{C}_{\text{calcite}}$ of was measured to be +3.1 ‰ and the $\delta^{18}\text{O}_{\text{calcite}}$ -5.4 ‰ (Table 4.1).

The ITRAX scanner identified a moderate response from both calcium and silicon (Si) (Figure 4.9). Overall the fabric of the rock contains the primarily clastic derived elements of Silicon (Si), and potassium (K), magnesium (Mg) and aluminium (Al) that were detected with variable (low to relatively high) responses. Calcium (Ca) is particularly concentrated in the haloes surrounding common *Nereites isp* burrows, and as silt-sized shell debris. Slightly elevated calcium concentrations are also visible at the base of individual beds where relict bedding planes are visible. Iron (Fe) and sulfur (S) responses were low in these samples likely due to the low overall pyrite concentrations.

4.4.2. Homogenized, burrow mottled silt-bearing carbonate-rich calcareous mudstone

Homogenous, burrow mottled silt-bearing carbonate-rich facies are highly bioturbated (e.g. *Planolites isp.*) and contain no evidence of depositional textures (Figure 4.4). In many of the samples silt-rich halos of the burrows overlap. This has resulted in the overall fabric of this facies being much more clay-poor, relative to other similar fabrics in the Benbulbin Shale.

The framework of this facies is composed of a mix of well-sorted skeletal carbonate debris and detrital minerals. The skeletal carbonate fraction, which makes up most of the framework material, has grain sizes ranging from 10 to 250 μm (Figure 4.4 B-C). Other framework grains include quartz and feldspars (plagioclase) ranging in size

from <3 to 50 μm (Figure 4.4 E-F). The detrital fraction, which makes up a small amount of the total rock, includes feldspar, quartz and minor amounts of clays. Minor amounts of dolomite are present although undetected through XRD analysis. It is present as corroded grains through SEM analysis. In many areas authigenic feldspar (albite) appears to occur as a rim around corroded dolomite grains. Many well-preserved feldspar (albite) and pyrite grains are similar in shape to the trigonal rhombohedral crystal structure, which is common for dolomite cements (Figure 4.4 D-F). The similar shape may suggest that pyrite and albite (at different stages of diagenesis) may be occurring as a pseudomorphic replacement of dolomite. Minor amounts of silica cements are also present. This quartz replaces pre-existing corroded calcite cements and allochems (Figure 4.4 C-D) (in the form of mega-quartz in the intergranular porosity) (Figure 4.4 C-D). XRD analysis indicates the mineralogical composition of this facies is calcite (81.2 %), albite (2.7 %), quartz (11 %), illite (2.9 %), and pyrite (0.8 %) (Table 4.1). The total organic carbon abundance was measured to be at 0.61 % have a $\delta^{13}\text{C}_{\text{OM}}$ signature of -27.1 ‰ (Table 4.1). In bulk carbonate samples the $\delta^{13}\text{C}_{\text{calcite}}$ of was measured to be +2.9 ‰ and the $\delta^{18}\text{O}_{\text{calcite}}$ - 4.9 ‰ (Table 4.1).

Across this facies the ITRAX scanner identified a relatively high response from Ca and low response from Si (Figure 4.9). At random intervals the scan identified corresponding increases in the Fe and S response, likely related to pyrite identified in the facies. Minerals suggesting a detrital input (K, Al, and Mg) were all found to be very low to below detection with the scan. In one sample a burrow was identified across the centre of which Si increased with a corresponding decrease in Ca and Sr.

4.4.3. Homogenized pseudo-sparry calcite- and silt-rich calcareous mudstone

This well-indurated completely homogenous pseudo-sparry calcite-rich calcareous mudstone has no visible bedding preserved (Figure 4.5). The pseudospar crystals are a neomorphic (recrystallization) calcite fabric with crystal sizes ranging from 10 to 250 μm (Figure 4.5 B-C). In addition to the pseudospar crystals, calcite occurs as comminuted bioclastic debris and as cement surrounding these crystals/grains and filling in pore spaces (Figure 4.5 B-F).

The relative small fraction of framework grains include quartz and feldspars (albite) ranging in size from <3 to 50 μm (Figure 4.5 E-F). The plagioclase has trigonal rhombohedral crystal structure. The similarity in shape to many of the dolomite grains in the formation suggests that albite may be of diagenetic origin replacing earlier dolomite (Figure 4.5 E-F). A minor amount of diagenetic pyrite also occurs in this facies (Figure 4.5 E-F). XRD analysis indicates the mineralogical composition of this facies is calcite (86.4 %), quartz (8.3 %), illite (3.4 %), albite (2.8 %), pyrite (1.1 %) and apatite (0.7 %) (Table 4.1). Due to the very high concentrations of calcium carbonate, TOC analysis was not conducted on any of the samples from this facies. In bulk carbonate samples the $\delta^{13}\text{C}_{\text{calcite}}$ was measured to be +1.6 ‰ and the $\delta^{18}\text{O}_{\text{calcite}}$ -6.1 ‰ (Table 4.1).

The XRF scan revealed similar information as the petrographic investigation. Across the samples the Ca response was consistently high, while Si and K were found to have a low response (Figure 4.9). Low Si and K is likely a result of the low concentration of detrital minerals in the facies. The elements Al and Mg were identified in variable abundance (low to moderate). The source of Al and Mg is likely related to the

distributions of albite and dolomite respectively. Fe and S were low, likely due to low concentrations (~1%) of diagenetic pyrite in the facies.

4.4.4. Homogenized silt-bearing clay-rich calcareous mudstone with broken skeletal debris

This homogenized silt-bearing clay-rich calcareous mudstone contains relatively large pieces of broken skeletal debris (100 to >1000 μm) (Figure 4.6). While some of the skeletal material is partially broken, a significant amount is still intact (Figure 4.6 A-E). In comparison the detrital siliciclastic minerals present in this facies are very fine grained with a grain sizes ranging from clay to silt (<3 to 50 μm) (Figure 4.6 C-F). Burrows containing a mixture of coarse-grained carbonates, and more fine-grained of clays, feldspars and quartz are common throughout. Identifiable fossils preserved in the framework fraction include echinoderms (Figure 4.6 D), and brachiopods (Figure 4.6 B).

The matrix material of this facies is predominantly composed of very fine-grained quartz, clays and some feldspar, in the form of plagioclase (albite) (Figure 4.6 F). Pyrite occurs in a euhedral form, and is commonly also present as a replacement of large skeletal grains (Figure 4.6 E). XRD analysis indicates the mineralogical composition of this facies is calcite (52.8 %), quartz (26 %), illite (17 %), albite (3.2 %), and pyrite (1.1 %) (Table 4.1). Total organic carbon of this facies was measured to be 0.76% (Table 4.1).

Overall the framework and matrix fractions are predominantly composed of clastic and clay minerals as were identified in the scan with high Si, K, and variable responses of Mg and Al (Figure 4.9). Overall Ca was identified to have a relatively low response with positive aberrations occurring when the scan passed over some of the large skeletal debris (composed of calcite). Relatively high Fe and S were also identified in this

facies corresponding to increased concentrations of pyrite infilling portions of the large skeletal debris.

4.4.5. Homogenous silt-bearing clay-rich calcareous mudstone

Homogenous silt-bearing clay-rich mudstone contains framework grains of re-worked skeletal debris composed of calcite ranging in size from 10 to 100 μm and detrital quartz and feldspars ranging in size from <3 to 30 μm (Figure 4.7). While the initial fabrics are barely discernable in these units, discontinuous beds are partially preserved (Figure 4.7 A-B). The original bedding features have been disrupted by a combination of soft sediment deformation and bioturbation. Soft sediment deformation has imparted a convolute fabric (Figure 4.7 A-B). Escape traces, which crosscut the convolute bedding (Figure 4.7 A-B) are also present. These escape burrows are lined by a thin layer composed of organic matter and pyrite and contain burrow fills composed of mineral mixtures of feldspars (albite and corroded K-feldspar), clays and a diagenetic ferroan-dolomite as oppose to calcite, which is common throughout the rest of the facies (Figure 4.7 D). Calcite occurs as a cement forming rims around framework grains (Figure 4.7 C). Minor amounts of framboidal pyrite are present throughout. XRD analysis indicates the mineralogical composition of this facies is calcite (72.6 %), quartz (11.8 %), illite (5.8 %), albite (8.6 %), and pyrite (1.2 %) (Table 4.1). Total organic carbon of this facies was measured to be 0.76 have a $\delta^{13}\text{C}_{\text{OM}}$ signature of -28.8 ‰ (Table 4.1). In bulk carbonate samples the $\delta^{13}\text{C}_{\text{calcite}}$ was measured to be +2.7 ‰ and the $\delta^{18}\text{O}_{\text{calcite}}$ -6.0 ‰ (Table 4.1).

The ITRAX scan of this facies identified a moderate response from both Ca and Si (Figure 4.9). Small-elevated Ca concentrations are present at the base of individual

(discontinuous) beds, likely as a result of the increased amount and size of shell debris at the base of beds. All other elements were identified to have variable responses.

4.4.6. Thin-bedded normally graded fossil-bearing, silt-rich calcareous mudstone

This thin-bedded, normally graded fossil-bearing, silt-rich calcareous mudstone contains significant volumes of fossil debris (50 to 2000 μm) (Figure 4.8). The individual beds are normally graded and have fossil lags at their bases and bioturbated tops (*Phycosiphon isp.*) (Figure 4.8 B-C). While much of the fossil debris has an indeterminate origin, fragments of fenestrate bryozoans, bivalves, crinoids and echinoderm are identifiable (Figure 4.8 A-D).

The detrital fraction range in size from <3 to 25 μm and is composed of quartz, feldspar and clays (Figure 4.8 E-F). Calcite is present both as the skeletal debris and as cement, although not as extensive as in other facies, due to a greater amount of detrital material (particularly quartz) (Figure 4.8 E-F). XRD analysis indicates the mineralogical composition of this facies is calcite (64.3 %), quartz (22.3 %), illite (5 %), albite (2.9 %), dolomite (1.6 %) and pyrite (1.2 %) (Table 4.1). Total organic carbon data is not available for this facies (Table 4.1).

The ITRAX scan identified a moderate response from Ca and a moderate to high response from Si (Figure 4.9). The bases of individual beds are shell rich with larger grain sizes resulting in an increased Ca response. Moving upwards from the base of the beds there is less Ca and higher response from Si, and K, Mg and Al. Fe and S contained variable responses across samples from this facies due to pyrite preserved in portions of shell material.

4.4.7. Overall stacking patterns

Across the measured section of the formation there appear to be two genetically related sections, a lower portion and an upper portion. In the lower section (from the base of the measured section to approximately 4.7 m) and an upper portion (4.7 to 6 m). In the lower section a series of repeating coarsening upward units ranging from 0.25 m to 1.75 m is present. These units commonly contain a more fine-grained clastic and shell debris bearing section underlying a more coarse-grained and bioturbated interval. Intervals that haven't been completely bioturbated suggest this lower section contains sediment delivered via processes that have preserved erosive surfaces and fining upward fabrics.

Approximately 4.7 m above the base a shift occurs. Above this level rhythmic repeating series of much thinner units (0.1 to 0.25 m) are present (Figure 4.2). In this part of the succession the repeating series of units comprise burrow mottled silt-bearing clay-rich mudstone at their base that are overlain by homogenized and indurated calcareous mudstones. The framework material of these homogenous units is primarily composed of silt-sized pseudospinel crystals of calcite suggesting a possible diagenetic origin. The less cemented units have an abundance of trace fossils and a higher input of detrital framework minerals, e.g. silt sized quartz and feldspars (e.g. Figure 4.3).

4.5. DISCUSSION

4.5.1. Fine-grained sediment production, delivery and accumulation

The lithofacies present are predominantly composed of calcareous mudstones with varying lamina geometries and intensities of bioturbation. The framework fraction of the Benbulbin Shale is composed of material derived from two sources i) reworked silt to sand sized skeletal debris composed of calcite and ii) detrital quartz and feldspars

derived from weathering in the hinterland that was supplying sediment to the basin. The matrix and framework fractions of the unit are composed of silt to fine sand (framework) and clay-sized (matrix) skeletal debris (calcite), quartz, feldspars (mainly albite) and clays (primarily illite). Most of this material was either supplied to the basin by rivers or produced in the basin by biological processes (Ghadeer and Macquaker, 2011). The very fine-grained material would suggest it has been transported a much further distance than the bioclastic debris. This difference in source likely results from production derived bioclastic debris being produced in the basin and being transported only short distances from the site of production (Aplin and Macquaker, 2011).

Although disarticulated skeletal debris is found throughout the formation, the degree of abrasion varies considerably between facies. In some facies it is possible to identify either whole or mostly intact fossils including: fenestrate bryozoans, echinoderm fragments, and crinoid's spines. In some facies however the debris is fragmented to the point where the initial fossils are unidentifiable. The differences in the degree of sorting suggest shifts in the point along the sediment transport path where production was occurring with the more fine-grained facies representing a longer path and more coarse fractions a shorter path (Ghadeer and Macquaker, 2011).

Although most primary sedimentary structures (and bedding planes) have been disrupted by bioturbation, the few structures that are preserved suggest normally graded beds with a shell-rich lags at their bases (Figure 4.7, Figure 4.8). This type of bedding feature is commonly a product of episodic storm deposition on the distal portion of shelves – i.e. muddy tempestites (Aigner and Reineck, 1982). The presence of these fabrics indicates that these beds were deposited above storm wave base (Aigner and

Reineck, 1982). In some instances soft sediment deformation has disrupted the sediment prior to it being bioturbated. This fabric suggests the sediment founded prior to it being colonized suggesting that large volumes of materials were delivered to the sediment as discrete events that had a higher recurrence frequencies than the rate of colonization (Aplin and Macquaker, 2011; Bohacs et al., 2005).

4.5.2. Bioturbation

As indicated above there are a number of bioturbation styles preserved in the Benbulbin shale with the types of burrows and assemblages present varying between different facies. The prevalence of bioturbation throughout the succession suggests that the geochemical conditions of the water column remained oxygenated throughout the deposition of the formation (Gingras et al., 2011). The intensity of bioturbation reflects the rate of sediment accumulation with increased sediment accumulation being related to lowered bioturbation intensities (Bentley et al., 2006; Ghadeer and Macquaker, 2011). The most common facies (i.e. burrow mottled silt-bearing clay-rich mudstone with broken skeletal debris) contains an abundance of *Nerities isp.* and *Phycosiphon isp.* These two traces represent slightly different depositional environments. *Nerities isp.* are generally indicative of deep-water (Chamberlain and Clark, 1989) however they have been reported in shallow-water basins as well (Pemberton et al., 2002). Ekdale and Mason (1988) suggested that rather than representing deep basinal environments *Nerities isp.* may indicate environments with stressed oxygen or salinity conditions. Due to the dominance of *Phycosiphon isp.* traces, which typically represents normal marine shallow shelf type environments, combined with the presence of nearly intact fossil debris it appears that the Benbulbin shale was most likely deposited in a normal marine shallow

shelf environment (Bednarz, 2009; Goldring et al., 1991). The presence of *Neritites isp.* is most likely indicative of periods of stressed salinity and oxygen conditions (Ekdale and Mason, 1988; Gingras et al., 2011).

4.5.3. Diagenetic attributes

Much of the calcite is present in the Benbulbin Shale as cement. This cement infills pre-compaction pore space and is therefore likely to have precipitated close to the sediment water interface (Morse et al., 2007). The range of $\delta^{13}\text{C}$ values of these cements indicates that there is no significant depletion from seawater values, which suggests that the carbon for this cement was supplied either from; the dissolution of calcite and metastable aragonite containing tests of organisms and/or, directly from seawater (Whiticar, 1999). Iron-reduction likely occurred in the sediment during this time period leading to the breakdown of organic matter which further supplied inorganic carbon for calcite precipitation in the sediment (Adams et al., 2003; Morse et al., 2007). At some time after the precipitation of calcite cement, but pre-compaction, the pore-waters became sulfidic and more reducing resulting in pyrite precipitation (Taylor and Macquaker, 2000). Pyrite occurs both in euhedral (replacing shell fossils) and framboidal forms (e.g. Figure 4.6 E, Figure 4.7 D, Figure 4.8 F) (Berner, 1984; Schoonen and Barnes, 1991; Van Cappellen, 2003). Some euhedral pyrite is similar to the shape of the corroded pyrite grains and therefore may also be a pseudomorphic replacement of dolomite (Figure 4.4 D).

Feldspar and quartz are also present as diagenetic minerals. Albite often occurs either (i) as a rim around corroded dolomite grains or (ii) as a complete pseudomorphic replacement of previous diagenetic dolomite (Figure 4.4 E-F, Figure 4.5 E-F) (Nesbitt et al., 1997; Putnis, 2002; Putnis, 2009).

4.5.4. Interpretation of stacking patterns and implications for petrophysical properties

Throughout the measured succession the cycle of switching between rocks with larger and smaller grain sizes (i.e. upward coarsening sequences) likely reflects periods of increased and decreased sediment supply (Ghadeer and Macquaker, 2011). During periods of moderate to high sediment delivery more fine-grained material transported from a weathered continental source was deposited (Aplin and Macquaker, 2011). This led to a variably burrow mottled, generally silt-bearing clay-rich mudstones. In these units the clastic component is greater and there are lower concentrations of calcium, leading to less extensive carbonate cements.

During periods of low sedimentation delivery rates the production component makes up a more significant fraction of the mudstones (Bohacs et al., 2005; Sageman et al., 2003). This production component often contained greater grain sizes resulting in the coarser grained units overlying the more fine-grained clastic units. During the periods of low sediment delivery a greater amount of time was available for the precipitation of extensive carbonate cements (Morse et al., 2007). These units were generally preserved as homogenized, silt-rich calcareous mudstones. The low sedimentation delivery rates also provided the time necessary for the complete destruction of bedding planes by burrowing organisms (Pemberton et al., 2008).

At approximately 4.7 m there was a shift, which occurred and appears to correspond to increased sediment recurrence frequency (Ghadeer and Macquaker, 2011). Above this point the sediment no longer had enough time for much carbonate cement to precipitate in the more fine-grained units. Furthermore the length of the cycles was shorter as each interval from low to high sediment delivery is shorter (e.g. 0.2 m).

The stacking patterns of the more clastic and more carbonate-rich units may have significant implications for any potential reservoir characteristics of the formation. Specifically, the more indurated units are more likely to fracture (Rijken and Cooke, 2001). The more clastic rich, less cemented units may, however cause a baffle to any fracturing activity (Rijken and Cooke, 2001). In the upper section with lower sediment higher sediment recurrence frequency this may be particularly important due to the small spacing (e.g. ~ 0.2 m) between the two types of mudstones as it may significantly decrease the overall fracturability.

4.5.5. Scale of compositional variability

In the ITRAX XRF scan the relationship between the calcium and silicon response trends is particularly significant as in a broad sense it is possible to distinguish between carbonate-rich and clay-rich facies. (Croudace et al., 2006). Facies, which corresponded to increases in the Ca response trend, tend to correspond to carbonate-rich mudstone facies. Facies, which correspond to increases in Si response, tend to relate to fine-grained siliciclastic material often present in clay-rich facies.

In individual beds there is significant variation as a result of both bioturbation and sedimentary structures. The normally graded beds contain a significant amount of shell debris that forms lags at their bases and are more enriched in clay minerals towards their tops. The bases of the beds are therefore richer in Ca and Sr, in contrast to their upper portions that are more enriched in Si, Al, and K. This pattern was likely a product of deposition from storms in distal settings with these units being distal mud tempestites (Aigner and Reineck, 1982) and leads to beds exhibiting significant small-scale variability.

On a bed-set scale the boundary between beds is very clear as there are distinct boundaries relating due to differences in elemental composition. The shift from the less to more cemented units (which is common throughout the succession) corresponds to a large sudden increases in Ca and a corresponding significant decrease in Si (and other elastic associated elements, Al, K, etc.). At some boundaries this distinct shift has been overprinted by bioturbation, which results in a less clear signal of bedding planes.

In relation to the 2 overall sections of the formation there is an general increase in Si and other elastic derived elements in samples from above ~4.7 m. This is likely due to an increase in sediment recurrence frequency. The higher frequency of elastic derived sediment flux to the basin limited both the production input and the time for diagenetic cements to precipitate, relative to the section below ~4.7 m, leaving increased Si and generally decreased Ca (Bohacs et al., 2005).

This data highlights the extent of heterogeneity in fine-grained rocks (Figure 4.9). Not only is there large heterogeneity between samples, but also within the sample itself. Inevitably, conventional XRF analyses that are performed on hand-specimen sized samples does not record the significant variability that is observed on the scale of individual beds. To compare between the pressed pellet and ITRAX scanning techniques the average response for each element was calculated from the all data points across individual samples (Figure 4.10). This comparison between the conventional XRF analysis and ITRAX scanner suggest that while bulk analysis of XRF samples are useful to provide insights into large scale trends, scanning techniques can provide high-resolution data, which in very fine-grained rocks elucidates a high degree of heterogeneity that typically is masked by bulk analysis. The similarity between the two

techniques in the comparison confirmed that while the ITRAX scan did not provide quantitative values the response trend is very accurate.

4.6. CONCLUSIONS

A high degree of lithofacies heterogeneity was observed in the relatively short measured succession of the Benbulbin Shale. The heterogeneity was present across a range of scales from macroscopic to microscopic and in all components of the rock (i) production – shifts in size and type of fossil debris, (ii) detrital – shifts in abundance and size of clastic input, and (iii) diagenetic – a range of diagenetic features with more and less cemented units. This variability is significant as it has important implications for the rocks reservoir and source rock attributes as well as the ability to hydrofracture. The significant amount of heterogeneity was easily observed through the high-resolution ITRAX XRF scan across the samples between bed-sets and within individual beds (e.g. calcium rich at the base and silicon rich at the tops of individual beds).

Comparison between conventional XRF techniques (pressed pellet) and the ITRAX scanning technique yielded remarkably consistent results. These results suggest that while bulk analysis of XRF samples are useful to provide insights into bulk trends, scanning techniques can provide high-resolution data, which in very fine-grained rocks elucidates a high degree of heterogeneity which is masked by bulk analysis.

4.7. TABLES

Table 4.1: Analytical Results of Benbulbin Shale

SPY Sample No.	SPY 0.00	SPY 0.05	SPY 0.10	SPY 0.15	SPY 0.20	SPY 0.25	SPY 0.30	SPY 0.35	SPY 0.40	SPY 0.45	SPY 0.50	SPY 0.55	SPY 0.60	SPY 0.65	SPY 0.70	SPY 0.75	SPY 0.80	SPY 0.85	SPY 0.90	SPY 0.95	SPY 1.00		
Inorganic Analysis																							
SiO ₂	57.4	-	1.6	-	27.9	-	-	-	-	9.9	-	-	-	-	26.8	-	-	27.6	-	26.4	-	57.7	
Al ₂ O ₃	-	-	4.1	-	-	-	-	-	-	-	-	-	-	-	4.0	-	-	3.7	-	4.0	-	4.4	
FeO	17.7	12.8	9.3	26	3	27.9	22.3	18.9	156	79	7.3	11.8	18.3	17.9	16.7	8.1	20.1	18.3	17.4	18.3	17.4	17.4	17.4
CaO	1.7	7.3	-	0.3	1.3	7.1	-	-	0.9	0.9	0.9	0.9	0.9	0.9	0.9	0.9	0.9	0.9	0.9	0.9	0.9	0.9	0.9
MgO	1.7	7.3	-	0.3	1.3	7.1	-	-	0.9	0.9	0.9	0.9	0.9	0.9	0.9	0.9	0.9	0.9	0.9	0.9	0.9	0.9	0.9
Na ₂ O	-	1	-	1.1	-	0.7	1.2	-	1.7	1.1	1.7	0.7	0.7	0.7	0.6	1.4	0.6	1.4	0.6	1.4	0.6	1.4	0.6
K ₂ O	106	106	106	106	106	106	106	106	106	106	106	106	106	106	106	106	106	106	106	106	106	106	106
SO ₄	0	1	-	88.1	88.1	88.1	88.1	88.1	88.1	88.1	88.1	88.1	88.1	88.1	88.1	88.1	88.1	88.1	88.1	88.1	88.1	88.1	88.1
CO ₂	3	3	2	3.2	2.4	2.1	2.9	4.4	1.2	2.6	3.5	8.6	-	-	3.7	5.5	1.4	7.7	-	4.6	-	4.6	-
Loss on Ignition	-	-	0.7	-	-	-	-	-	-	-	-	-	-	-	-	-	-	-	-	-	-	-	-
Organic	3	3	1	0	2.4	2.1	2.9	4.4	1.2	2.6	3.5	8.6	-	-	3.7	5.5	1.4	7.7	-	4.6	-	4.6	-
Chloride	3.7	3.3	9	17	0.8	3.3	7.7	4.1	0	13.6	3.4	5.8	17	4.7	5.6	-	-	9.6	4	4.5	-	4.5	-
SPY Elements																							
Major Elements																							
wt%	33.100%	18.00%	16.00%	14.00%	11.00%	11.00%	14.00%	14.00%	14.00%	14.00%	14.00%	14.00%	14.00%	14.00%	14.00%	14.00%	14.00%	14.00%	14.00%	14.00%	14.00%	14.00%	14.00%
wt%	4.00%	1.44%	0.60%	0.74%	1.36%	3.17%	4.57%	4.73%	3.50%	3.00%	1.60%	1.60%	1.60%	1.60%	1.60%	1.60%	1.60%	1.60%	1.60%	1.60%	1.60%	1.60%	1.60%
wt%	2.77%	2.65%	1.07%	2.64%	2.64%	2.64%	2.64%	2.64%	2.64%	2.64%	2.64%	2.64%	2.64%	2.64%	2.64%	2.64%	2.64%	2.64%	2.64%	2.64%	2.64%	2.64%	2.64%
wt%	1.18%	1.18%	1.18%	1.18%	1.18%	1.18%	1.18%	1.18%	1.18%	1.18%	1.18%	1.18%	1.18%	1.18%	1.18%	1.18%	1.18%	1.18%	1.18%	1.18%	1.18%	1.18%	1.18%
wt%	42.16%	35.52%	35.52%	35.52%	35.52%	35.52%	35.52%	35.52%	35.52%	35.52%	35.52%	35.52%	35.52%	35.52%	35.52%	35.52%	35.52%	35.52%	35.52%	35.52%	35.52%	35.52%	35.52%
wt%	0.37%	0.88%	0.10%	0.10%	0.25%	0.36%	0.69%	0.77%	0.40%	0.40%	0.40%	0.40%	0.40%	0.40%	0.40%	0.40%	0.40%	0.40%	0.40%	0.40%	0.40%	0.40%	0.40%
wt%	0.85%	0.85%	0.85%	0.85%	0.85%	0.85%	0.85%	0.85%	0.85%	0.85%	0.85%	0.85%	0.85%	0.85%	0.85%	0.85%	0.85%	0.85%	0.85%	0.85%	0.85%	0.85%	0.85%
Trace Elements																							
ppm	7827	5870	3823	5311	3527	7717	9036	8267	7164	18667	6537	16270	8427	8937	1656	8267	8937	1656	8267	8937	1656	8267	8937
ppm	476	417	357	438	588	440	441	444	444	444	444	444	444	444	444	444	444	444	444	444	444	444	444
ppm	22	28	28	24	33	29	21	25	29	35	35	36	36	36	36	36	36	36	36	36	36	36	36
ppm	41	41	41	41	41	41	41	41	41	41	41	41	41	41	41	41	41	41	41	41	41	41	41
ppm	41	41	41	41	41	41	41	41	41	41	41	41	41	41	41	41	41	41	41	41	41	41	41
ppm	11	11	11	11	11	11	11	11	11	11	11	11	11	11	11	11	11	11	11	11	11	11	11
ppm	41	41	41	41	41	41	41	41	41	41	41	41	41	41	41	41	41	41	41	41	41	41	41
ppm	41	41	41	41	41	41	41	41	41	41	41	41	41	41	41	41	41	41	41	41	41	41	41
ppm	22	22	22	22	22	22	22	22	22	22	22	22	22	22	22	22	22	22	22	22	22	22	22
ppm	285	43	47	40	31	191	172	263	196	196	196	196	196	196	196	196	196	196	196	196	196	196	196
ppm	163	163	163	163	163	163	163	163	163	163	163	163	163	163	163	163	163	163	163	163	163	163	163
ppm	91	65	105	98	79	141	112	179	125	113	92	128	116	110	69	67	114	111	110	69	67	114	111
ppm	42.3	21.7	19.8	48.0	29.2	26.3	42.0	37.0	46.3	29.4	29.3	29.9	29.1	28.2	29.3	29.3	29.3	29.3	29.3	29.3	29.3	29.3	29.3
ppm	4.4	3.3	3.8	3.5	3.5	3.7	3.7	3.7	3.7	3.7	3.7	3.7	3.7	3.7	3.7	3.7	3.7	3.7	3.7	3.7	3.7	3.7	3.7
ppm	5	5	5	5	5	5	5	5	5	5	5	5	5	5	5	5	5	5	5	5	5	5	5
ppm	41	41	41	41	41	41	41	41	41	41	41	41	41	41	41	41	41	41	41	41	41	41	41
ppm	41	41	41	41	41	41	41	41	41	41	41	41	41	41	41	41	41	41	41	41	41	41	41
ppm	41	41	41	41	41	41	41	41	41	41	41	41	41	41	41	41	41	41	41	41	41	41	41

4.8. FIGURES

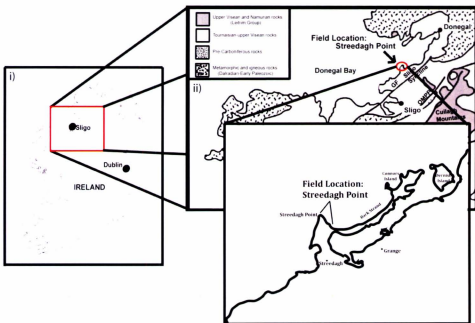


Figure 4.1: i) Map of Ireland demonstrating location of field site at Streedagh Point in Sligo Co. Ireland. ii) Geologic map demonstrating regional geology of Northwest Ireland and significant syncline structures in the region, BF – Belhavel Fault, CF – Curlew Fault, CVF – Clogher Valley Fault, GF = Grange Fault, OMPF = Ox Mountains – Pettigoe Fault (Modified from Aretz et. al., 2010, after Dixon, 1972).

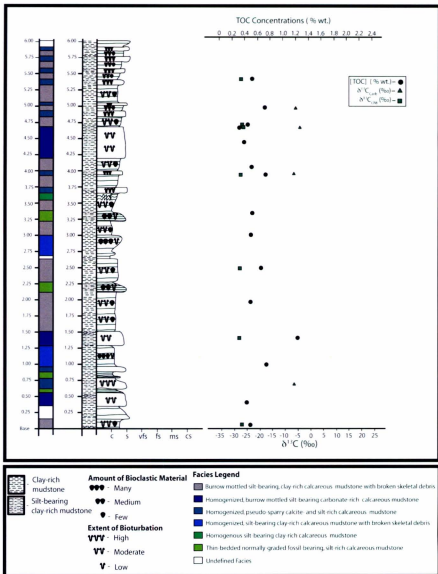


Figure 4.2: Stratigraphic log of measured section of the Benbulbin Shale at Streedagh Point, in Sligo County, Ireland.

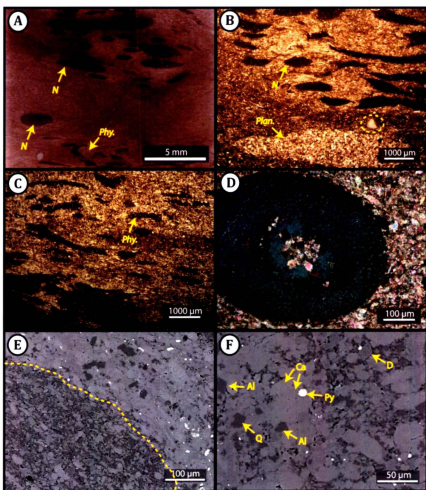


Figure 4.3: Petrographic observations of the burrow mottled silt-bearing, clay-rich calcareous mudstone with broken skeletal debris. (A) Scan of thin section demonstrating significant preservation of trace fossils. (B-D) Optical images from petrographic microscope demonstrating the variety of trace fossils; *N* – *Nereites* *isp.*, *Phy* – *Phycosiphon* *isp.*, *Plan* – *Planolites* *isp.*. Circled in B is an Echinoderm fragment (E-F) Backscatter electron optical micrographs. Dashed line in E represents the boundary of a burrow. Mineralogy is arrowed and labeled as; Q – quartz, Ca – calcite, D – dolomite, Al – albite, and Py – Pyrite.

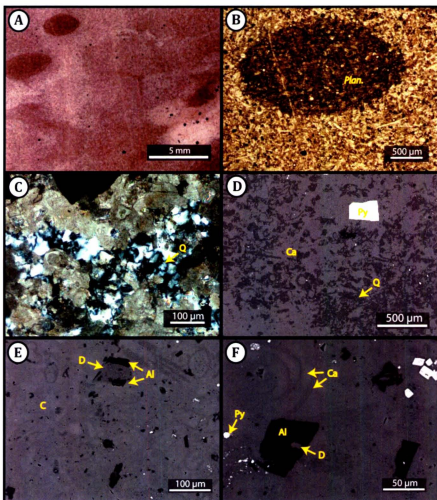


Figure 4.4: Petrographic observations of the homogenized, burrow mottled silt-bearing carbonate-rich calcareous mudstone. (A) Scan of thin section. (B-C) Optical images from petrographic microscope; *Plan* – *Planolites isp.*. Diagenetic quartz is visible in C. (D-F) Backscatter electron optical micrographs. Multiple (production and diagenetic) forms of calcite are visible in D-F. Pyrite (D) and Albite (E-F) can be seen occurring as a pseudomorphic replacement of dolomite. Mineralogy is arrowed and labeled as; Q – quartz, Ca – calcite, D – dolomite, Al – albite, and Py – Pyrite.

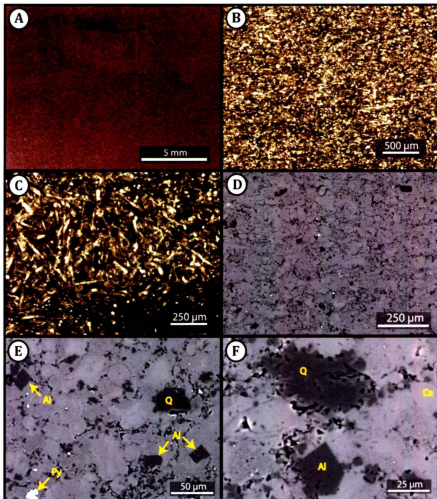


Figure 4.5: Petrographic observations of the homogenized, pseudo-sparry calcite- and silt-rich calcareous mudstone. (A) Scan of thin section. (B-C) Optical images from petrographic microscope with visible pseudo-sparry calcite. (D-F) Backscatter electron optical micrographs. Pyrite (D) and Albite (E-F) can be seen possibly occurring as a pseudomorphic replacement of dolomite. Mineralogy is arrowed and labeled as; Q – quartz, Ca – calcite, Al – albite, and Py – Pyrite.

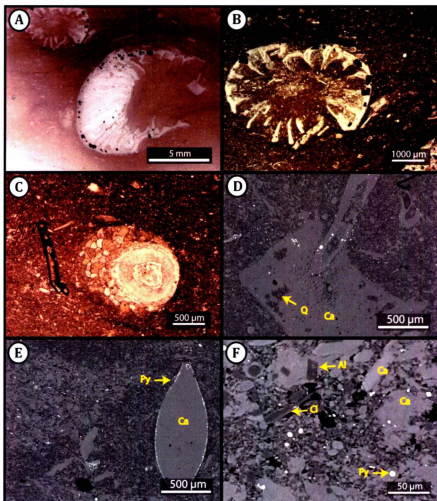


Figure 4.6: Petrographic observations of the homogenized, silt-bearing clay-rich calcareous mudstone with broken skeletal debris. (A) Scan of thin section. (B-C) Optical images from petrographic microscope (D-F) Backscatter electron optical micrographs. Visible fossils are abundant in this facies including brachiopods (A-B) and echinoderms (B, D-E). Mineralogy is arrowed and labeled as; Q – quartz, Ca – calcite, Al – albite, Cl – chlorite and Py – Pyrite.

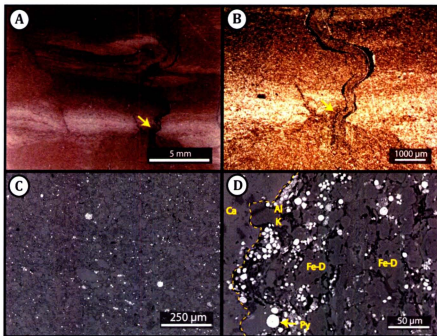


Figure 4.7: Petrographic observations of the homogenous silt-bearing clay-rich calcareous mudstone. (A) Scan of thin section demonstrating soft sediment deformation, which is cross cut by an escape trace. (B) Optical image from petrographic microscope. (C-D) Backscatter electron optical micrographs. B shows escape trace and D demonstrates the composition of the escape trace, with a greater amount of fine grained and organic rich material. Mineralogy is arrowed and labeled as; Q – quartz, Ca – calcite, Al – albite, Cl – chlorite Fe-D – ferroan dolomite and Py – Pyrite.

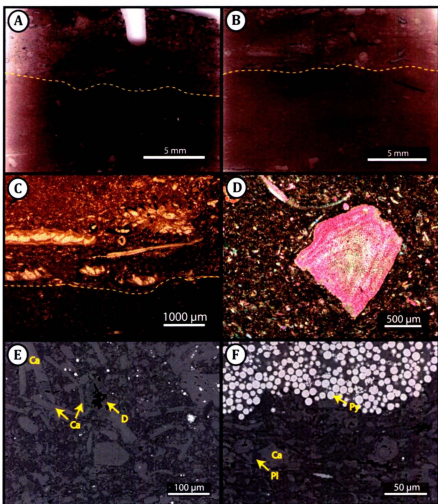


Figure 4.8: Petrographic observations of the thin-bedded normally-graded fossil-bearing, silt-rich calcareous mudstone. (A) Scan of thin section demonstrating an uneven erosional surface at the base of a bed. (B-D) Optical images from petrographic microscope. C demonstrates the upward fining nature of the beds (E-F) Backscatter electron optical micrographs. The dissolution of a dolomite can be observed in E. Mineralogy is arrowed and labeled as; Ca – calcite, Al – albite, and Py – Pyrite.

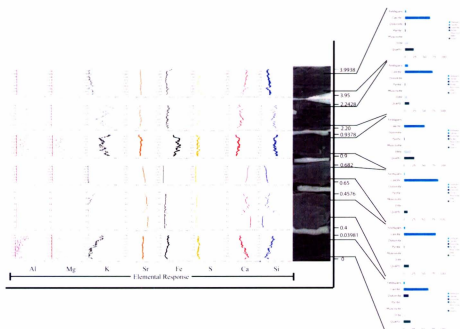


Figure 4.9: Results from ITRAX X-ray Fluorescence (XRF) data at 2 mm vertical intervals across a selection of the samples collected.

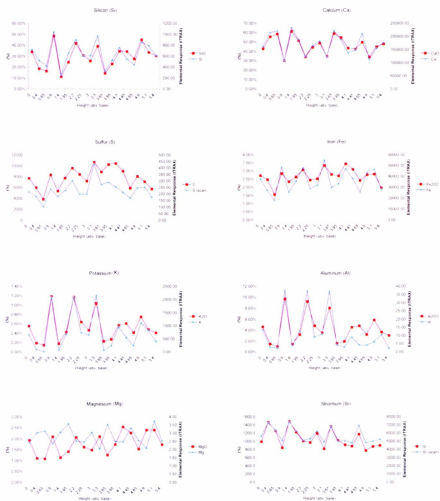


Figure 4.10: Comparison between conventional XRF and high resolution ITRAX XRF scan techniques.

5. : CONCLUSIONS

The main aims of this study were to collect and characterise mudstones of varying ages and environments to highlight the significant heterogeneity, which exists both within and between these successions. Samples from four different successions and two different geologic time periods were collected. The results from the analysis of these successions are discussed as follows.

The lithofacies and iron-disulfide investigation of the Devonian aged Exshaw Formation indicate the following:

- Total of 5 lithofacies identified with a mix of sandstones and thin-bedded mudstones.
- Agglutinated benthic foraminifera suggests oxic to dysoxic conditions in the bottom waters of the basin.
- Pyrite and marcasite cements identified in the succession, with a significant abundance in the basal arkosic sandstone.
- One population of pyrite appears to be syngenetic while another formed at a later time during burial diagenesis.
- Marcasite appears to be epigenetic because it has a different source (much less evolved - abiogenic) of sulfur relative to pyrite.
- Isotopic analysis combined with textural observations suggests marcasite formation may be the result of a process similar to that, which forms Lead-Zinc type ore deposits.

- Presence of marcasite alone therefore, cannot suggest that oxygen (or any other oxidant) was available in the pore-waters during the deposition of a mudstone.

Comparison between lithofacies characterizations between two Ordovician aged mudstones of the Utica and Winterhouse Formations indicated the following:

- Total of 7 lithofacies identified in the measured section of the Utica and 4 in the measured interval of the Winterhouse Formation.
- Sediment in Utica and Winterhouse was delivered from both allochthonous (quartz, feldspars and clay minerals) and autochthonous sources.
- Sediment was dispersed primarily by waning processes (storms), but also occasionally from suspension settling.
- Sediments in the Winterhouse Formation were deposited more proximally on sediment transport path compared to those of the Utica Formation.
- Contrary to published models neither succession was deposited during prolonged periods of bottom water anoxia although sediment pore waters were sulfidic.
- Feldspar dissolution is common in both but more extensive in the Winterhouse.
- Significant carbonate diagenesis occurred in the Winterhouse and to a lesser extent in the Utica, specifically grain dissolution coupled with cement precipitation.

- Carbon isotopic data suggests solutes for carbonate cements were derived both from (i) early microbial degradation of organic matter - some of which was methanogenic, and (ii) dissolution of carbonate shells.
- Large volumes of carbonate cement in the Winterhouse suggest that microbial decay was responsible for much of the degradation of the source rock potential.
- In spite of having similar total carbonate contents there is less cement in the Utica making its reservoir potential greater.
- Carbonate cements in both successions increase their susceptibility to fracturing.
- Neither of the formations are ideal source rocks.

The lithofacies investigation and comparison between XRF techniques using the Late Devonian – Early Carboniferous aged Benbulbin Shale indicated:

- A high degree of lithofacies (6 identified) heterogeneity in a relatively short measured succession.
- Heterogeneity was present across a range of scales from macroscopic to microscopic and in all components of the rock (i) production – shifts in size and type of fossil debris, (ii) detrital – shifts in abundance and size of clastic input, and (iii) diagenetic – a range of diagenetic minerals with more and less cemented units.
- This variability is significant as it has important implications for the rocks reservoir and source rock attributes as well as the ability to hydrofracture.

- The significant amount of heterogeneity was easily observed with the high-resolution ITRAX XRF scan.
- The scale of elemental heterogeneity ranged from bed-sets to within individual beds (e.g. calcium rich at the base and silicon rich at the tops of individual beds).
- It was not possible to identify the same scale of heterogeneity from the conventional XRF techniques, due to the very thin beds which occurs in these fine-grained rocks.
- While conventional analysis of XRF samples provide useful insights into bulk trends, scanning techniques can provide high-resolution data, which in very fine-grained rocks better elucidate the high degree of heterogeneity that is often masked by bulk analysis.

A particular emphasis was placed on comparing early and late Palaeozoic successions to determine if secular changes can be observed that are consistent with the input of detrital materials with different starting compositions, and the effects of inputs from different microfossil groups. This stratigraphic interval was chosen because it is the time period associated with the evolution of land plants and the development of extensive soil profiles on land.

The anticipation of the project was that the type of weathering and inputs changes, which have altered through time, would have an intrinsic effect on the resulting mudstone composition. This was found to be true as a significant amount of variability was observed between mudstones from different time periods. Mudstones, which were

deposited in time periods prior to the evolution of soils on land, contained much more variability in mineralogical composition and that crucially they contain materials that are relatively susceptible to chemical weathering (Brady, 1989; Curtis, 1976; Goldich, 1938). In the two successions from the Ordovician a total of 13 minerals were identified with at least 6 to 7 most likely being of a detrital source. While in the samples from the Carboniferous a total of 10 minerals were identified with 4 most likely being of a detrital source. This is likely a result of the fact that as sediment is transported and filtered through soils the increased time and availability of reaction site leads to the dissolution of minerals on land (Algeo et al., 1998; Davies and Gibling, 2010). As the dissolved solutes are transported and deposited in the oceans the range of minerals produced are more likely to be diagenetic and have a smaller overall variety in detrital grains.

It is important to note that there was considerable variability identified not just between different time periods but also between successions. In the two successions from the Carboniferous, one was very silica and clastic rich mudstone, while the other was much more carbonate dominated (Chapter 2 and 4). In the Ordovician both successions were dominated by calcareous mudstones, however significant variability was still identified between the two due to different proportions of sequestered vs. mineralised carbon (Chapter 3). Analysis of any individual mudstone reveals that while they can appear to be very homogenous there is in fact a significant amount of heterogeneity.

BIBLIOGRAPHY

- Adams, L.K., Lloyd, J.R., MacQuaker, J.H.S., 2003. Microbial iron reduction: From bacteria to cement. *Geochimica Et Cosmochimica Acta*, 67(18): A7-A7.
- Aigner, T., Reineck, H., 1982. Proximality trends in modern storm sands from the Helgoland Bight (North Sea) and their implications for basin analysis. *Senckenbergiana Maritima*(14): 183-215.
- Algeo, T.J., Scheckler, S.E., Maynard, J.B., 2001. Effects of the Middle to Late Devonian spread of vascular land plants on weathering regimes, marine biotas, and global climate. In: Gensel P.G., and Edwards, D., *Plants Invade the Land: Evolutionary and Environmental Perspectives*. Columbia University Press: 213-236.
- Algeo, T.J., Scheckler, S.E., Scott, A.C., 1998. Terrestrial-Marine Teleconnections in the Devonian: Links between the Evolution of Land Plants, Weathering Processes, and Marine Anoxic Events [and Discussion]. *Philosophical Transactions: Biological Sciences*, 353(1365): 113-130.
- Aller, R.C., 1994. Bioturbation and remineralization of sedimentary organic matter: effects of redox oscillation. *Chemical Geology*, 114(3-4): 331-345.
- Anderson, G.M., Garven, G., 1987. Sulfate-Sulfide-Carbonate Associations in Mississippi Valley-Type Lead-Zinc Deposits. *Economic Geology*, 82(2): 482-488.
- Angulo, S., Buatois, L.A., 2012. Integrating depositional models, ichnology and sequence stratigraphy in reservoir characterization: The middle member of the Devonian-Carboniferous Bakken Formation of subsurface southeastern Saskatchewan. *AAPG Bulletin* 96(6): 1017-1043.
- Aplin, A.C., Macquaker, J.H.S., 2011. Mudstone diversity: Origin and implications for source, seal, and reservoir properties in petroleum systems. *Aapg Bulletin*, 95(12): 2031-2059.
- Aretz, M., Herbig, H.G., Somerville, I.D., Cozar, P., 2010. Rugose coral biostromes in the late Viséan (Mississippian) of NW Ireland: Bioevents on an extensive carbonate platform. *Palaeogeography, Palaeoclimatology, Paleocology*, 292(3-4): 488-506.
- Baas, J.H., Best, J.L., Peakall, J., Wang, M., 2009. A Phase Diagram for Turbulent, Transitional, and Laminar Clay Suspension Flows. *Journal of Sedimentary Research*, 79(3-4): 162-183.
- Baker, P.A., Kastner, M., 1981. Constraints on the Formation of Sedimentary Dolomite. *Science*, 213(4504): 214-216.
- Balci, N., Shanks I, W.C., Mayer, B., Mandernack, K.W., 2007. Oxygen and sulfur isotope systematics of sulfate produced by bacterial and abiotic oxidation of pyrite. *Geochimica et Cosmochimica Acta*, 71(15): 3796-3811.
- Bednarz, M., McIlroy, D., 2009. Three-Dimensional Reconstruction of "Phycosiphoniform" Burrows: Implications for Identification of Trace Fossils in Core. *Palaeontologia Electronica* 12(3; 13A): 15.

- Belt, E.S., Riva, J., Bussières, L., 1979. Revision and Correlation of Late Middle Ordovician Stratigraphy Northeast of Quebec-City. *Canadian Journal of Earth Sciences*, 16(7): 1467-1483.
- Bentley, S.J., Sheremet, A., Jaeger, J.M., 2006. Event sedimentation, bioturbation, and preserved sedimentary fabric: Field and model comparisons in three contrasting marine settings. *Continental Shelf Research*, 26(17-18): 2108-2124.
- Berger, G., Velde, B., Aigouy, T., 1999. Potassium sources and illitization in Texas Gulf Coast shale diagenesis. *Journal of Sedimentary Research*, 69(1): 151-157.
- Bergstrom, S.M., Riva, J., Kay, M., 1974. Significance of Conodonts, Graptolites, and Shelly Faunas from Ordovician of Western and North-Central Newfoundland. *Canadian Journal of Earth Sciences*, 11(12): 1625-&.
- Berner, R.A., 1967. thermodynamic stability of sedimentary iron sulfides. *Am J Sci*, 265(9): 773-785.
- Berner, R.A., 1984. Sedimentary pyrite formation: An update. *Geochimica et Cosmochimica Acta*, 48(4): 605-615.
- Blake, R.E., Walter, L.M., 1999. Kinetics of feldspar and quartz dissolution at 70-80°C and near-neutral pH: effects of organic acids and NaCl. *Geochimica et Cosmochimica Acta*, 63(13-14): 2043-2059.
- Bohacs, K.M. et al., 2005. Production, Destruction, and Dilution - The Many Paths to Source-Rock Development. Special Publication - SEPM (Society for Sedimentary Geology)(82): 61-102.
- Bottjer, D.J., 2005. Geobiology and the fossil record: eukaryotes, microbes, and their interactions. *Palaeogeography, Palaeoclimatology, Palaeoecology*, 219(1-2): 5-21.
- Bottjer, D.J., Hagadorn, J.W., Dornbos, S.Q., 2000. The Cambrian substrate revolution. *GSA Today*, 10(9): 1-7.
- Brady, P.V., and Walther, J.V., 1989. Controls on silicate dissolution rates in neutral and basic pH solutions at 25°C. *Geochimica et Cosmochimica Acta*, 53(11): 2823-2830.
- Brady, P.V., Walther, J.V., 1990. Kinetics of quartz dissolution at low temperatures. *Chemical Geology*, 82: 253-264.
- Brett, C.E., Baird, G.C., 2002. Revised stratigraphy of the Trenton Group in its type area, central New York State: sedimentology and tectonics of a Middle Ordovician shelf-to-basin succession. *Physics and Chemistry of the Earth*, 27(1-3): 231-263.
- Butler, M., Dam, H.G., 1994. Production-Rates and Characteristics of Fecal Pellets of the Copepod *Acartia-Tonsa* under Simulated Phytoplankton Bloom Conditions - Implications for Vertical Fluxes. *Marine Ecology-Progress Series*, 114(1-2): 81-91.
- Calvert, S.E., 1968. Silica Balance in the Ocean and Diagenesis. *Nature*, 219(5157): 919-920.
- Canfield, D.E., 2001. Biogeochemistry of Sulfur Isotopes. *Reviews in Mineralogy and Geochemistry*, 43(1): 607-636.
- Caplan, M.L., Bustin, R.M., 1996. Factors governing organic matter accumulation and preservation in a marine petroleum source rock from the Upper Devonian to Lower Carboniferous Exshaw Formation, Alberta. *Bulletin of Canadian Petroleum Geology*, 44(3): 474-494.

- Caplan, M.L., Bustin, R.M., 1999. Palaeoceanographic controls on geochemical characteristics of organic-rich Exshaw mudrocks: role of enhanced primary production. *Organic Geochemistry*, 30(2-3): 161-188.
- Chamberlain, C.K., Clark, D.L., 1989. Characteristic Trace-Fossil Associations in Oxygen-Poor Sedimentary Environments - Comment. *Geology*, 17(6): 576-577.
- Christensen, J.P., Smethie Jr, W.M., Devol, A.H., 1987. Benthic nutrient regeneration and denitrification on the Washington continental shelf. *Deep Sea Research Part A. Oceanographic Research Papers*, 34(5-6): 1027-1047.
- Claypool, G.E., Holser, W.T., Kaplan, I.R., Sakai, H., Zak, I., 1980. The age curves of sulfur and oxygen isotopes in marine sulfate and their mutual interpretation. *Chemical Geology*, 28: 199-260.
- Croudace, I.W., Rindby, A., Rothwell, R.G., 2006. ITRAX: description and evaluation of a new multi-function X-ray core scanner. Geological Society, London, Special Publications, 267(1): 51-63.
- Curtis, C.D., 1976. Stability of minerals in surface weathering reactions: A general thermochemical approach. *Earth Surface Processes*, 1(1): 63-70.
- Curtis, C.D., Coleman, M.L., Love, L.G., 1986. Pore Water Evolution during Sediment Burial from Isotopic and Mineral Chemistry of Calcite, Dolomite and Siderite Concretions. *Geochimica Et Cosmochimica Acta*, 50(10): 2321-2334.
- Dagg, M.J., Walser, W.E., 1986. The Effect of Food Concentration on Fecal Pellet Size in Marine Copepods. *Limnology and Oceanography*, 31(5): 1066-1071.
- Davies, N.S., Gibling, M.R., 2010. Cambrian to Devonian evolution of alluvial systems: The sedimentological impact of the earliest land plants. *Earth-Science Reviews*, 98(3-4): 171-200.
- de Kamp, P.C.V., 2008. Smectite-illite-muscovite transformations, quartz dissolution, and silica release in shales. *Clays and Clay Minerals*, 56(1): 66-81.
- De Raaf, J.F.M., Boersma, J.R., Vangelder, A., 1977. Wave-Generated Structures and Sequences from a Shallow Marine Succession, Lower Carboniferous, County Cork, Ireland. *Sedimentology*, 24(4): 451-483.
- Demico, R.V., Hardie, L.A., 2002. The "carbonate factory" revisited: A reexamination of sediment production functions used to model deposition on carbonate platforms. *Journal of Sedimentary Research*, 72(6): 849-857.
- Detmers, J., Bruchert, V., Habicht, K.S., Kuever, J., 2001. Diversity of Sulfur Isotope Fractionations by Sulfate-Reducing Prokaryotes. *Appl. Environ. Microbiol.*, 67(2): 888-894.
- Dietrich, J. et al., 2011. Geological setting and resource potential of conventional petroleum plays in Paleozoic basins in eastern Canada. *Bulletin of Canadian Petroleum Geology* 59(1): 54-84.
- Drever, J.I., Stillings, L.L., 1997. The role of organic acids in mineral weathering. *Colloids and Surfaces A: Physicochemical and Engineering Aspects*, 120(1-3): 167-181.
- Eberl, D., Hower, J., 1976. Kinetics of Illite Formation. *Geological Society of America Bulletin*, 87(9): 1326-1330.
- Ekdale, A.A., Mason, T.R., 1988. Characteristic Trace-Fossil Associations in Oxygen-Poor Sedimentary Environments. *Geology*, 16(8): 720-723.

- Elliott, W.C., Matisoff, G., 1996. Evaluation of kinetic models for the smectite to illite transformation. *Clays and Clay Minerals*, 44(1): 77-87.
- Essene, E.J., Peacor, D.R., 1995. Clay mineral thermometry - A critical perspective. *Clays and Clay Minerals*, 43(5): 540-553.
- Falkowski, P. et al., 2000. The global carbon cycle: A test of our knowledge of earth as a system. *Science*, 290(5490): 291-296.
- Freed, R.L., Peacor, D.R., 1989. Variability in Temperature of the Smectite Illite Reaction in Gulf-Coast Sediments. *Clay Minerals*, 24(2): 171-180.
- Froelich, P.N. et al., 1979. Early oxidation of organic matter in pelagic sediments of the eastern equatorial Atlantic: suboxic diagenesis. *Geochimica et Cosmochimica Acta*, 43(7): 1075-1090.
- George, T.N., 1958. Lower Carboniferous palaeogeography of the British Isles. *Proc. Yorks. Geol. Soc.*, 31: 227-318.
- Ghadeer, S.G., Macquaker, J.H.S., 2011. Sediment transport processes in an ancient mud-dominated succession: a comparison of processes operating in marine offshore settings and anoxic basinal environments. *Journal of the Geological Society*, 168(5): 1121-1132.
- Gillespie, H., 1998. Acritarch biostratigraphy and taxonomy of the Winterhouse Formation (Upper Ordovician), Port Au Port Peninsula, Newfoundland. Masters of Science Thesis, Memorial University of Newfoundland, St. John's, Newfoundland.
- Gingras, M.K., MacEachern, J.A., Dashtgard, S.E., 2011. Process ichnology and the elucidation of physico-chemical stress. *Sedimentary Geology*, 237(3-4): 115-134.
- Gingras, M.K., Rasanen, M.E., Pemberton, S.G., Romero, L.P., 2002. Ichnology and sedimentology reveal depositional characteristics of bay-margin parasequences in the Miocene Amazonian foreland basin. *Journal of Sedimentary Research*, 72(6): 871-883.
- Goldich, S.S., 1938. A Study in Rock Weathering. *Journal of Geology*, 46: 17-58.
- Goldring, R., Pollard, J.E., Taylor, A.M., 1991. *Anconichnus horizontalis*; a pervasive ichnofabric-forming trace fossil in post-paleozoic offshore siliciclastic facies. 13th International Sedimentological Congress, Ichnologic Symposium. *Palaios*, 6: 250-263.
- Graham, J.R., 1996. Dinantian river systems and coastal zone sedimentation in northwest Ireland. *Recent Advances in Lower Carboniferous Geology*(107): 183-206.
- Hannigan, R.E., Basu, A.R., 1998. Late diagenetic trace element remobilization in organic-rich black shales of the taconic foreland basin of Quebec, Ontario and New York. In: *Schweizerbart, "Shales and Mudstones"*, 2: 209-234.
- Harrison, A.G., Thode, H.G., 1957. The kinetic isotope effect in the chemical reduction of sulphate. *Transactions of the Faraday Society*, 53: 1648-1651.
- Harrison, A.G.T., H.G., 1958. Mechanism of the bacterial reduction of sulphate from isotope fractionation studies. *Trans. Faraday Soc.*, 54: 84 - 92.
- Helgeson, H.C., Murphy, W.M., Aagaard, P., 1984. Thermodynamic and kinetic constraints on reaction rates among minerals and aqueous solutions. II. Rate constants, effective surface area, and the hydrolysis of feldspar. *Geochimica et Cosmochimica Acta*, 48(12): 2405-2432.

- Hower, J., Eslinger, E.V., Hower, M.E., Perry, E.A., 1976. Mechanism of Burial Metamorphism of Argillaceous Sediment .1. Mineralogical and Chemical Evidence. *Geological Society of America Bulletin*, 87(5): 725-737.
- Isaacs, C.M., 1985. Abundance Versus Rates of Accumulation in Fine-Grained Strata of the Miocene Santa-Barbara Basin, California. *Geo-Marine Letters*, 5(1): 25-30.
- Jaeger, J.M., Nittrouer, C.A., 2006. A quantitative examination of modern sedimentary lithofacies formation on the glacially influenced Gulf of Alaska continental shelf. *Continental Shelf Research*, 26(17-18): 2178-2204.
- Johnston, D.L., Henderson, C.M., Schmidt, M.J., 2010. Upper Devonian to Lower Mississippian conodont biostratigraphy of uppermost Wabamun Group and Palliser Formation to lowermost Banff and Lodgepole formations, southern Alberta and southeastern British Columbia, Canada: Implications for correlations and sequence stratigraphy. *Bulletin of Canadian Petroleum Geology*, 58(4): 295-341.
- Jorgensen, B.B., 1982. Mineralization of organic matter in the sea bed[mdash]the role of sulphate reduction. *Nature*, 296(5858): 643-645.
- Kaplan, I.R., 1975. Stable Isotopes as a Guide to Biogeochemical Processes. *Proceedings of the Royal Society of London Series B-Biological Sciences*, 189(1095): 183-211.
- Kemp, A.L.W., Thode, H.G., 1968. The mechanism of the bacterial reduction of sulphate and of sulphite from isotope fractionation studies. *Geochimica et Cosmochimica Acta*, 32(1): 71-91.
- Kendrick, M.A., Burgess, R., Leach, D., Patrick, R.A.D., 2002. Hydrothermal fluid origins in Mississippi valley-type ore districts: Combined noble gas (He, Ar, Kr) and halogen (Cl, Br, I) analysis of fluid inclusions from the Illinois-Kentucky fluorspar district, Viburnum Trend, and Tri-State districts, midcontinent United States. *Economic Geology and the Bulletin of the Society of Economic Geologists*, 97(3): 453-469.
- Kennedy, M.J., Pevcar, D.R., Hill, R.J., 2002. Mineral Surface Control of Organic Carbon in Black Shale. *Science*, 295(5555): 657-660.
- Knight, I., and Cawood, P.A., 1992. Paleozoic geology of western Newfoundland: an exploration of a deformed Cambro-Ordovician passive margin and foreland basin, and Carboniferous successor basin. Centre for Earth Resources Research, Memorial University of Newfoundland, 2: 403.
- Kuhlemann, J., Vennemann, T., Herlec, U., Zech, S., Bechstadt, T., 2001. Variations of sulfur isotopes, trace element compositions, and cathodoluminescence of Mississippi Valley-type Pb-Zn ores from the Drau Range, Eastern Alps (Slovenia-Austria): Implications for ore deposition on a regional versus microscale. *Economic Geology and the Bulletin of the Society of Economic Geologists*, 96(8): 1931-1941.
- Leach, D. et al., 2006. Precipitation of lead-zinc ores in the Mississippi Valley-type deposit at Treves, Cevennes region of southern France. *Geofluids*, 6(1): 24-44.
- Leach, D.L. et al., 2010. Sediment-Hosted Lead-Zinc Deposits in Earth History. *Economic Geology*, 105(3): 593-625.

- Leach, D.L. et al., 2001. Mississippi Valley-type lead-zinc deposits through geological time: implications from recent age-dating research. *Mineralium Deposita*, 36(8): 711-740.
- Levin, L.A., Rathburn, A.E., Gutierrez, D., Munoz, P., Shankle, A., 2003. Bioturbation by symbiont-bearing annelids in near-anoxic sediments: Implications for biofacies models and paleo-oxygen assessments. *Palaeogeography Palaeoclimatology Palaeoecology*, 199(1-2): 129-140.
- Lovley, D.R., Phillips, E.J.P., 1986. Availability of Ferric Iron for Microbial Reduction in Bottom Sediments of the Freshwater Tidal Potomac River. *Appl. Environ. Microbiol.*, 52(4): 751-757.
- Lovley, D.R., Phillips, E.J.P., 1988. Novel Mode of Microbial Energy Metabolism: Organic Carbon Oxidation Coupled to Dissimilatory Reduction of Iron or Manganese. *Appl. Environ. Microbiol.*, 54(6): 1472-1480.
- Machel, H.G., 2001. Bacterial and thermochemical sulfate reduction in diagenetic settings -- old and new insights. *Sedimentary Geology*, 140(1-2): 143-175.
- Machel, H.G., Krouse, H.R., Sassen, R., 1995. Products and distinguishing criteria of bacterial and thermochemical sulfate reduction. *Applied Geochemistry*, 10(4): 373-389.
- Machent, P.G., Taylor, K.G., Macquaker, J.H.S., Marshall, J.D., 2007. Patterns of early post-depositional and burial cementation in distal, shallow-marine sandstones: Upper Cretaceous Kenilworth Member, Book Cliffs, Utah, USA. *Sedimentary Geology*, 198(1-2): 125-145.
- Macquaker, J.H.S., Adams, A.E., 2003. Maximizing information from fine-grained sedimentary rocks: An inclusive nomenclature for mudstones. *Journal of Sedimentary Research*, 73(5): 735-744.
- Macquaker, J.H.S., Bentley, S.J., Bohacs, K.M., 2010a. Wave-enhanced sediment-gravity flows and mud dispersal across continental shelves: Reappraising sediment transport processes operating in ancient mudstone successions. *Geology*, 38(10): 947-950.
- Macquaker, J.H.S., Bohacs, K.M., 2007. *Geology - On the accumulation of mud*. *Science*, 318(5857): 1734-1735.
- Macquaker, J.H.S., Curtis, C.D., Coleman, M.L., 1997. The role of iron in mudstone diagenesis: Comparison of Kimmeridge clay formation mudstones from onshore and offshore (UKCS) localities. *Journal of Sedimentary Research*, 67(5): 871-878.
- Macquaker, J.H.S., Gawthorpe, R.L., 1993. Mudstone Lithofacies in the Kimmeridge Clay Formation, Wessex Basin, Southern England - Implications for the Origin and Controls of the Distribution of Mudstones. *Journal of Sedimentary Petrology*, 63(6): 1129-1143.
- Macquaker, J.H.S., Keller, M.A., Davies, S.J., 2010b. Algal Blooms and "Marine Snow": Mechanisms That Enhance Preservation of Organic Carbon in Ancient Fine-Grained Sediments. *Journal of Sedimentary Research*, 80(11-12): 934-942.
- Macquaker, J.H.S., Taylor, K.G., Gawthorpe, R.L., 2007. High-resolution facies analyses of mudstones: Implications for paleoenvironmental and sequence stratigraphic interpretations of offshore ancient mud-dominated successions. *Journal of Sedimentary Research*, 77(3-4): 324-339.

- Macqueen, R.W., Sandberg, C.A., 1970. Stratigraphy, age, and interregional correlation of the Exshaw Formation, Alberta Rocky Mountains. *Bulletin of Canadian Petroleum Geology*, 18: 32-57.
- Mango, F., Jarvie, D., 2009. Low-temperature gas from marine shales. *Geochemical Transactions*, 10(1): 3.
- Mellroy, D., 2004. Some ichnological concepts, methodologies applications and frontiers. Geological Society, London, Special Publications, 228: 3-27.
- Mckay, J.L., Longstaffe, F.J., Plint, A.G., 1995. Early Diagenesis and Its Relationship to Depositional Environment and Relative Sea-Level Fluctuations (Upper Cretaceous Marshybank Formation, Alberta and British-Columbia). *Sedimentology*, 42(1): 161-190.
- Meysman, F.J.R., Middelburg, J.J., Heip, C.H.R., 2006. Bioturbation: a fresh look at Darwin's last idea. *Trends in Ecology & Evolution*, 21(12): 688-695.
- Milliken, K., Choh, S.J., Papazis, P., Schieber, J., 2007. "Cherty" stringers in the Barnett Shale are agglutinated foraminifera. *Sedimentary Geology*, 198(3-4): 221-232.
- Mitchell, C.E., Goldman, D., Delano, J.W., Samson, S.D., Bergstrom, S.M., 1994. Temporal and spatial distribution of biozones and facies relative to geochemically correlated K-bentonites in the Middle Ordovician Taconic foredeep. *Geology*, 22(8): 715-718.
- Mitchell, W.I., 2004. Carboniferous. Regional Guide to the Geology of Northern Ireland — our Natural Foundation. Geological Survey of Northern Ireland (GSNI), Belfast: 79-116.
- Morse, J.W., Arvidson, R.S., Luttge, A., 2007. Calcium carbonate formation and dissolution. *Chemical Reviews*, 107(2): 342-381.
- Morse, J.W., Millero, F.J., Cornwell, J.C., Rickard, D., 1987. The chemistry of the hydrogen sulfide and iron sulfide systems in natural waters. *Earth-Science Reviews*, 24(1): 1-42.
- Murowchick, J.B., Barnes, H.L., 1986. Marcasite Precipitation from Hydrothermal Solutions. *Geochimica Et Cosmochimica Acta*, 50(12): 2615-2629.
- Myers, C.R., Nealson, K.H., 1988. Microbial reduction of manganese oxides: Interactions with iron and sulfur. *Geochimica et Cosmochimica Acta*, 52(11): 2727-2732.
- Nadeau, P.H., Wilson, M.J., Mchardy, W.J., Tait, J.M., 1984. Interstratified Clays as Fundamental Particles. *Science*, 225(4665): 923-925.
- Nesbitt, H.W., Fedo, C.M., Young, G.M., 1997. Quartz and Feldspar Stability, Steady and Non-steady-State Weathering, and Petrogenesis of Siliciclastic Sands and Muds. *The Journal of Geology*, 105(2): 173-191.
- Newton, R., Bottrell, S., 2007. Stable isotopes of carbon and sulphur as indicators of environmental change: past and present. *Journal of the Geological Society*, 164(4): 691-708.
- Peevler, J., Fayek, M., Misra, K.C., Riciputi, L.R., 2003. Sulfur isotope microanalysis of sphalerite by SIMS: constraints on the genesis of Mississippi valley-type mineralization, from the Mascot-Jefferson City district, East Tennessee. *Journal of Geochemical Exploration*, 80(2-3): 277-296.

- Pemberton, G.S., MacEachern, J.A., Frey, R.W., 2002. Trace fossils and facies models: environmental and allostratigraphic significance. In: *Facies Models: Response to sea level change*, 6: 47-73.
- Pemberton, S.G., MacEachern, J.A., Gingras, M.K., Saunders, T.D.A., 2008. Biogenic chaos: Cryptobioturbation and the work of sedimentologically friendly organisms. *Palaeogeography Palaeoclimatology Palaeoecology*, 270(3-4): 273-279.
- Piper, D.Z., Calvert, S.E., 2009. A marine biogeochemical perspective on black shale deposition. *Earth-Science Reviews*, 95(1-2): 63-96.
- Price, F.T., Shieh, Y.N., 1979. Fractionation of sulfur isotopes during laboratory synthesis of pyrite at low temperatures. *Chemical Geology*, 27(3): 245-253.
- Price, R.A., 1970. *Geology - Canmore (east half) Alberta*. Geological Survey of Canada, Map 1265 A.
- Putnis, A., 2002. Mineral replacement reactions: from macroscopic observations to microscopic mechanisms. *Mineralogical Magazine*, 66(5): 689-708.
- Putnis, A., 2009. Mineral Replacement Reactions. *Thermodynamics and Kinetics of Water-Rock Interaction*, 70: 87-124.
- Quinn, L., Williams, S.H., Harper, D.A.T., Clarkson, E.N.K., 1999. Late Ordovician foreland basin fill: Long Point Group of onshore western Newfoundland. *Bulletin of Canadian Petroleum Geology*, 47(1): 63-80.
- Raasch, G.O., 1956. Late Devonian and/or Mississippian faunal succession in Stettler area, Alberta. *J. Alta. Soc. Pet. Geol.*, 4: 112-118.
- Raiswell, R., 1988. Evidence for Surface Reaction-Controlled Growth of Carbonate Concretions in Shales. *Sedimentology*, 35(4): 571-575.
- Raiswell, R., Fisher, Q.J., 2000. Mudrock-hosted carbonate concretions: a review of growth mechanisms and their influence on chemical and isotopic composition. *Journal of the Geological Society*, 157: 239-251.
- Rickard, D., Luther, G.W., 2007. Chemistry of Iron Sulfides. *Chemical Reviews*, 107(2): 514-562.
- Rijken, P., Cooke, M.L., 2001. Role of shale thickness on vertical connectivity of fractures: application of crack-bridging theory to the Austin Chalk, Texas. *Tectonophysics*, 337(1-2): 117-133.
- Rimstidt, J.D., Vaughan, D.J., 2003. Pyrite oxidation: a state-of-the-art assessment of the reaction mechanism. *Geochimica et Cosmochimica Acta*, 67(5): 873-880.
- Roh, Y. et al., 2003. BIOGEOCHEMICAL AND ENVIRONMENTAL FACTORS IN Fe BIOMINERALIZATION: MAGNETITE AND SIDERITE FORMATION. *Clays and Clay Minerals*, 51(1): 83-95.
- Ross, D.J.K., Bustin, M., R., 2009. The importance of shale composition and pore structure upon gas storage potential of shale gas reservoirs. *Marine and Petroleum Geology*, 26(6): 916-927.
- Sageman, B.B. et al., 2003. A tale of shales: the relative roles of production, decomposition, and dilution in the accumulation of organic-rich strata, Middle-Upper Devonian, Appalachian basin. *Chemical Geology*, 195(1-4): 229-273.
- Savoy, L.E., Harris, A.G., Mountjoy, E.W., 1999. Extension of lithofacies and conodont biofacies models of Late Devonian to Early Carboniferous carbonate ramp and

- black shale systems, southern Canadian Rocky Mountains. *Canadian Journal of Earth Sciences*, 36(8): 1281-1298.
- Schieber, J., 1996. Early diagenetic silica deposition in algal cysts and spores: A source of sand in black shales? *Journal of Sedimentary Research*, 66(1): 175-183.
- Schieber, J., 2007. Oxidation of detrital pyrite as a cause for Marcasite Formation in marine lag deposits from the Devonian of the eastern US. *Deep-Sea Research Part II-Topical Studies in Oceanography*, 54(11-13): 1312-1326.
- Schieber, J., 2009. Discovery of agglutinated benthic foraminifera in Devonian black shales and their relevance for the redox state of ancient seas. *Palaeogeography Palaeoclimatology Palaeoecology*, 271(3-4): 292-300.
- Schieber, J., 2011. Marcasite in Black Shales-a Mineral Proxy for Oxygenated Bottom Waters and Intermittent Oxidation of Carbonaceous Muds. *Journal of Sedimentary Research*, 81(7-8): 447-458.
- Schieber, J., Southard, J., Thaisen, K., 2007. Accretion of Mudstone Beds from Migrating Floccule Ripples. *Science*, 318(5857): 1760-1763.
- Schieber, J., Southard, J.B., Schimmelmann, A., 2010. Lenticular Shale Fabrics Resulting from Intermittent Erosion of Water-Rich Muds-Interpreting the Rock Record in the Light of Recent Flume Experiments. *Journal of Sedimentary Research*, 80(1-2): 119-128.
- Schmoker, J.W., 1981. Determination of Organic-Matter Content of Appalachian Devonian Shales from Gamma-Ray Logs. *Aapg Bulletin-American Association of Petroleum Geologists*, 65(7): 1285-1298.
- Schoonen, M.A.A., Barnes, H.L., 1991. Reactions Forming Pyrite and Marcasite from Solution .I. Nucleation of Fes₂ Below 100-Degrees-C. *Geochimica Et Cosmochimica Acta*, 55(6): 1495-1504.
- Scott, D.B., Medioli, F., Braund, R., 2003. Foraminifera from the Cambrian of Nova Scotia: The oldest multichambered foraminifera. *Micropalaeontology*, 49(2): 109-126.
- Sevastopulo, G.D., Wyse Jackson, P.N., 2009. Carboniferous: Mississippian (Tournaisian and Viséan). In: Holland, C.H., Sanders, I. (Eds.), *The Geology of Ireland*. Dunedin Academic Press, Edinburgh: 215-268.
- Shull, D.H., Benoit, J.M., Wojcik, C., Senning, J.R., 2009. Infaunal burrow ventilation and pore-water transport in muddy sediments. *Estuarine, Coastal and Shelf Science*, 83(3): 277-286.
- Siegel, D.I., Pfannkuch, H.O., 1984. Silicate Mineral Dissolution at Ph-4 and near Standard Temperature and Pressure. *Geochimica Et Cosmochimica Acta*, 48(1): 197-201.
- Sims, P.A., Mann, D.G., Medlin, L.K., 2006. Evolution of the diatoms: insights from fossil, biological and molecular data. *Phycologia*, 45(4): 361-402.
- Smith, M.G., Bustin, R.M., 2000. Late Devonian and Early Mississippian Bakken and Exshaw black shale source rocks, Western Canada sedimentary basin: A sequence stratigraphic interpretation. *Aapg Bulletin-American Association of Petroleum Geologists*, 84(7): 940-960.

- Somerville, I.D. et al., 2009. Carbonate facies and biostromal distribution in a tectonically controlled platform in northwest Ireland during the late Viséan (Mississippian). *Proceedings of the Yorkshire Geological Society*, 57: 165-192.
- Stillings, L.L., Drever, J.I., Brantley, S.L., Sun, Y., Oxburgh, R., 1996. Rates of feldspar dissolution at pH 3-7 with 0-8 m M oxalic acid. *Chemical Geology*, 132(1-4): 79-89.
- Stoffell, B., Appold, M.S., Wilkinson, J.J., McClean, N.A., Jeffries, T.E., 2008. Geochemistry and Evolution of Mississippi Valley-Type Mineralizing Brines from the Tri-State and Northern Arkansas Districts Determined by LA-ICP-MS Microanalysis of Fluid Inclusions. *Economic Geology*, 103(7): 1411-1435.
- Subramanian, V., Ittekkot, V., Unger, D., Madhavan, N., 2006. Silicate weathering in South Asian Tropical River Basins. *The Silicon Cycle: Human Perturbations and Impacts on Aquatic Systems*, SCOPE Series, 66.(Island Press, Washington, D.C., USA.): 3-13.
- Sverjensky, D.A., 1986. Genesis of Mississippi Valley Type Lead-Zinc Deposits. *Annual Review of Earth and Planetary Sciences*, 14: 177-199.
- Taylor, K.G., Macquaker, J.H.S., 2000. Early diagenetic pyrite morphology in a mudstone-dominated succession: the Lower Jurassic Cleveland Ironstone Formation, eastern England. *Sedimentary Geology*, 131(1-2): 77-86.
- Trabucho-Alexandre, J. et al., 2010. The mid-Cretaceous North Atlantic nutrient trap: Black shales and OAEs. *Paleoceanography*, 25.
- Tréguer, P. et al., 1995. The Silica Balance in the World Ocean: A Reestimate. *Science*, 268(5209): 375-379.
- Turner, J.T., 2002. Zooplankton fecal pellets, marine snow and sinking phytoplankton blooms. *Aquatic Microbial Ecology*, 27(1): 57-102.
- Urban-Rich, J., 2001. Seston effects on faecal pellet carbon concentrations from a mixed community of copepods in Balsfjord, Norway, and the Antarctic Polar Front. *ICES Journal of Marine Science*, 58(3): 700-710.
- Van Cappellen, P., 2003. Biomineralization and Global Biogeochemical Cycles. *Reviews in Mineralogy and Geochemistry*, 54(1): 357-381.
- Vandeginste, V. et al., 2007. Geochemical constraints on the origin of the Kicking Horse and Monarch Mississippi Valley-type lead-zinc ore deposits, southeast British Columbia, Canada. *Mineralium Deposita*, 42(8): 913-935.
- Velde, B., Vasseur, G., 1992. Estimation of the Diagenetic Smectite to Illite Transformation in Time-Temperature Space. *American Mineralogist*, 77(9-10): 967-976.
- Vermcij, G.J., 1989. The origin of skeletons. *PALAIOS*, 4(6): 585-589.
- Vorhies, J.S., Gaines, R.R., 2009. Microbial dissolution of clay minerals as a source of iron and silica in marine sediments. *Nature Geosci.*
- Warren, J., 2000. Dolomite: occurrence, evolution and economically important associations. *Earth-Science Reviews*, 52(1-3): 1-81.
- Weaver, C.E., 1967. Potassium, illite and the ocean. *Geochimica et Cosmochimica Acta*, 31(11): 2181-2196.

- Welch, S.A., Ullman, W.J., 1996. Feldspar dissolution in acidic and organic solutions: Compositional and pH dependence of dissolution rate. *Geochimica et Cosmochimica Acta*, 60(16): 2939-2948.
- Whitaker, F.F., Smart, P.L., 1990. Active Circulation of Saline Ground Waters in Carbonate Platforms - Evidence from the Great-Bahama-Bank. *Geology*, 18(3): 200-203.
- Whiticar, M.J., 1999. Carbon and hydrogen isotope systematics of bacterial formation and oxidation of methane. *Chemical Geology*, 161(1-3): 291-314.
- Wilkin, R.T., Barnes, H.L., Brantley, S.L., 1996. The size distribution of framboidal pyrite in modern sediments: An indicator of redox conditions. *Geochimica et Cosmochimica Acta*, 60(20): 3897-3912.
- Williams S.H., a.C., P.A., 1989. Geological setting and resource potential of conventional petroleum plays in Paleozoic basins in eastern Canada. Geological Survey of Canada, Map 1678A.
- Williams S.H., B., W.D., and James, N.P., 1987. Graptolites from the Lower-Middle Ordovician St. George and Table Head groups, western Newfoundland, and their correlation with trilobite, graptolite, brachiopod and conodont zones. *Canadian Journal of Earth Sciences*, 24: 456-470.
- Williams, S.H., Boyce, W.D., Knight, I., Measures, E.A., Rohr, D.M., 2000. Early ordovician (Arenig) graptolites from the upper St. George Group, Port Au Port, Peninsula: preservation correlation, and paleo-environmental and stratigraphic implications Current Research: Newfoundland Department of Mines and Energy, Report 2000-1: 291-298.
- Wogelius, R.A., Walther, J.V., 1991. Olivine dissolution at 25°C: Effects of pH, CO₂, and organic acids. *Geochimica et Cosmochimica Acta*, 55(4): 943-954.
- Yoon, W.D., Marty, J.C., Sylvain, D., Nival, P., 1996. Degradation of faecal pellets in *Pegae confederata* (Salpidae, Thaliacea) and its implication in the vertical flux of organic matter. *Journal of Experimental Marine Biology and Ecology*, 203(2): 147-177.

